INTERFACE PROPERTIES OF MODIFIED INDIUM TIN OXIDE BASED ORGANIC LIGHT EMITTING DIODES WITH FUNCTIONAL AROMATIC MOLECULES

A Thesis submitted to
the Graduate School of Engineering and Sciences of
İzmir Institute of Technology
in Partial Fulfillment of the Requirements for the Degree of

MASTER OF SCIENCE

in Physics

by

Hasan AYDIN

July 2011
İZMİR

We approve the thesis of **Hasan AYDIN**

_____

Assoc. Prof. Salih OKUR
Supervisor

_____

Assist. Prof. Yusuf SELAMET
Committee Member

_____

Assist. Prof. Hadi ZAREİE
Committee Member

4 July 2011

_____

Prof. Dr. Nejat BULUT
Head of the Department of Physics

_____

Prof. Dr. Durmuş Ali DEMİR
Dean of the Graduate School of Engineering and Sciences

ACKNOWLEDGEMENTS

Firstly, I would like to thank my supervisor, Dr. Salih Okur. His encouragement and support made this thesis possible. I also would like to thank Dr. Şerafettin Demiç, Dr. Hadi Zareie and Mustafa Can for their contribution to this thesis. Moreover, I want to thank our lab mates, Nesli Yağmurcukardeş, Ali Kemal Havare, Mavişe Şeker and Fevzi Sümer for providing a wonderful working environment. Of course, Ali Kemal and Nesli deserve my special thanks for their friendship, supporting and discussing with my experimental work.

Finally, I can't find better words to explain contribution of my family to my education and explain their love. I express my thanks for their helps.

ABSTRACT

INTERFACE PROPERTIES MODIFIED INDIUM TIN OXIDE BASED ORGANIC LIGHT EMITTING DIODES WITH FUNCTIONAL AROMATIC MOLECULES

This thesis focused on modification and characterization of ITO substrates with carboxylic acid based self-assembled monolayers to improve OLED device performance. In this study, ITO was used as anode material in OLEDs. In order to modify ITO electrodes, MePIFA and DPIFA aromatic small molecules with double bound carboxylic acid have been used as self-assembly monolayer (SAM). Characterizations of modified ITO and unmodified ITO surfaces were performed via atomic force microscopy and scanning tunneling microscopy. In addition to surface characterization, I-V measurements of the modified and unmodified ITO were taken via spreading resistance microscopy and scanning tunneling microscopy. Moreover, in order to measure change in the surface potential after the modification of ITO surface with MePIFA and DPIFA SAM molecules, Kelvin Probe Force Microscopy was performed. Finally two different configurations of OLEDs devices were fabricated using thermal evaporator system in order to explore the effect of SAM modified ITO on electrical characterization of OLED devices. It was shown that OLED intensity, and turn on voltage were improved compared to OLED devices with unmodified ITO.

ÖZET

FONKSİYONEL AROMATİK MOLEKÜLLER İLE MODİFİYE OLMUŞ İNDİYUM KALAY OKSİT TABANLI IŞIK YAYAN ORGANİK DİYOTLARIN ARAYÜZEY ÖZELLİKLERİ

Bu tez, OLED cihaz performansını artırmak için karboksilik asit bazlı kendiliğinden organize tek katman tabakaları ile ITO yüzeyinin modifikasyonu ve karekterizasyonu üzerine odaklanmıştır. Bu çalışmada, ITO, OLED'ler de anot malzemesi olarak kullanılmıştır. ITO elektrodunu modifiye etmek için, çift karboksilik asit bağlı MePIFA and DPIFA aromatik küçük moleküller kendiliğinden organize tek katman olarak kullanılmıştır. MePIFA and DPIFA SAM molekülleriyle modifiye edilmiş ITO ların ve modifiye edilmemiş ITO nun yüzey karekterizasyonu atomik kuvvet mikroskobu ve taramalı tünellemeli mikroskobu ile gerçekleşmiştir. Yüzey karekterizasyonuna ek olarak, MePIFA and DPIFA ile modifiye edilmiş ITO ların ve modifiye edilmemiş ITO nun I-V ölçümleri taramalı tünellemeli ve direnç dağılım mikroskobu ile alınmıştır. Ayrıca, MePIFA ve DPIFA SAM molekülleri ile ITO nun yüzey modifikasyonun gerçekleştiğini anlamak için, Kelvin Probe kuvvet mikroskobu uygulanmıştır. Tezin son aşamasında, iki farklı OLED cihaz konfigürasyonu ısıl buharlaştırma sisteminde ITO yüzeyindeki SAM modifikasyonun cihazların elektriksel karekterizasyonu üzerindeki etkisini araştırmak için yapılmıştır. OLED ışık şiddeti ve açma gerilimi modifiye edilmemiş ITO lu OLED cihazlara göre iyileşme olduğu gösterilmiştir.

To my Family

TABLE OF CONTENTS

LIST OF FIGURES

Figure **Page**

LIST OF TABLES

CHAPTER 1

INTRODUCTION

Today's modern electronic devices are not only made of crystalline inorganic semiconductor but also organic semiconductor which shows attractive chemical, mechanical and electrical properties. Technological applications of semiconducting materials as LED device have indisputable significance. After invention of Organic LED (OLED) using thin films made of electroluminescent organic semiconducting compounds, there is an increasing interest in these devices over last decade due to their potential applications in organic electronics. Currently, OLEDs technologies are commercialized and have many applications started to take place in display markets. OLEDs have several advantages with respect to liquid crystal display (LCD) and cathode ray tube (CRT). OLEDs are self luminous, backlight is not required to display image less power consumption. OLEDs are also very thin and have high brightness (150.000 cd/m^2). Thus each of single pave the way for wide viewing angle which makes OLEDs stand out compared to LCD. Moreover, they can be fabricated on the plastic substrates which give rise to flexible electronics. They are low costs and easy to fabricate roll to roll manufacturing process with inkjet printing and screen printing techniques can be used.

The disadvantages of OLEDs are mostly associated with their lifetime. Organic materials are sensitive to humidity and oxygen which degrade device performance severely. Thus appropriate encapsulation is required to prevent from device degradation.

Electroluminance (EL) from organic compounds was first observed in 1963 by Pope et al. (Pope et al., 1963). It was needed to apply a voltage up to 400 V to an anthracene crystal with large thicknesses (10μm~5mm) to observe luminance. In 1982 (Vincett et al., 1982) carried out blue EL from anthracene crystal with thicknesses about 0.6 μm at a driven voltage less than 100V. However this voltage was still not compatible with organic electronic applications. Spectacular development came true in 1987; Ching W. Thank and Steve Van Slyke presented a novel organic device at Eastmen Kodak Company. This is considered the first organic light emitting diode (Tang and VanSlyke, 1987). The device was fabricated by thermally evaporated organic

small molecules including, N,N'-diphenyl-N, N'-bis(3-methylphenyl) 1-1'biphenyl-4,4' diamine (TPD) and tris(8-hydroxyquinoline) aluminum (Alq_3) with a total thickness of ~ 100nm in a double layer structure. They succeed in very high brightness of more than 1000cd/m^2 and external quantum efficiency of 1% at a driven voltage of about 10V (Tang and VanSlyke, 1987). In 1989 developed a laser dye Alq_3 multilayer structure, in which the fluorescent efficiency was improved. Following important study has to be another type of OLED in 1990. Richard Friend's group at Cambridge University revealed the first polymer LED (PLED) by using luminescent poly-(para-phenlenevinylene) (PPV) material which was fabricated by spin coating. The light emission is in the green-yellow part in the spectrum, and efficiency was about 0.05 % (Burroughes et al., 1990).

Recently research in the literature has been focused to improve efficiency of OLEDs and to increase stability of used organic compounds. The weak bonding at organic/inorganic interface in OLEDs due to the incompatible structural difference is one of the limiting parameters for the stability and performance of OLEDs devices. To find a solution to these problems, Conjugated polymer (Nuesch et al., 1998; Pei and Oh, 2003), organic acid (Nüesch et al., 2000) thin platinum layer (Shen et al., 2001) and siloxane coated (Malinsky et al., 1999) were used to modify anode surface (Indium tin oxide) (ITO). However significant improvement has been obtained, when Self Assembled Monolayer (SAM) were used. SAM was used to establish a compatible interface between hydrophilic ITO surface and hydrophobic hole transport layer (HTL) (Cui et al., 2002a; Cui et al., 2002b). Recently works, important improvements have been accomplished to enhance of the stability and efficiency of OLEDs by using SAM technique with chemical covalent bonding to Si group compare to alkyl chains to TPD molecules and ITO surface (ITO/TPD-Si_2) (Lee et al., 2002). An exponential decrease in the tunneling current was observed due to the increase of tunneling barrier distance because of increase of alkyl chain length (Huang et al., 2005; Selzer et al., 2002). In another work, smaller threshold voltage was obtained in OLED I-V measurements, since the charge transport increased with inelastic tunneling mechanism and due to the smaller HOMO-LUMO energy level difference of aromatic molecules with respect to the alkyl structures (Vuillaume et al., 2006).

In our study, two types of carboxylic acid based SAMs were synthesized to modify ITO surface using self-assembled monolayer technique. The aim is to

characterize modified and unmodified ITO substrates via Scanning Probe Microscope and investigate effect of carboxylic acid based SAMs on OLED charge transport.

CHAPTER 2

BACKGROUND OF ORGANIC SEMICONDUCTOR AND ORGANIC LIGHT EMIITING DIODES (OLEDs)

2.1. Organic Semiconductor

The development of new class of materials, commonly known as organic semiconductors has led to new revolution at 21st century. Organic semiconductors are composed of mainly carbon atoms with energy band gap between 1.5 and 3 eV giving rise to light emission or absorption in the visible spectral range (Brütting). Moreover, although organic semiconductors were seen as insulator with low charge carrier mobility, in recent years, mobility in organic semiconductors exceeding 1cm^2/Vs have been reported, which is comparable to mobility measured in amorphous silicon (Haldi, 2008).

There are two types of semiconductor materials exist namely organic molecules and polymers (Brütting). Organic molecules have less carbon atoms. Polymer composes of a large molecule with repeated units which are connected by the covalent bonds. The difference between two classes of materials is formation of thin film technique. Fabrication of OLEDs is generally developed by deposition of small molecules in gas phase via sublimation or evaporation. The thin film of polymers can be formed in solution phase by spin coating or printing technique (Brütting). However both have a similar electronic structure formed by hybridized carbon atoms in the molecules. In the electronic configuration of carbon consist four valance orbitals (2s, $2p_x$, $2p_y$, and $2p_z$) (see Figure 2.1 a) (Haldi, 2008) responsible for the formation of covalent bonds. Combinations of s and p atomic orbitals form hybrid orbitals with three possible hybridization: sp, sp^2 and sp^3 (see Figure 2.1 b). The subscript denotes the number of p-orbitals that are part of the superposition.

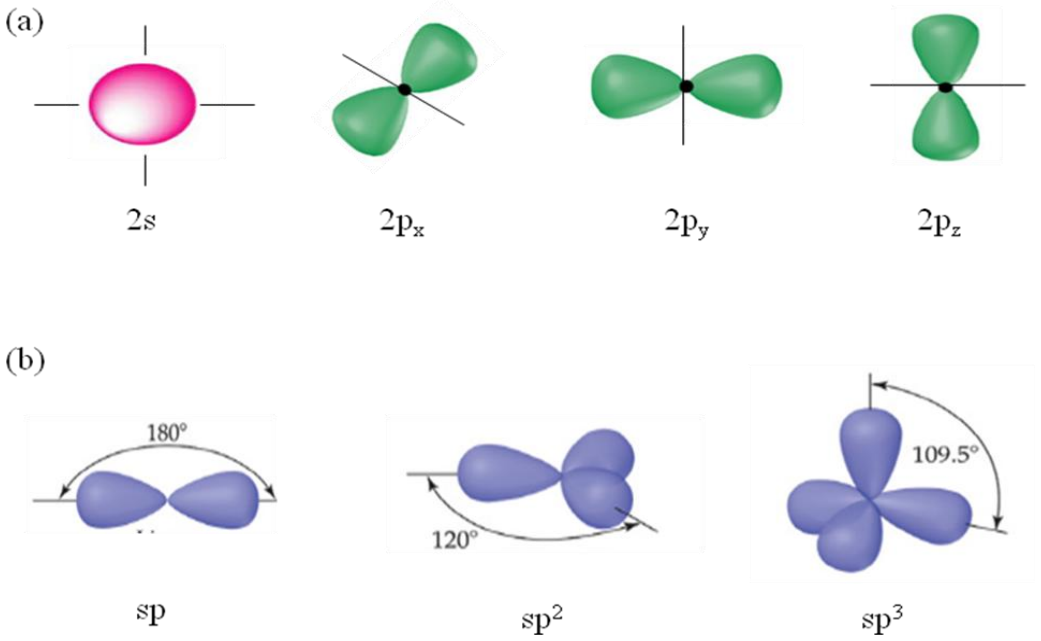

Figure 2.1. Illustration of the 2s, 2p$_x$, 2p$_y$, 2p$_z$ (a), and hybrid orbitals (b) for a carbon atom.

When two atoms are bonded by overlapping over hybrid orbitals, sigma (σ) and pi (π) bond are formed. These bonds constitute single and double bonds consisting of one σ-bond and one or two π-bonds in organic semiconductor. σ bonds are cylindrically symmetrical about the bond axis and formed by head-to-head overlap which has maximum electron density. π bonds are formed by side-to-side overlap because of unhybridized p orbitals. π bonds are weaker compare to σ bonds due to weaker coupling between p-orbitals. Thus electrons in these orbitals have more tendencies to delocalize. This delocalization provides fast movement of charge carriers in organic semiconductors under electric field.

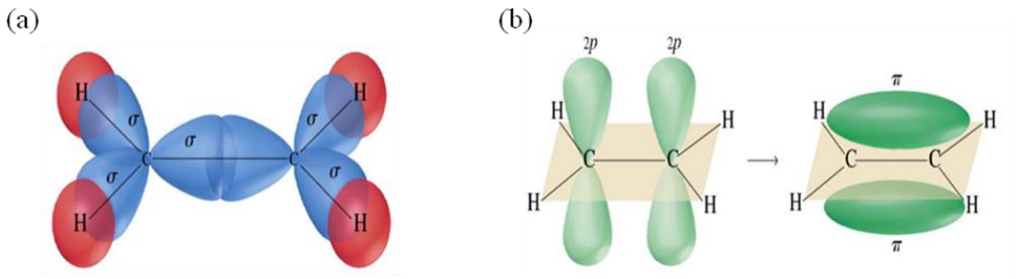

Figure 2.2 Illustration of σ (a), and π (b) bond between carbon atoms.

2.1.1. Molecular Energy Levels and Energy Bands

Wavefunctions due to the delocalization of the electrons in the molecular orbitals describe the location of an electron on the whole molecule instead of just on an atom. Because the Schrödinger equations too very complex for a system with several atoms and electrons, eigenfunctions and eigenvalues of the Hamiltonian are usually approximated by ignoring certain terms in the Hamiltonian.

The wavefunctions Ψ_n of molecular orbital can be defined as the first approximation of linear combinations of the atomic p-orbitals with wavefunctions Φ_l:

$$\psi_\pi = \sum_{l=1}^{N} \alpha_l \phi_l \qquad (2.1)$$

where N is the number of carbon atoms in the molecule, α_l is linear coefficient and sum goes over all carbon atoms (Pope and Swenberg, 1999). For N carbon atoms, we can define N molecular orbitals that are orthogonal given the hermiticity of the Hamiltonian. In the ground state of a molecule, the molecular orbitals of the lowest energies are filled with two electrons of opposite spin (Pauli-Principle). The filled molecular orbital with highest energy is then called the highest occupied molecular orbital (HOMO), whereas the molecular orbital with next higher energy contains no electron and is called the lowest unoccupied molecular orbitals (LUMO). HOMO and LUMO are corresponding to valance and conduction band edges, in inorganic semiconductor's, respectively.

2.2. Device Structures of OLEDs

OLED device operation can be understood by considering the electronic energy structure. This is necessary issue to describe operating characteristic of OLEDs. OLEDs are sandwiched structures between two electrodes. The types of device structures can be seen in Figure 2.3. The structures are usually deposited on glass substrates coated with a transparent conducting oxide as anode, as the bottom electrode upon, which the organic layers are deposited. The organic layers consist of one or more polymer fabricating by

spin coating or evaporating small molecular films, generally well below 1 μm in thickness. These organic may be composed of single or multilayer. If a single layer is used, that layer must transport both electrons and holes which emit light by recombination. These recombination properties have been difficult to achieve in a single material. Therefore in multilayer both polymer and small molecular films inserted to act as electron transport layers (ETLs) or hole transport layers (HTLs) are used to provide good carrier injection and transportation between two electrodes. Finally top electrode is formed by thermal evaporation.

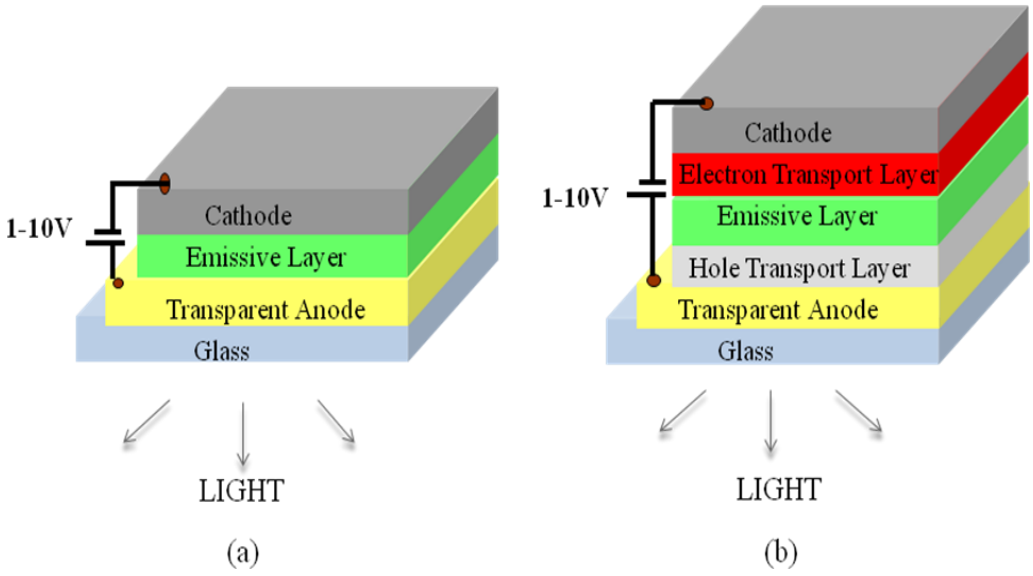

Figure 2.3. Schematic of device structure of single (a), and multilayer OLEDs.

2.3. Principle of OLEDs

OLEDs operation is similar to inorganic light emitting diodes. Holes are injected from the anode into the high occupied molecular orbital (HOMO) of the HTL, while electrons are injected from the cathode into the lowest unoccupied molecular orbital (LUMO) of the ETL by applying a voltage between two electrodes. Both electrons and holes are transported into the organic semiconductors under the formation of an exciton capable of relaxing from its excited state to the ground state by emission in emissive layer (EL) (see Figure 2.4). Each of steps is explained in more details in the following subsections.

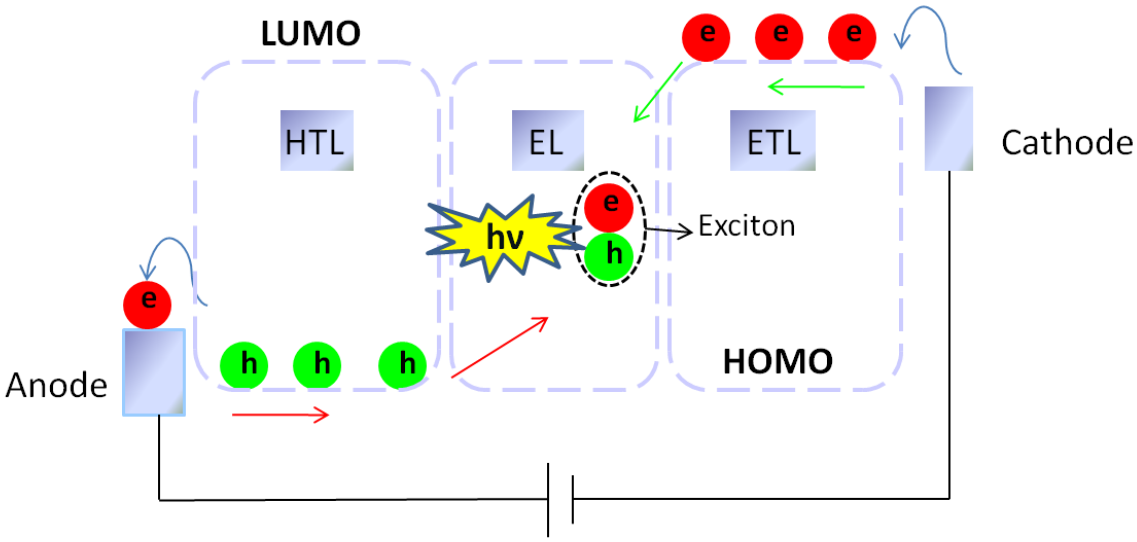

Figure 2.4. Schematic representation of OLED device operation.

2.3.1. Charge Injection

Charge carrier injection is determined by interfacial electronic properties in OLEDs. The quality of contact between metal electrode and organic semiconductor interface plays a significant role in the performance of OLEDs devices. For example, charge injection was found to be most critical factor in determining the device efficiency (Shen et al., 2004). Richardson-Schottky (RS) thermionic emission and Fowler Nordheim tunneling model were frequently used to analyze charge injection mechanism between metal and semiconductors including organic semiconductors (Donkor et al., 2001).

2.3.1.1. Richardson-Schottky Thermionic Emission

At the metal-organic semiconductor interface, if the charge carriers have a sufficient thermal energy, they can be injected to cross the barrier into the LUMO level of organic semiconductor. Under zero bias condition, at thermal equilibrium charge carriers flow from the both sides (metal $\longrightarrow$semiconductor and semiconductor $\longrightarrow$ metal) resulting in a net zero current.

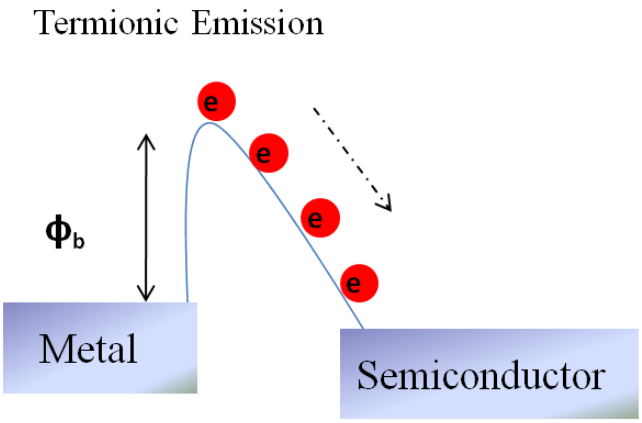

Figure 2.5. Thermionic Emission carrier injection.

Under forward voltage, the electrostatic potential across the barrier is lowered thus reducing current flow from the organic semiconductor to the metal and net current equals the difference J_{MS}-J_{SM}. The current-voltage characteristic given by (Rhoderick and Williams, 1978)

$$J = A^{*}T^{2}\exp\left(-\frac{\phi_b}{k_B T}\right) \tag{2.2}$$

$$A^{*} = \frac{4\pi q m^{*} k_B^{2}}{h^{3}} \tag{2.3}$$

Where q is the electron charge, m^{*} is the effective electron or hole mass, k_B is Boltzmann's constant, T is temperature, ϕ_b is the barrier height and A^{*} is Richardson's constant.

Basically, the Richardson law describes the charge carriers considering only the flux from both side of the contact. When the contact between the electrode and the semiconductor is established, injected electrons create in the metal side positive charge which in turns exerts an attractive force on these electrons. This is known as image

force effect. Consequently, when an electric field E exists at the interface, the actual barrier ϕ_b is lowered by amount of $\Delta\phi_b$ (Figure 2.5):

$$\Delta\phi_b = \left(\frac{e^3}{4\pi\varepsilon_0}\right)^{1/2} E^{1/2} = \beta_{RS} E^{1/2} \tag{2.4}$$

The current density becomes then Richardson-Schottky law and Figure 2.5 (Glang and Maissel, 1970).

$$J = A^* T^2 \exp\left(-\frac{\phi_b}{k_B T}\right)\exp\left(\frac{2\beta_{RS} E^{1/2}}{k_B T}\right) \tag{2.5}$$

2.3.1.2. Fowler Nordheim Tunneling

Contrary to Richardson-Schottky thermionic emission, Fowler-Nordheim mechanism disregards Coulombic effect and takes accounts tunneling through a triangular barrier created by the band bending because of the high electric field as shown in Figure 2.6.

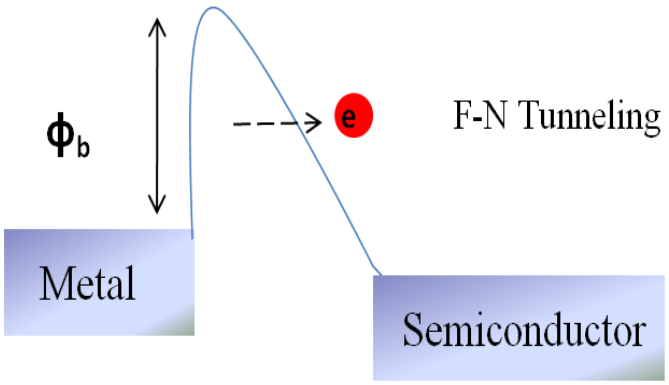

Figure 2.6. Fowler-Nordheim Tunneling carrier injection.

Carrier injection by Fowler Nordheim mechanism can be described by following equation 2.6 (Figure 2.6) (Bhandari et al., 2009).

$$J = \left(\frac{q^3 V^2 m_0}{8\pi h \phi_b m^*} \right) \exp\left(- \frac{8\pi (2m)^{0.5} \phi_b^{1.5}}{3hqV} \right) \quad (2.6)$$

where m_0 is the mass of the free electron, m^* is the effective electron or hole mass, ϕ_b is the barrier height, h is the Planck constant and V applied voltage between the anode and the cathode.

2.3.2. Space Charge Limited Current (SCLC)

Carrier transport between metal and organics layer in OLEDs can be analyzed by space charge limited current (SCLC) theories. Figure 2.7 shows bulk limited and injection limited current density versus voltage characteristic. Current density can be separated to four regimes as ohmic, space charge limited, trap charge limited and trap filled space charge limited.

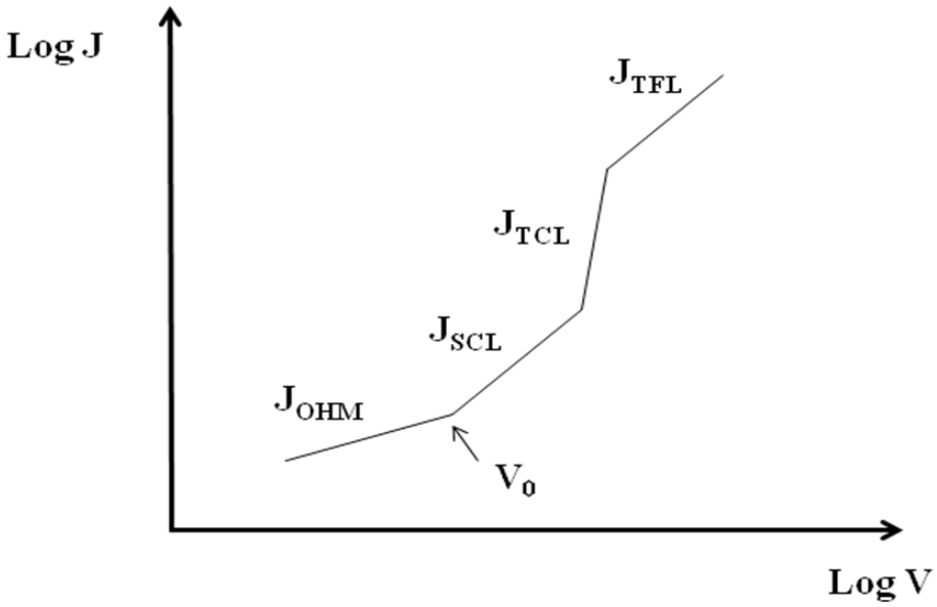

Figure 2.7. Injected limited current density versus voltage characteristic.

At lower voltages, the current is determined by the motion of free electrons which presents in the semiconductor and the current density can be explained with by Ohm's law (Shen et al., 2004).

$$J_{OHM} = eN_0 \mu \frac{V}{L} \tag{2.7}$$

where e is the charge of an electron, N_0 is the number of free electrons per unit free volume, μ is the mobility, V is the applied voltage and L is the distance between electrodes.

Threshold voltage V_0 shows the voltage at which the bulk-limited current turns from ohmic to space charge limited. As the voltage increases, charge carriers are injected than can be transported into the organic semiconductor. Injected charge carriers create a space charge at the interface between the electrode and the organic semiconductor. This is because of the low carrier mobility in organic materials, which are in the range between 10^{-5} and 10^{-3} $cm^2/(V.s)$ (Rakurthi, 2010). When the applied voltage increases, increased carrier injection into low mobility materials give rise to

charge accumulation in organic semiconductor. These charges build up result in its redistribution. This behavior of I-V is considered space charge limited regime. Space charge limited current can be explained with simple capacitor model which can be defined as following:

$$Q_{inj} \approx Q = CV \tag{2.8}$$

where Q_{inj} is the injected charge, Q is the total charge, C is the capacitance and V is the voltage. Then current density can be written as following,

$$J = \frac{Q_{inj}}{A.d} v_d \quad \text{with} \quad v_d = \mu.E = \mu \frac{V}{d} \quad \text{and} \quad C = \varepsilon\varepsilon_0 \frac{A}{d} \tag{2.9}$$

where A is the area between two electrodes, d is the distance between two electrodes, v_d is the velocity of the carriers (drift velocity), μ is the mobility, E is the electric field, ε is the dielectric constant and ε_0 is the permittivity of free space. Then, current density becomes,

$$J_{SCLC} \approx \varepsilon\varepsilon_0 \mu \frac{V^2}{L^3} \tag{2.10}$$

As a result, Mott and Gurney have shown that current behavior can be explain with SCLC and written as (Shen et al., 2004).

$$J_{SCLC} = \frac{9}{8} \varepsilon\varepsilon_0 \mu \frac{V^2}{L^3} \tag{2.11}$$

where ε is the dielectric constant and ε_0 is the permittivity of free space.

Under the high applied electric fields relatively, quite a number of carriers are injected into organic semiconductor, and fill up the trap sites in organic layer. This regime is called trap charge limited (Kim and Ha, 2008).

As soon as injected carriers fill up all the trap sites in organic layer, the additional injected carriers are free move in the presence of space charge effects only, without any influence of charge trapping. This regime is called trap filled space charge limited (Rakurthi, 2010).

2.3.3. Singlet and Triplet Excited States

An electron moves from the HOMO to the LUMO with the helping of absorption of light creating an excited state. For electrical excitation, electron and hole can be injected into the organic semiconductor. These charges migrate through the organic semiconductor until neighbouring molecules are coulombically bound. The resulting configuration is to excited state preserving spin and creating singlet exciton, electrical excitation giving rise to formation of both singlet and triplet states. Singlet (Triplet) state which is the spins of two electrons is antiparallel (parallel) and as a result total spin is a zero in units of ħ, and number of excited states in energetic order, i.e. S_1, S_2 or T_1,T_2 etc., for the energetically lowest or second lowest singlet or triplet state. Schematic representation of singlet and triplet states can be seen from Figure 2.8.

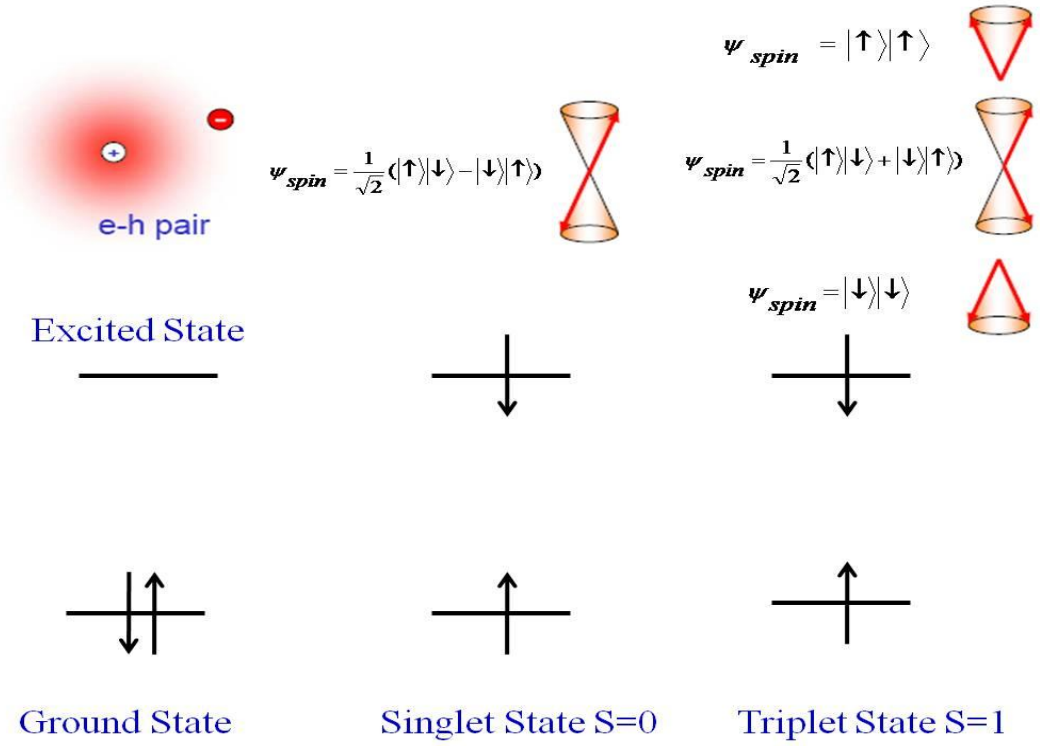

Figure 2.8. Schematic representation and vector diagram of singlet and triplet state.

Both electrons and holes can be represented by similar spin wavefunctions can be written as singlet (antisymmetric) state

$$\psi_{spin} = \frac{1}{\sqrt{2}}(|\uparrow\rangle|\downarrow\rangle - |\downarrow\rangle|\uparrow\rangle) \tag{2.12}$$

in three triplet (symmetric) state as given in the following equations;

$$\psi_{spin} = \frac{1}{\sqrt{2}}(|\uparrow\rangle|\downarrow\rangle + |\downarrow\rangle|\uparrow\rangle) \tag{2.13}$$

$$\psi_{spin} = |\uparrow\rangle|\uparrow\rangle \tag{2.14}$$

$$\psi_{spin} = |\downarrow\rangle|\downarrow\rangle \tag{2.15}$$

There are four possible spin combinations. The ratio of singlet state to triplet state should be 1:3 according to spin statistic. These vectorial illustrations of coupling between singlet and triplet spins are shown Figure 2.8.

2.3.4. Energy Transfer in OLEDs

Energy transfers from excitons formed in OLEDs play important roles to obtain more efficient devices with tunable emission color (Wu et al., 2009). These energy transfers, which are called Förster and Dexter mechanisms, ensure both singlet and triplet excitons migrations leading to charge recombination in OLEDs.

Förster energy transfer involves dipole-dipole interaction over a distance up to 10nm (Wu et al., 2009). The probability of energy transfer decays is proportional to R^{-6} where R is the distance between molecules. In Förster energy transfer, because of the spin selection role $\Delta S=0$, the spin of both D and A must be conserved. Thus the allowed singlet-singlet transitions are given as following,

$$^1D^* + {}^1A \rightarrow {}^1D + {}^1A^* \tag{2.16}$$

where the superscript 1 denotes a singlet state and the star marks an excited state.

Dexter energy transfer mechanism, a process involving by hopping among neighboring molecules through the electron exchange (Wu et al., 2009). For the electron exchange, total system spin must be conserved and, thus triplet-triplet energy transfer allowed are given following,

$$^3D^* + {}^1A \rightarrow {}^1D + {}^3A^* \tag{2.17}$$

Although singlet-singlet is also allowed Dexter transition, due to the singlet-singlet transfer is much faster and longer range, Dexter type singlet-singlet transfer is normally insignificant compared to Förster type. Both energy transfer mechanism can be seen from Figure 2.9.

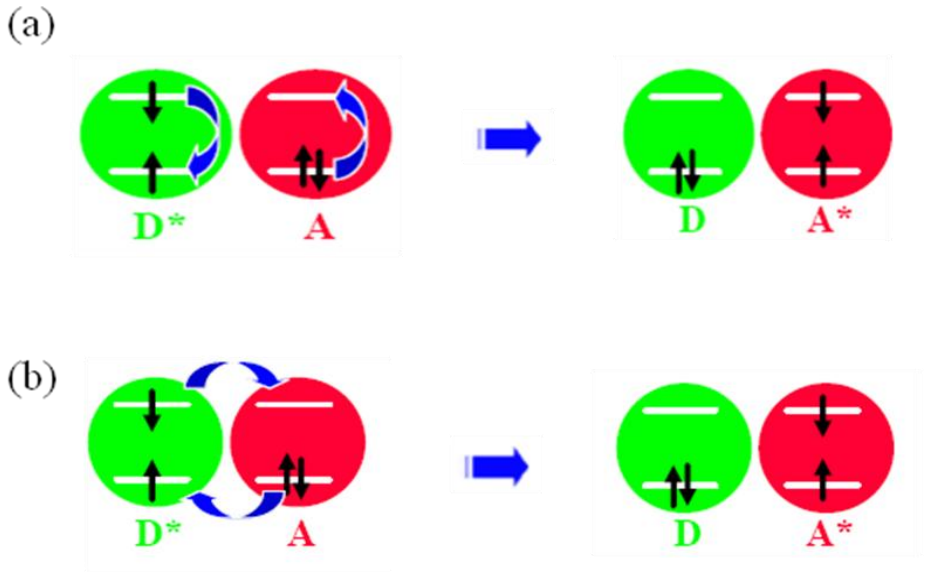

Figure 2.9. Förster (a), and Dexter (b) energy transfer in a donor-acceptor system.

2.3.5. Charge Carrier Recombination in OLEDs

After electrons and holes are injected from the anode and the cathode, the recombination of an electron and hole, leading to the emission of a photon occur in the emitting organic semiconductor layer. Recombination can be either radiative (emission of photon and phonon) or non-radiative (emission of phonon) and statistically independent, therefore electron-hole recombination is a random process.

Charge carrier recombination was already studied by Paul Langevin in 1903 (Langevin, 1903). Electron-hole pair close to each other within a distance of less than the columbic capture radius r_c where the coulomb attractive potential energy should be equals to thermal energy as follows,

$$\frac{e^2}{4\pi\varepsilon\varepsilon_0 r_c} = k_B T \tag{2.18}$$

$$r_c = \frac{e^2}{4\pi\varepsilon\varepsilon_0 k_B T} \tag{2.19}$$

where ε is the dielectric constant, ε_0 is the permittivity of free space, k_B is the Boltzmann constant and T is the temperature. Assuming that the mean free path λ of charge carriers is smaller than the coulombic capture radius ($\lambda < r_c$), and typical relative dielectric constant of organic semiconductor is $\varepsilon = 3$ with mobilities below 1 cm^2 / Vs, thus a coulombic capture radius is $r_c = 18.5$ nm (Pope and Swenberg, 1999). Electrons and holes migrate toward each other owing to the external electric field and attractive coulomb interaction in emitting organic semiconductor, until it recombines. The recombination rate, R, is given as following,

$$R = \frac{e(\mu_e + \mu_h)}{\varepsilon\varepsilon_0} n_e n_h \tag{2.20}$$

where n_e and n_h are the electron and hole densities, and μ_e and μ_h are the electron and hole mobilities respectively.

$$R = \gamma n_e n_h \tag{2.21}$$

where γ is the recombination rate factor.

2.3.6. Light Emission

As mentioned above, recombination can be either radiative or non-radiative, radiative transitions spin-singlet excited (S_1) to the spin-singlet ground state (S_0) are allowed, but spin triplet excited state (T_1) to the ground state are forbidden. These all transitions are known fluorescence and generally occur between 10^{-9} and 10^{-7} s. Radiative transition from to spin-triplet state (T_1) to the ground state is called as phosphorescence and it occurs between 10^{-6} and 1s. Both two transitions are shown in Figure 2.10.

The probability P of radiative relaxation from state ψ_i to the state ψ_j is proportional to the square of the transition dipole moment as given in the following equation.

$$P = \left| \int \Psi_i M \Psi_j \, d\tau \right|^2 \tag{2.22}$$

where M is the dipole moment operator and integration over $d\tau$ covers the whole space of all 3N coordinates with N the number of electron.

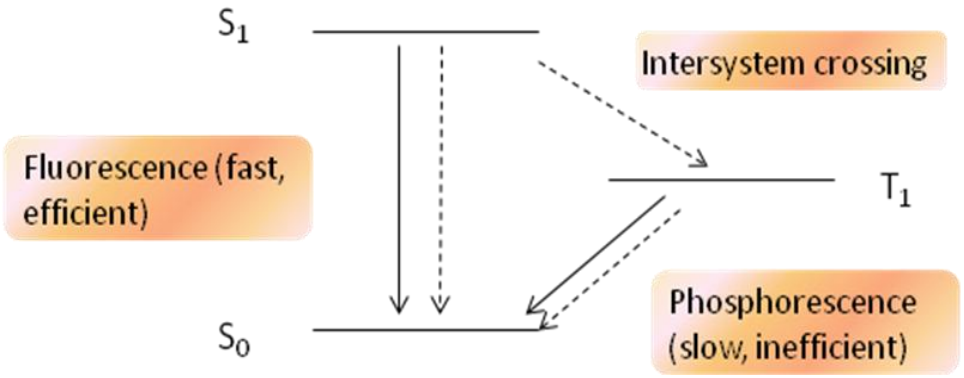

Figure 2.10. Schematic illustrations of Fluorescence and Phosphorescence. Solid and dot lines represent radiative and non-radiative decay.

2.3.7. OLEDs Efficiency

There are different parameters such as External Quantum Efficiency, Luminance, Luminance Efficiency, and Lifetime showing OLEDs device performance. In this part External Quantum and Luminance Efficiency are explained in the following subsections.

2.3.7.1. External Quantum Efficiency

External Quantum Efficiency (EQE) is defined as the ratio number of photon released from the devices and the number of charge carriers injected into devices (Shinar, 2004). A relationship between external quantum efficiency can be written as follows,

$$\eta_{ext} = \eta_{\text{int}} \eta_p = \gamma \eta_r \Phi_p \eta_p \tag{2.23}$$

where η_{ext} is the external quantum efficiency, η_{int} is the internal quantum efficiency, η_p is the light out-coupling efficiency, γ is the charge carrier balance factor (e/h), Φ_p is the photoluminance quantum yield and η_r is the efficiency of exciton production.

The light out-coupling efficiency is defined as the ratio between the number of photon emitted out from the surface in OLEDs and the number of the photon generated inside devices. Due to total internal reflection loss due to the device geometry, this ratio can be decreased. Supposing that the cathode treat like a mirror according to the simple ray theory, η_p can be obtained as following (Kim et al., 2000).

$$\eta_p \approx \frac{1}{2}\left(\frac{n_2}{n_1}\right)^2 \tag{2.24}$$

where n_2=1 is the refractive index of air and n_1=1.5 (Bansal et al., 2006) is the refractive index of organic. In this case, the out coupling efficiency can be calculated approximately 22%.

η_r is defined as the ratio of singlet exciton to the triplet excitons formed during the recombination of the injected charge carriers. As mentioned before according to the spin statistic, four possible combinations take place thus the ratio of singlet exciton to triplet exciton should be 1:3. Hence η_r has an upper limit of 25%.

γ is the probability of electron and hole recombination which are injected into devices. This parameter can be increased by different thicknesses of HTL and ETL to improve charge balance in the emitting layers.

Φ_p is defined as ratio between the number of radiative transition and the number of total transition from the excited states to the ground state.

2.3.7.2. Luminance Quantum Efficiency

‘‘The luminance efficiency or the luminance current efficiency (units in cd/A) is the ratio of the luminance (L, units in cd/m^2) of the light emitted to input current density (J, units in A/m^2). The luminance current efficiency is useful for measuring the influence of the current on the device performance’’ (Rakurthi, 2010).

2.4. Materials

Organic semiconductors can be divided into two major classes of materials, low molecular weight and polymer used for fabrication of organic and polymer LEDs. To improve device efficiency, it is necessary to obtain a high rate injection of the carriers from the electrodes and balance electrons and holes in the emissive layer to allow maximum recombination to occur. These functions require the use of the specific layers made of specific materials.

2.4.1. Hole Transport Materials (HTL)

Hole Transport Materials have delocalized holes which distributed in the molecule while electrons are localized (Rockett, 2007). Most of the hole transport materials are based on aromatic amines which have high hole mobility and electron blocking capability compare to other organic molecules. In addition, a lower binding energy of the HOMO and LUMO states make hole injection easier in these materials (Rockett, 2007). *N, N'*-diphenyl-*N, N'*- bis(3-methyphenly)-(1,1'-biphenyl)-4,4'-diamine (TPD) and *N, N'*-bis(1-napthalenyl)- *N, N'*-diphenyl)-(1,1'-biphenly)-4,4'-diamine (NPB) are frequently materials used as HTL in OLEDs as shown Figure 2.11. These materials are small molecules and can be evaporated under vacuum.

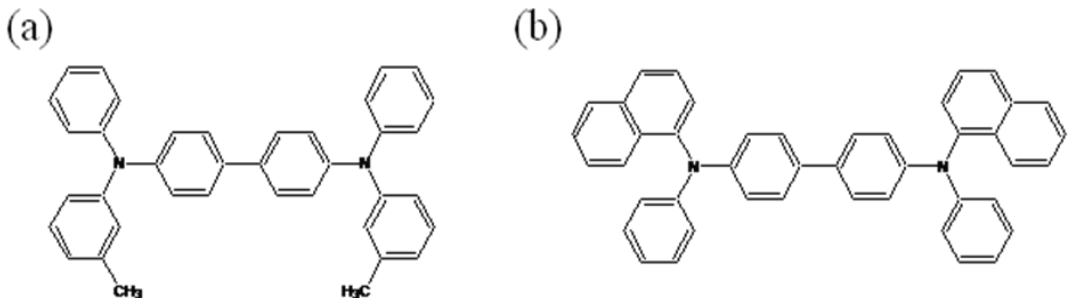

Figure 2.11. Chemical Structure of TPD (a), NPB (b).

HTL materials need to have low energy barrier between HOMO level of HTL and work function of anode to improve device efficiency and act as electron blocking layer to prevent the flow of electrons. HTL materials also should show good adhesion to the anode to provide a smooth anode surface. However they have low glass transition temperature (T_g), so they tent to crystallize leading to degradation of the devices which is currently key issue in OLEDs.

2.4.2. Electron Transport and Emissive Materials (ETL and EL)

The applications of organo-metallic compounds are very useful in OLEDs owing to both transport and emitting properties of compounds. For example, tris-(8-hydroxyquinoline) aluminum (Alq_3), tris-(8-hydroxyquinolinolato) gallium (Gaq_3) and tris-(8-hydroxyquinoline) indium (Inq_3) based materials are frequently used as both electron transport and emissive material in OLEDs shown in Figure 2.12. However Alq_3 is the most common emissive and electron transport molecule in OLEDs due to the its electronic properties such as good thermal stability, high electron affinity (3.0 eV) and ionization potential (5.95 eV).

Other common electron transport materials are bathocuproine (Kijima et al., 1999) and (bis (2-(4, 6-difluorophenyl) pyridyl-NC2') iridium (III) picolinate) or FIrpic (Adamovich et al., 2003). These materials are used as hole blocking layer.

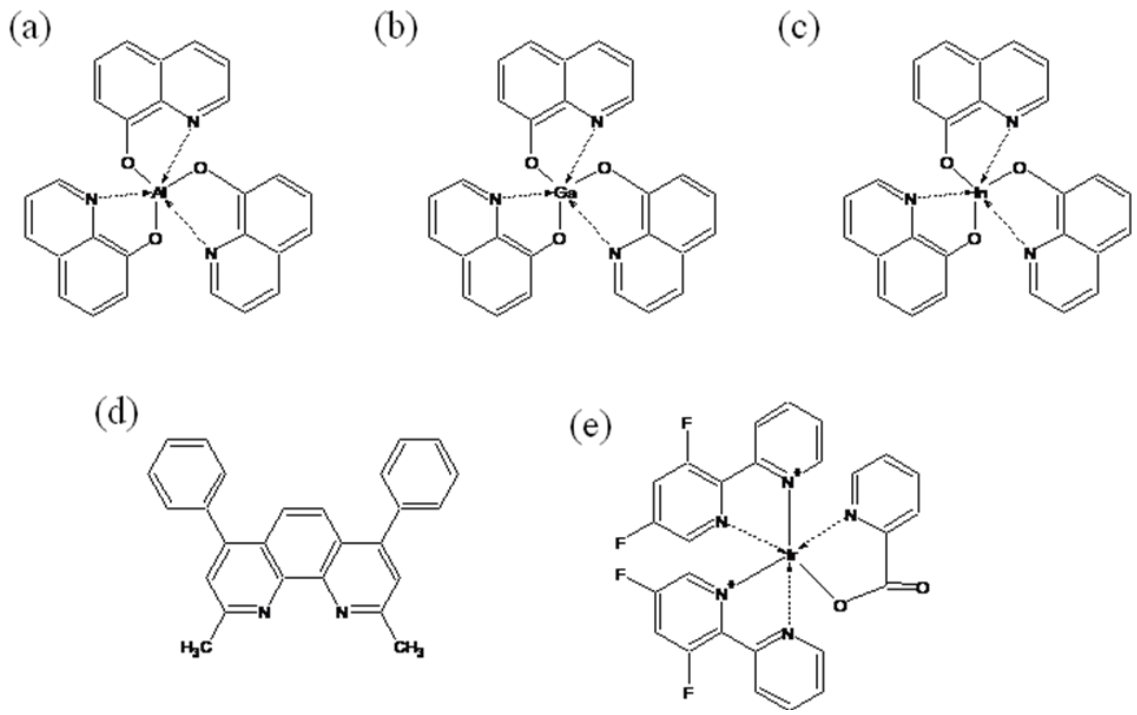

Figure 2.12. Chemical Structures of Alq_3 (a), Gaq_3 (b), Inq_3 (c), BCP (d) and FIrpic (e).

ETL and EL materials need to show good energy match between LUMO level of ETL and cathode Fermi level to provide good electron injection and also should have high mobility due to the electron mobilities in organic materials are less than hole mobilities (Kulkarni et al., 2004). ETL and EL materials should be unreactive in OLEDs operation since the having high glass transition (T_g>120 ^{0}C). This property prevents Joule heating during the operating devices. Finally they should block exciton diffusing from the anode side to cathode side.

2.4.3. Anode Materials

In typical light emitting device, one of the electrodes should be transparent for the emitted light to escape from the device, in general, transparent conducting oxides such as indium tin oxide (ITO), aluminum-doped zinc oxide (AZO) and fluorine doped tin oxide (FTO) can be used as the anode materials in OLEDs. Especially ITO is mostly utilized due to the high electrical conductivity, high transparency to visible light and large band gap over 4.0 eV (Li and Meng, 2007). ITO is highly degenerate n type semiconductor with Sn dopants and oxygen vacancies contributing to its conduction (Lee et al., 2001). The work function of ITO is about 4.8 eV which is very close to HOMO level of most HTL materials leading to increase hole injection into organic semiconductor. Work function of ITO is also quite responsive to cleaning procedures (ozone or plasma treatments) used to improve OLEDs device efficiency (Gustafsson et al., 1992).

Anode materials should be show highly conductive in order to reduce contact resistance, should have high work function to provide efficient hole injection and have good stability both thermally and chemically to prevent ion migration into organic semiconducting layer (Li and Meng, 2007).

2.4.4. Cathode Materials

Unlike the anode materials, cathode materials should have low work function such as Mg, Ca, Al, and Ba. Electrons in these materials are injected into the LUMO level of ETL easily due to the energy matching between the cathode Fermi level and

LUMO level of ETL. However any such materials are naturally reactive with oxygen and humidity giving rise to degrade OLEDs devices (Li and Meng, 2007). A solution to problem of low work function is to used the two layer cathode a thin (<5 nm) layer of Lithium Fluoride (LiF) vapor deposited onto active organic layer. Several groups shown that a thin LiF layer leads to decrease of the work function of Al (Yang et al., 2001).

2.5. Self Assembled Monolayers

Self Assembled Monolayers (SAMs) are ordered molecular structure formed by the absorption of an active surfactant on a solid surface (see Figure 2.13 b). Nuzzo and Allara are the considered the pioneers of the SAMs due to the published the work ‘‘Absorption of Bifunctional Organic Disulfides on Gold Surface’’ in 1983 (Nuzzo and Allara, 1983). They reported a new technique to form well-ordered monolayers in contrast to the well-known Langmuir-Blodgett deposition (Marrón and Luis, 2010). Since then, the preparation, formation and structure of SAMs are increasing interest in the surface engineering field. The thickness of SAMs is about 1-3 nm; these nanometer scales make SAMs suitable for studies in organic electronics and nanotechnology owing to the providing stability and controlling at interface in the molecular level. Furthermore, contrary to molecular beam epitaxy (MBE), chemical vapor deposition (CVD), and physical vapor deposition, SAM thin films are easy to prepare due to the not require ultra high vacuum.

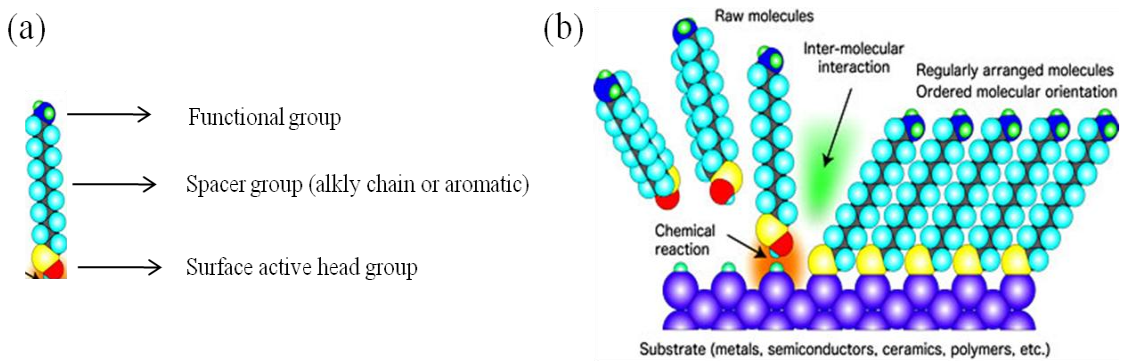

Figure 2.13. Schematic illustration of SAMs (a), Formation of Self Assembled Monolayer (b).

As can be seen Figure 2.13.a. SAMs consist of three distinctive parts: surface active head groups, spacer groups and surface functional groups. Surface active head groups should have the capability to form bond with solid surface spontaneously by chemisorption (strong chemical bond), or physisorption (weak bond). Also, surface active head group stabilize surface atoms and modify electronic states. Furthermore, the head groups provide the physical and chemical interaction of SAMs on the active device layer by using different functional groups such as -SH (thiols), SiR_3 (silanes), COOH (carboxylic acids).

Spacer groups can be aromatic or heteroaromatic structure and provide well define thickness of the SAMs. Also, spacer groups dominate electrical and optical properties of the SAMs. Surface functional groups determine surface properties of the SAMs and present chemical functional groups. Furthermore, functional groups prevent from extra layer formation.

2.5.1. Formation of SAMs

The self assembly process can take place mainly at a solid surface over a sufficient time interval to establish chemical bond. When the surface head groups approach to solid surface, the chemical bond formed by chemisorption which is the main driving force to create chemical bond on the surface. While the layers continues to form, van der Walls forces between spacer groups help pack the molecules into well ordered layer and determining surface coverage. Formation of SAMs and time affects on the SAMs formation are illustrated in Figure 2.14. For shorter times, a molecule is absorbed at the surface, it undergoes a random walk on the surface until it meets another absorbed molecule and forms island. Initial island growth is fast and linear and occurs via diffusion limited aggregation of adsorbed molecules (Doudevski et al., 1998). For higher times, coverage kinetics are slow and can be fit to Q=1-exp (-kt). Growth is limited by adsorption from the solution (Doudevski et al., 1998).

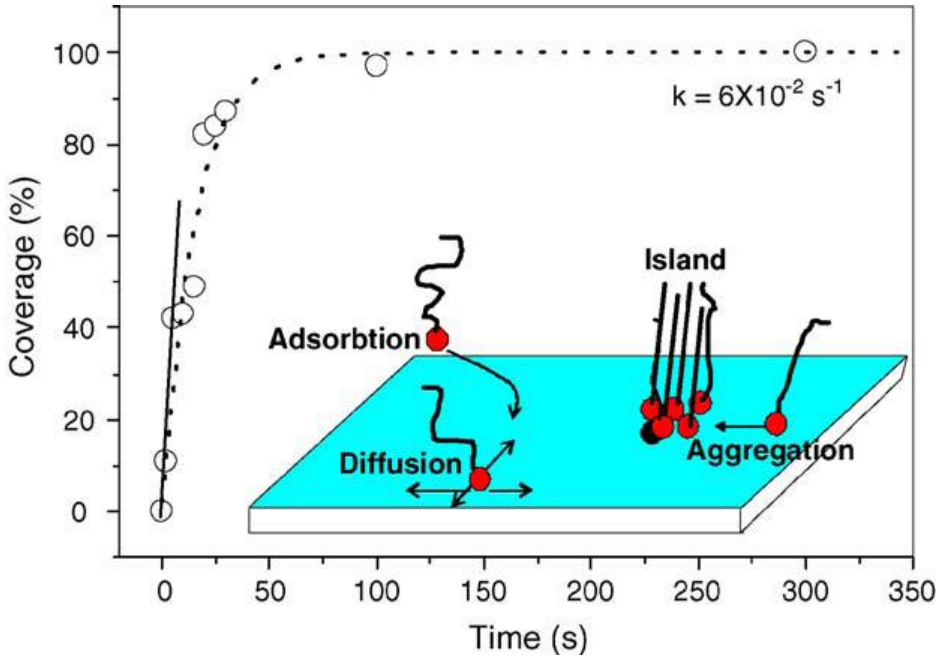

Figure 2.14. Surface coverage as a function time
(Source:(Aswal et al., 2006)).

2.6. Characterization

2.6.1. Atomic Force Microscopy (AFM)

Atomic Force Microscope (AFM) was invented by Binnig, Quate, and Gerber in 1985 as a tool for characterizing surface (Binnig et al., 1986). AFM is based on the analysis of long range Van der Waals forces and repulsive forces. The AFM operates by permitting extremely sharp tip, which is integrated into end of the cantilevers, moving above the surface under the interactive atomic forces. Thus information about the sample surface is obtained with a spatial resolution of a few nanometers by measuring deflection and torsion of the cantilever.

The fundamental idea of the AFM working principle is measurements of interactive force between tip and sample surface. The interactive forces can be explained by considering the van der Walls forces (Batsanov, 2001). Vander Walls force is occurred by dipole or induce-dipole interactions at the atomic and molecular level. These forces can be explained by taking into account two identical inert gas atoms. If they are far from each other; in other words, the distance (R) between these

two atoms is large in comparison with the radii of the atoms, the interaction force between atoms would be zero. Nevertheless, if the atoms include dipole moments in each other, induced moments cause an attractive interaction between atoms. In this case, the total energy of the system would be,

$$\Delta U = -\frac{A}{R^6} \tag{2.25}$$

As can be seen from the Equation (2.25), potential energy depends on inverse sixth-power of separation between the nearest two atoms. This is called as van der Walls interaction or London interaction (Kittel and McEuen, 1996).

The van der Walls energy of two atoms, located at a distance r from each other, is approximated by the exponential function-Lennard potential:

$$U(r) = U_0 \left\{ -2\left(\frac{r_0}{r}\right)^6 + \left(\frac{r_0}{r}\right)^{12} \right\} \tag{2.26}$$

The first term in the sum describing the attraction of long distances caused by a dipole-dipole interaction and second term considers short range repulsion owing to the Pauli Exclusion Principle. The parameter r_o is the equilibrium distances between atoms, the energy value in the minimum.

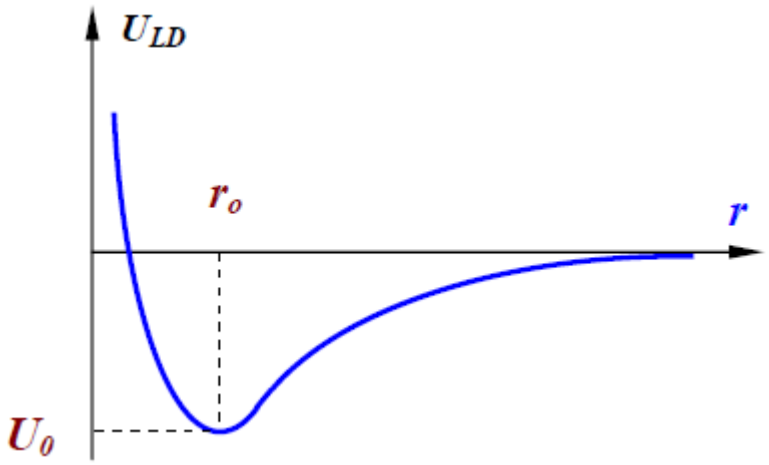

Figure 2.15. Lennard-Jones potential
(Source: Mironov 2004).

The force between the two atoms is given by –dU/dR. by using this relation, the force between two atoms at separation R can be derived from Equation (2.26), yielding

$$\vec{F}(r) = 24U_0\left[2\left(\frac{r_0}{r}\right)^{13} - \left(\frac{r_0}{r}\right)^{7}\right]\hat{r} \qquad (2.27)$$

Equation (2.27) represents the force between two atoms.

As mentioned before, the data acquisition in AFM operation can be done by recording the detection of tip movement (deflection and torsion). One of most popular method for this purpose is utilized “optical detection”. An optical detection system consists of a four-quadrant photodiode and a laser source. At first, a laser beam emitted from the source is focused on the cantilever and reflected towards to the photo diode. As the beam hits to the diode, photocurrents are created by each section of diode and these can be used to determine the tip bending due to the attractive or repulsive forces or torsion due to the lateral component of tip-sample interaction. If the reference values of photocurrent in the photodiode sections are assigned as I_{01}, I_{02}, I_{03}, I_{04} and I_1, I_2, I_3, I_4 are the currents values after change of the cantilever position, then differential currents from various sections of photodiodes $\Delta I_{i=}I_i$-I_{0i} then deflection and torsion of cantilever

can be characterized with $\Delta I_Z = [(I_1+I_2)-(I_3+I_4)]$ and $\Delta I_L = [(I_1+I_4)-(I_2+I_3)]$, respectively (Figure 2.16).

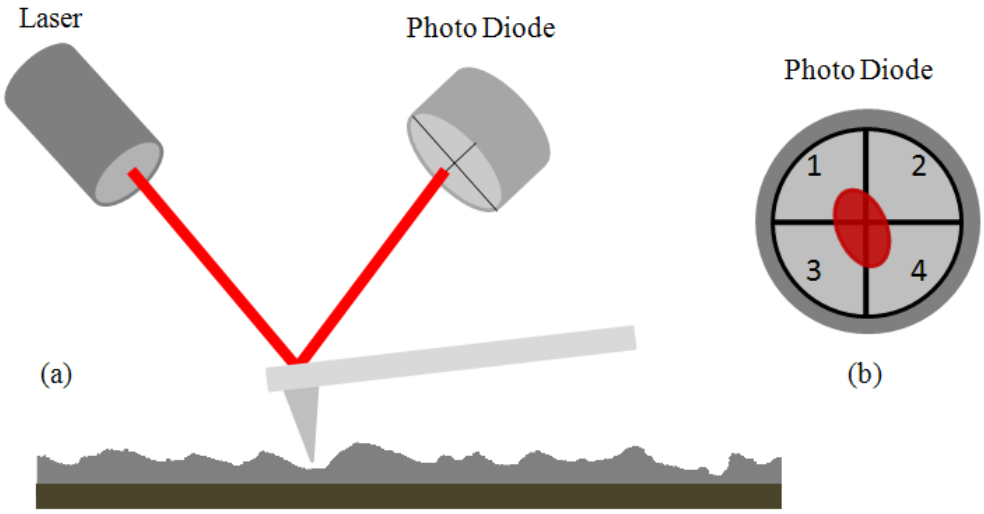

Figure 2.16. (a) Schematic description of optical detection system, (b) photodiode sections.

Feedback system is used to keep the tip-sample separation constant, and current difference (ΔI_Z) is used as input signal of feedback system in order to control the ΔZ (tip bending). To equate the value of ΔZ to the ΔZ_0 = constant (which is determined before the operation by the operator) a voltage is applied to the piezoelectric transducer (scanner) which is made of a piezoelectric material and it generates a mechanical tension in response to an applied voltage; thus, when voltage is applied to the Z electrode of the scanner, tips moves along the surface with constant ΔZ, as a result surface topography is obtained by recording the voltage on the Z electrode in computer memory and three dimensional f(x,y) graphic is achieved.

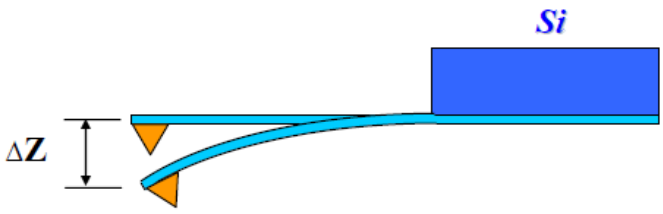

Figure 2.17. A schematic of a typical AFM tip and cantilever (Source: Mironov 2004).

AFM uses special tips mounted at the end of a cantilever to be able to detect the interaction forces, and elastic cantilevers provide sensitivity to the measurement. A schematic of a typical AFM tip and cantilever can be seen in Figure 2.17. AFM cantilevers can be made of Si, SiO_2 or Si_3N_4 by using photolithography and etching methods. According to the Hooke's Law, deflection of the cantilever can be written as;

$$F = k\Delta Z \tag{2.28}$$

where the deflection of cantilever ΔZ is determined by the acting force F and spring constant k. Another important parameter for cantilever is its harmonic frequencies; it is given by following for (Mironov, 2004) :

$$\omega_{ri} = \frac{\lambda_i}{l^2}\sqrt{\frac{EJ}{\rho S}} \tag{2.29}$$

where l is the cantilever length; E is the Young's modulus; J is the inertia moment of the cantilever cross-section; ρ is the material density; S is the cross section; λ_i is the numerical coefficient depending on the oscillation mode.

2.6.2. Kelvin Probe Force Microscopy (KPFM)

Kelvin Probe Force Microscopy are frequently used to measure contact potential difference (CPD) between conductive tip and the sample surface, thus giving information on the work function of conductive thin films (Rosenwaks et al., 2004). The CPD (V_{CPD}) between tip and sample is defined as following (Maldonado et al., 2006).

$$V_{CPD} = \frac{\phi_{sample} - \phi_{tip}}{e} \tag{2.30}$$

where ϕ_{sample} and ϕ_{tip} are the work functions of the sample and tip respectively. As can be seen from the equation 2.30, when the work function of tip is known, the work function of sample can be calculated.

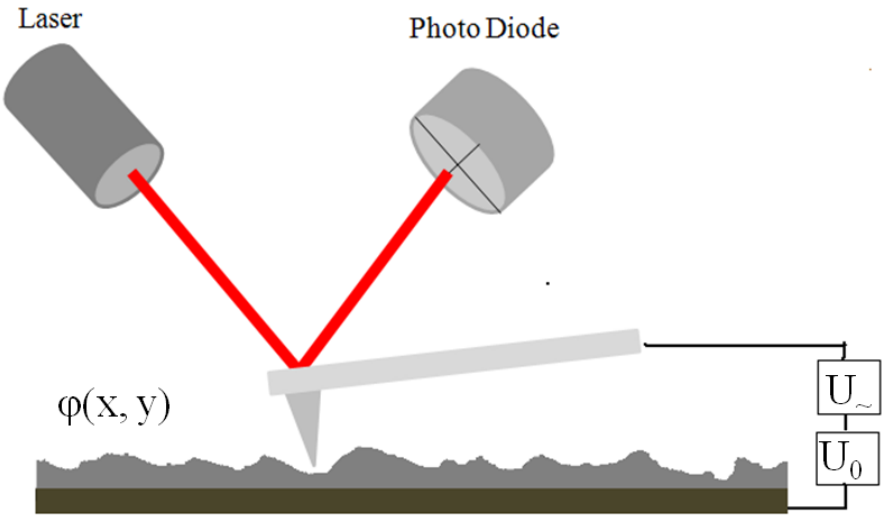

Figure 2.18. Measurements circuit of the electric tip-sample interactions (Source: Buyukkose 2009).

For KPFM measurements, during the operation, a constant voltage U_0 and a variable voltage $U_{\sim}=U_1\sin(\omega t)$ are applied to the substrate as given in Figure 2.17. When φ(x, y) is the potential distribution on the sample, the voltage between the AFM tip and surface will be

$$U = U_0 + U_1 \sin(\omega t) - \varphi(x, y) \tag{2.31}$$

and stored energy in this system will be

$$E = \frac{CU^2}{2} \tag{2.32}$$

Then electric force tip-sample interactions is

$$\vec{F} = -grad(E) \tag{2.33}$$

Z-component of the electric force between tip and surface is written as

$$F_Z = -\frac{\partial E}{\partial z} = -\frac{1}{2}U^2 \frac{\partial C}{\partial z} = -\frac{1}{2}\left[U_0 - \varphi(x,y) + U_1 \sin(\omega t)\right]^2 \frac{\partial C}{\partial z} \tag{2.34}$$

by using identity of $\sin^2(\omega t) = [1-\cos(2\,\omega t)] / 2$, electric force between tip and sample becomes,

$$F_Z = -\frac{1}{2}\left\{[U_0 - \varphi(x,y)]^2 + 2[U_0 - \varphi(x,y)]U_1 \sin(\omega t) + \frac{1}{2}{U_1}^2\left[1 - \cos(2\omega t)\right]\right\}\frac{\partial C}{\partial z} \tag{2.35}$$

This equation can be divided into three parts

$$F_{z(\omega=0)} = -\frac{1}{2}\left\{[U_o - \varphi(x,y)]^2 + \frac{1}{2}{U_1}^2\right\}\frac{\partial C}{\partial z}\ \textit{constant component;} \tag{2.36}$$

$$F_{z(\omega)} = -\left\{[U - \varphi(x,y)]\,U_1 \sin(\omega t)\right\}\frac{\partial C}{\partial z}\ \textit{component at frequency } \omega; \tag{2.37}$$

$$F_{z(2\omega)} = \left\{\frac{1}{4}{U_1}^2 \cos(2\omega t)\right\}\frac{\partial C}{\partial z}\ \textit{component at frequency } 2\omega\ ; \tag{2.38}$$

Detection of cantilever oscillation amplitude at a ω frequency gives to the surface potential distribution of sample. This technique is known as Kelvin Probe Force Microscopy (KPFM) (Mironov, 2004). Also, detection of cantilever oscillation amplitude at a 2ω frequency allows to obtaining capacitive properties of sample. This technique is called Scanning Capacitance Microscopy (SCM) (Mironov, 2004). Information on the electrical properties of the sample can be obtained using lock in amplifier which allows analyzing each of each these three signals. When ω component of electric force interaction is zero through feedback. The applied dc voltage (U_0) equals to surface potential ($\varphi(x, y)$)=($U_0 = \varphi(x, y)$).

KPFM surface potential characterization was performed two pass techniques, in the first pass, surface topography images were obtained in the semicontact mode of operation (see Figure 2.19 a). Then in the second pass the probe was retracted above the surface at the height dZ and surface potential topographies were obtained (see Figure 2.19 b).

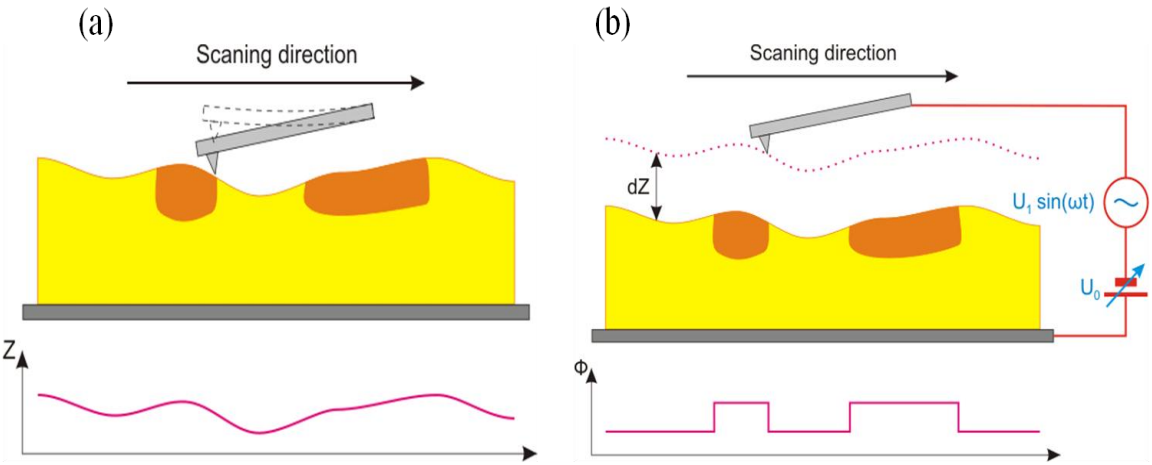

Figure 2.19.First (a) and second (b) pass techniques schematic
(Source: Mironov 2004).

2.6.3. Scanning Tunneling Microscopy (STM)

Scanning Tunneling Microscopy was invented in by Binnig, Quate, and Gerber in 1982 (Binnig and Rohrer, 1983). Since invention, the STM has become widely used tool due to allowing atomic scale resolution. The STM working principle is based on

quantum mechanical tunneling of electrons between metal tip and conductive sample surface. When STM tip is brought close to the sample to the distances of several Angstroms, electrons can tunnel through the gap from the tip to sample. The tunneling current depends exponentially on the tip-sample separation barrier as shown in equation 2.39.

$$I \propto e^{-2\kappa z} \tag{2.39}$$

where κ is decay constant and z is the barrier width. As can be seen equation 2.39, the tunneling current increases with decreasing barrier which allows exquisite resolution in STM measurements. In the case of the tunneling between tip and sample, the decay constant is

$$\kappa = \frac{4\pi\sqrt{2m\varphi^*}}{h} \tag{2.40}$$

where m is electron mass, φ^* average work function ($\varphi^* = (\varphi_{Tip}+\varphi_{Sample})/2$) and h is the Planck constant. Then current density becomes,

$$J = J_0(V)e^{-\frac{4\pi}{h}\sqrt{2m\varphi^* z}} \tag{2.41}$$

The value of the J_0 (V) does not dependent on the tip-sample distance. STM uses a feedback system to keep the tunneling current at the constant value (I_0), determined before operation by operator. To control the current value and a consequently tip-sample distance, a voltage is applied to the Z electrode of the scanner and STM surface topography is obtained by recording in the computer memory as a Z=f(x,y) function.

For the STM measurements, surface topography is formed either constant current mode or constant height mode. In the constant current mode, STM tip moves over the surface at a constant value of tunneling current and surface topography is obtained. In the constant height mode, STM tips moves over the surface at a constant height and surface topography is obtained by recording tunneling current changes.

STM tips should be made of conductive material so tungsten wire is commonly used in STM measurements. STM tip is manufactured by electrochemical etching or cutting a wire by using scissor.

2.6.4. Cylic Voltammetry (CV)

Cylic Voltammetry is significant tool to study the electrochemistry on a surface. Therefore it has been widely used to investigate the monolayer structure. This technique can determine the charge transfer process at the interface which is influenced by the nature of the electrode surface (Marrón and Luis, 2010).

A CV system contains an electrolysis cell, a potentiostat, a current voltage converter, and a data acquisition system as shown in Figure 2.20. The electrolysis cell contains working electrode, counter electrode, reference electrode and electrolytic solution. The working electrode's potential is changed linearly with time, while the reference electrodes keep a constant potential.

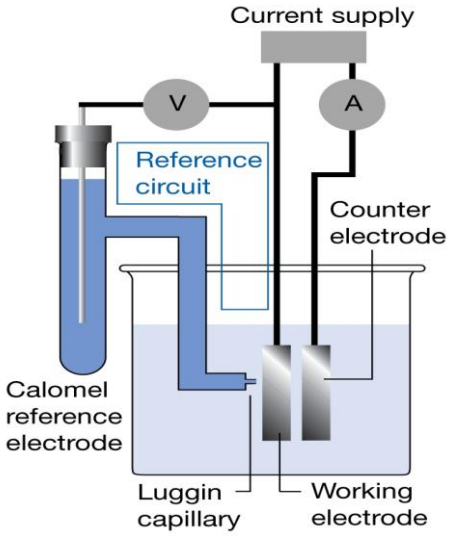

Figure 2.20. The representation of Electrochemical cell.

The counter electrode conducts electricity from the signal source to the working electrode. Electrolytic solution provides ions to the electrodes during oxidation and reduction. A potentiostat is used as a dc power source to produce potential, while allowing small currents into the system without changing the voltage. The current to voltage converter measures the resulting current and the data acquisition system produces the resulting voltammogram.

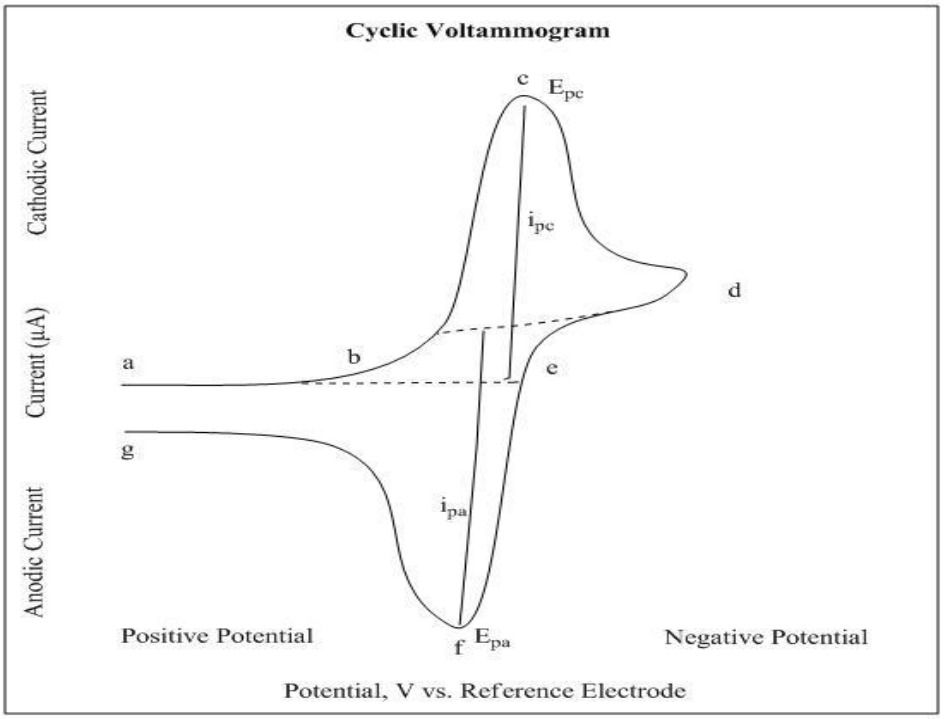

Figure 2.21. Voltammogram of a Single electron oxidation-reduction.

Figure 2.21 shows a cyclic voltammogram resulting from a single electron reduction and oxidation. The reduction process takes place from (a) initial potential to (d) switching potential. In this region, the potential is scanned negatively to lead a reduction. The resulting current is called cathodic current (i_{pc}). The corresponding peak potential takes place at (c), and is called cathodic peak potential (E_{pc}). The E_{pc} is reached when the substrate at the surface of the electrode has been reduced. After the switching potential has been reached (d), the potential is scanned positively from (d) to (g) to lead a oxidation. This resulting current is called anodic current (I_{pa}). The

corresponding peak potential at (f) is called the anodic peak potential (E_{pa}), and is reached when the substrate at the surface of the electrode has been oxidized.

Formal reduction Potential (E^0) for a reversible couple is centered between the anodic peak potential (E_{pa}) and cathodic peak potential (E_{pc}) (Zurowski, 2009):

$$E^0 = \frac{E_{pa} + E_{PC}}{2} \tag{2.42}$$

As a result, Cylic Voltammetry can be used to obtain information about electrochemical processes under various conditions, such as oxidation-reduction reactions, the reversibility of a reaction. CV can also be used to determine stoichiometry of a system, formal reduction potential.

CHAPTER 3

EXPERIMENTAL DETAILS

This chapter consists of two main parts. In the first part, both preparation of two new synthesized SAM molecules and fabrications of organic thin films were explained. In the second part, Atomic Force Microscopy, Kelvin Probe Force Microscopy and Scanning Tunneling Microscopy were used to characterize the modified and unmodified ITO surfaces.

3.1. Sample Preparation

Our sample preparation procedure includes synthesis of SAM molecules, preparation of SAM molecules, etching and cleaning of ITO substrates and thermal evaporation of organic and cathode layers.

3.1.1. Synthesis of SAM Molecules

In this work, 5-[(3-methylphenyl) (phenyl) amino] izoftalic acid (MePIFA) and 5-(diphenyl) amino] izoftalic acid (DPIFA) aromatic small molecules with double bound carboxylic acid have been used as self-assembly monolayer (SAM). The synthesis procedures for SAM molecules are described as follows: For MPPBA molecule, to a solution of dimethyl 5-iodobenzene 1, 3-dicarboxylate (0.5 g, 1.56 mmol) and 3-methyl-N-phenylalanine (0.29 g, 1.56 mmol) in toluene (1.5 ml), $Na^{t}BuO$ (0.18 g, 1.87 mmol), $Pd_2(dba)_3$ (0.033g, 36 μmmol) and $P(^{t}Bu)_3$ (0.032 g, 36 μmmol) were added in the given sequence and then follow by adding toluene (1.0 ml) again. After that, while keeping the solution under a vigorous mixing, it was heated in oil bath to reach to the temperature at 100 ^{0}C and keeping overnight in this solution. Thereafter the solution of ammonia (NH_3) (1N, 15 ml) was added and mixture was stirred at room temperature. This mixture was extracted with chloroform ($CHCl_3$) (50ml). At the end, the crude material was obtained and ethanol (18ml) was added. In an aqueous solution

of Sodium Hydroxide (NaOH) (1N, 18 ml), this crude material was boiled for an hour. Finally deionized water (22 ml) and Hydrochloric acid (HCl) (1M, 22 ml) were added in to the cooled mixture at room temperature. To obtain MePIFA SAM molecule, the collapsing material was collected by filtering and to be dried under vacuum.

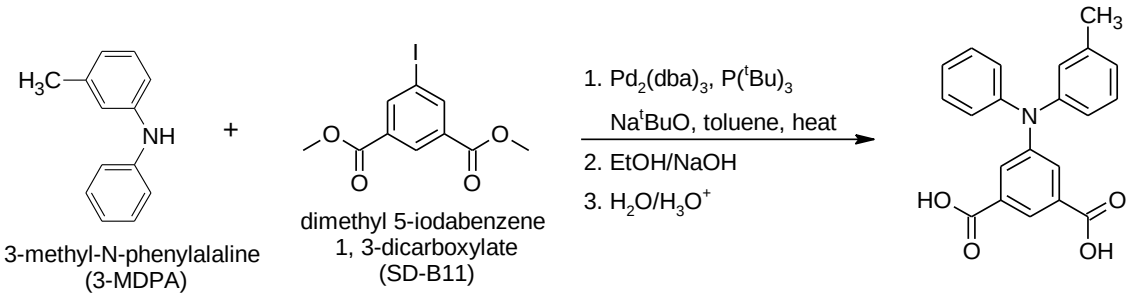

Figure 3.1. Synthesis procedure of a double bond carboxylic acid based (MePIFA) SAM molecule.

For DPIFA molecule, to a solution of dimethyl 5-iodobenzene 1, 3-dicarboxylate (0.5 g, 1.56 mmol) and diphenylamine (0.26 g, 1.56 mmol) in toluene (1.5 ml), Na^{t}BuO (0.18 g, 1.87 mmol), $Pd_2(dba)_3$ (0.033g, 36 μmmol) and P(^{t}Bu)$_3$ (0.032 g, 36 μmmol) were added in the given sequence and then again toluene (1.0 ml)added. After that, while keeping the solution under a vigorous mixing, it was heated in oil bath to reach to 100 ^{0}C temperature and waited overnight in this solution. Thereafter, the solution of ammonia (NH_3) (1N, 15 ml) was added and mixture was stirred at room temperature. This mixture was extracted with chloroform ($CHCl_3$) (50ml). At the end, crude material was obtained and ethanol (18ml) was added. In an aqueous solution of Sodium Hydroxide (NaOH) (1N, 18 ml) this crude material was boiled for an hour.

Finally deionized water (22 ml) and Hydrochloric acid (HCl) (1M, 22 ml) were added into the cooled mixture at room temperature. To obtain 5-(Difenil) amino] izoftalic acid (DPIFA) SAM molecule, the collapsing material was collected by filtering and was dried under vacuum.

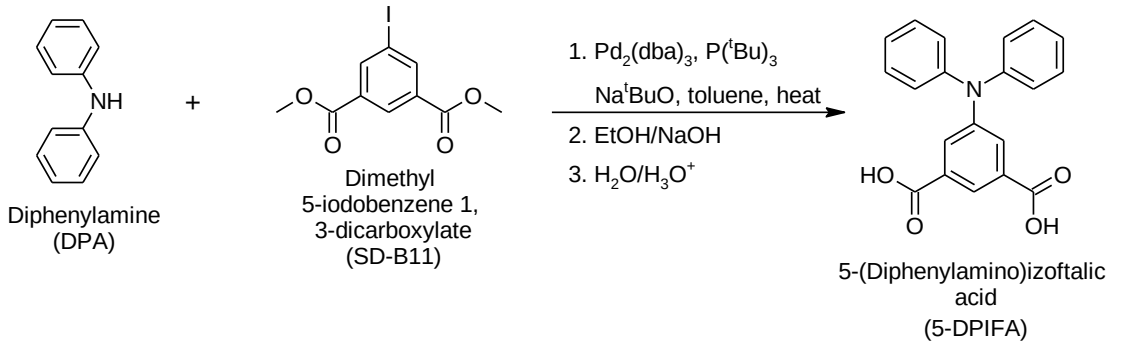

Figure 3.2. Synthesis procedure of a double bond carboxylic acid based (DPIFA) SAM molecule.

3.1.2. Preparation of SAM molecules

Preparation conditions are the important keys to obtain high quality SAM monolayer. Monolayer formation takes place by immersing of surface active material into a solution. In this study, 5-[(3-methylphenyl) (phenyl) amino] izoftalic acid (MePIFA) and 5-(Difenil) amino] izoftalic acid (DPIFA) aromatic small molecules with double bound carboxylic acid have been used as self-assembly monolayer (SAM) to modify ITO surface. Both MePIFA and DPIFA SAM molecules with 1mM were prepared at room temperature in methanol solution.

3.1.3. Etching and Cleaning Procedure of ITO Substrates

Etching process is the first step in OLED fabrication. First of all the ITO glass substrates were purchased from Sigma Aldrich with a 15-25 Ω/sq surface resistivity. After that the 1.4x1.4 cm ITO coated glass substrate were cut using a diamond pencil. Next, ITO is covered with Scotch tape about 0.3 cm lengths to define cathode and prevent from damaging during the etching process. Thereafter zinc powder was poured on uncovered ITO. Finally ITO was etched by dropping 20% diluted HCl solution on zinc powder ITO.

After etching, ITO substrates were cleaned with detergent solution and then sonicated for 15 min in deionized water, acetone, ethanol and isopropanol respectively.

3.1.4. Modification of ITO Surface by SAM Technique

After etching and cleaning procedure were completed, ITO substrates were kept in 1mM methanol-SAM solutions for 48 hours to be completed MePIFA and DPIFA monolayers. A chemical bounding occurred on hydroxyl-rich ITO surfaces from the double bond carboxylic acid head group of MePIFA and DPIFA molecules. The ITO substrates were then rinsed with pure methanol to remove the residual MePIFA and DPIFA molecules from the ITO surfaces and finally dried in stream of Nitrogen (N_2) gas.

3.1.5. Thermal Evaporation of Organic and Cathode Layers

In this study, organic small molecules and cathode layers were deposited by two different thermal evaporator systems (NANOVAK from Ankara). These two thermal evaporation systems can be seen from Figure 3.3.

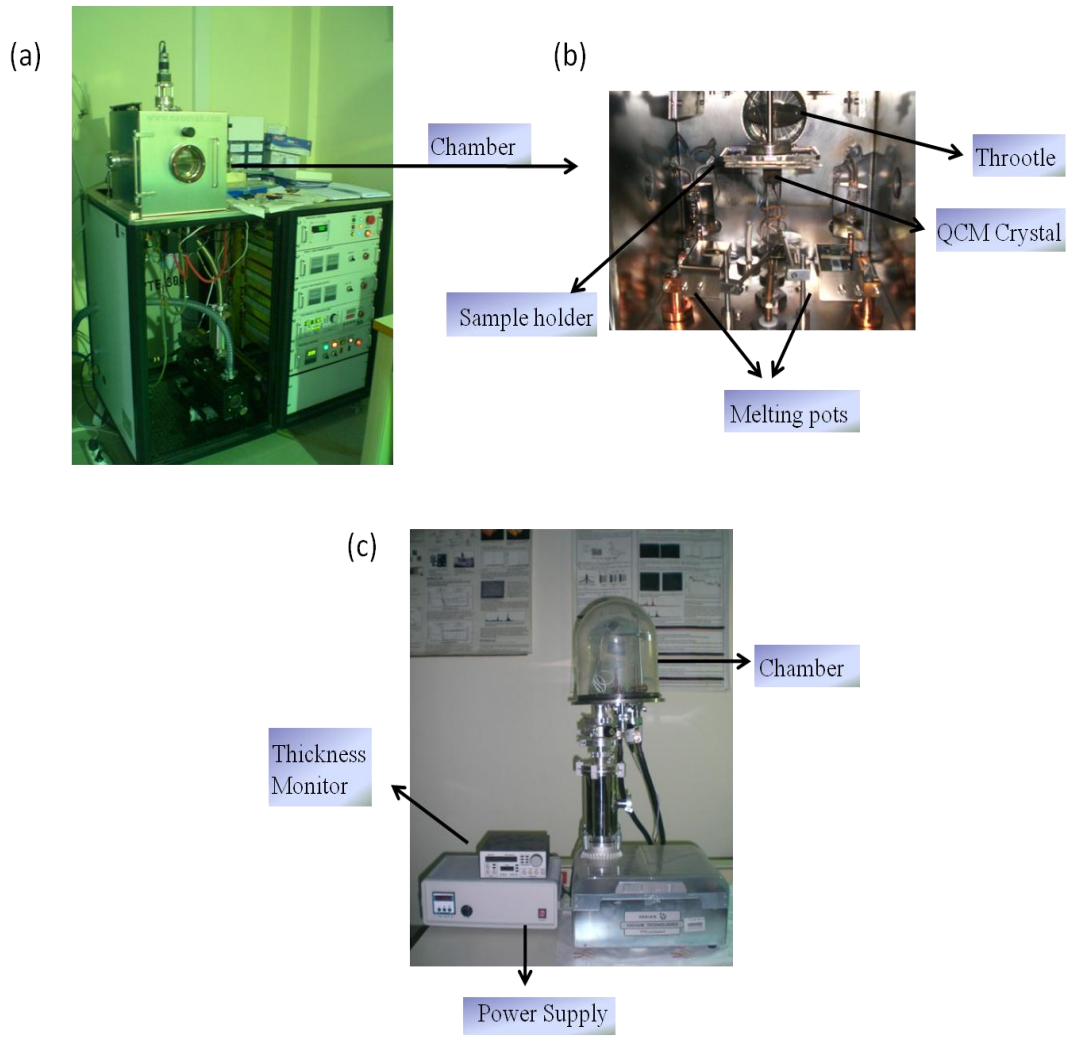

Figure 3.3. (a) and (b) Evaporation system for metallic materials, (c) Evaporation system for organic materials.

Before depositions, the thickness monitors were calibrated using a profilometer (DEKTAK from VEECO) and contact AFM cross section technique for both organic and inorganic thermal evaporator systems. In organic evaporation system, the etched ITO substrates were placed on substrate holder and the organic small molecules (TPD, NPB and Alq_3) were placed in boats connected to electrodes. Before the deposition, mask 1 was used to require area gets coated with organic materials as shown Figure 3.4.a. The depositions were started under the base pressure of $4x10^{-5}$ Torr to have good quality thin films. The rate of the deposition and thickness was monitored by using a quartz crystal microbalance (QCM) thickness monitor. After deposition of organic molecules, the thermal evaporation system shown in Figure 3.3.c was used to create

cathode layer of OLEDs devices. Before the deposition of Al, mask 2 was used as shown Figure 3.4.b.

Figure 3.4 (a) Mask 1 for organic evaporation, (b) Mask 2 for metal evaporation.

In this work, two different sets of OLED devices were fabricated in order to explore effect of SAM modification of ITO surface on electrical and optical characterization of the devices at each runs. These device configurations are shown in Table 3.1 and 3.2.

Table 3.1. Configuration of 1st set of OLED devices.

	Transparent Anode	**Hole Injection Layer**	**Hole Transport Layer**	**Emissive and Electron Transport Layer**	**Electron Injection Layer**	**Cathode Layer**
Device 1	ITO	-	TPD (60 nm)	Alq_3 (40 nm)	-	Al (125 nm)
Device 2	ITO	MePIFA (~1 nm)	TPD (60 nm)	Alq_3 (40 nm)	–	Al (125 nm)
Device 3	ITO	DPIFA (~1 nm)	TPD (60 nm)	Alq_3 (40 nm)		Al (125 nm)

Table 3.2.Configuration of 2st set of OLED devices.

	Transparent Anode	**Hole Injection Layer**	**Hole Transport Layer**	**Emissive and Electron Transport Layer**	**Electron Injection Layer**	**Cathode Layer**
Device 4	ITO	-	NPB (60 nm)	Alq_3 (40 nm)	-	Al (125 nm)
Device 5	ITO	MePIFA (~1 nm)	NPB (60 nm)	Alq_3 (40 nm)	–	Al (125 nm)
Device 6	ITO	DPIFA (~1 nm)	NPB (60 nm)	Alq_3 (40 nm)		Al (125 nm)

3.2. Characterization

Both surface and electrical characterizations of modified and unmodified ITO were performed via Atomic Force Microscopy (AFM), Spreading Resistance Microscopy (SRM), Kelvin Probe Force Microscopy (KPFM) and Scanning Tunneling Microscopy (STM). For surface characterization, surface topography images were obtained in semi-contact mode. For electrical characterization, SRM and KPFM were performed in contact and semi-contact mode by using two pass techniques. Finally STM was used to measure tunneling current between tip and thin films. For electrical and optical characterization of OLEDs devices, Labview™ and Ocean Optic were used.

3.2.1. AFM Surface and Electrical Characterization

AFM surface characterization was performed in semi-contact (tapping) mode operation using commercial Scanning Probe Microscopy instrument (Solver Pro 7 from MNT-MDT, Russia). Our experimental setup is shown in Figure 3.5. The AFM system was placed on a vibration isolation table to prevent the mechanical vibrations from the environmental noise. Optical camera integrated into the system sends the image to the computer screen and helps to define the tip position on the sample. Also, the laser source and photodiode which are essential parts of optical detection system in the AFM can be seen from the same Figure 3.5.

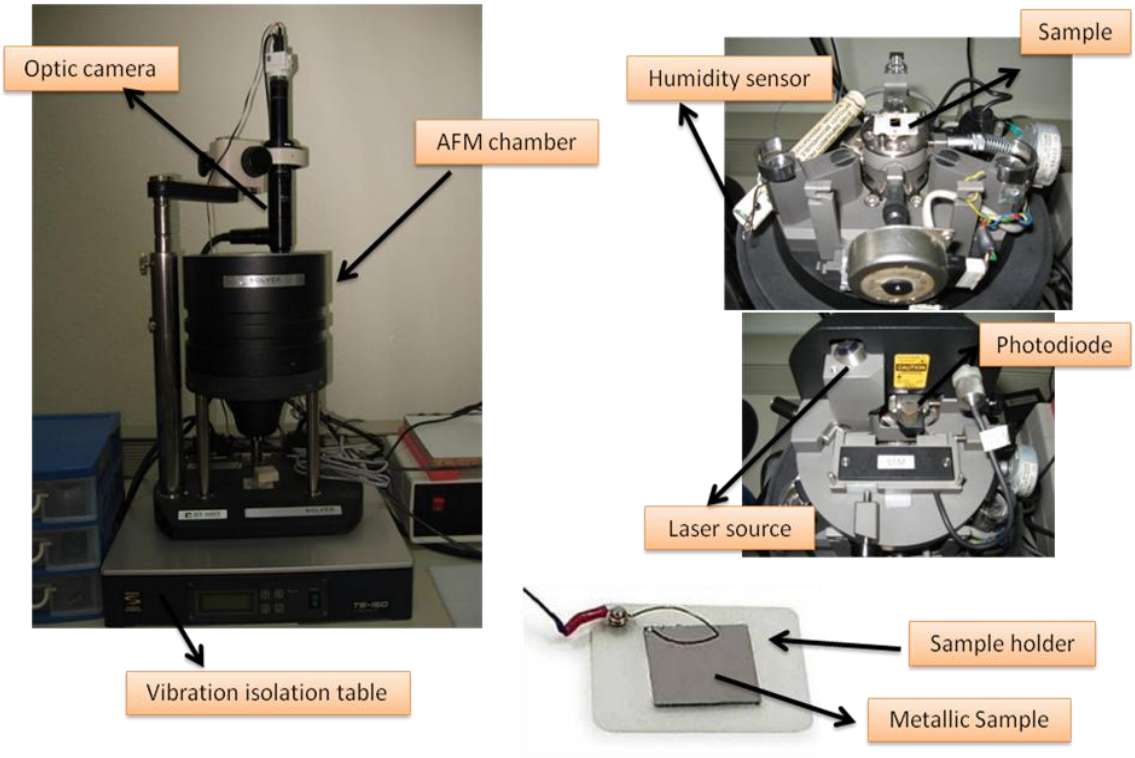

Figure 3.5. AFM set up
(Source : Buyukköse 2009).

During all the scans, a golden silicon tip with a curvature of 10 nm was used. Surface topography measurements were performed on modified ITO, unmodified ITO and organic thin films.

To obtain local resistance of map on the surface of modified ITO with MePIFA and DPIFA SAM molecules and unmodified ITO, Spreading Resistance Microscopy was performed in the contact mode operation by using Pt coated conductive AFM tip. In the SRM, a voltage applied between conductive AFM tip and sample surface while the tips moves over the sample surface. During the scan, the spreading resistance topography is obtained by recording current passing through the tip in the computer memory as a Z=f(x,y) function. In our study, we applied 0.5V between conductive tip and sample surface and I-V curves were obtained for SAM modified ITO with MePIFA and DPIFA and bare ITO.

3.2.2. KPFM Surface Characterization

For KPFM measurements, conductive AFM tip should be used to generate electrical force between tip and sample. In this work, TiN coated conducting AFM tip with a curvature of 35nm was used. To apply voltage between AFM tip and sample surface, a special sample holder with contact electrode was used. Figure 3.6 shows the special sample holder design. After the surface topography was obtained for each of the samples, feedback was broken in the second pass and detection of oscillation amplitude at ω frequency goes to zero with the feedback loop by changing the applied dc (U_0) voltage. As a result contact potential difference between AFM tip and each of the samples was found from the oscillation amplitude at ω frequency versus applied bias voltage.

3.2.3. STM Surface and Electrical Characterization

To investigate surface and electrical characterization of modified ITO, unmodified ITO and organic thin films, scanning tunneling microscopy (STM) was performed in constant current mode operation using commercial Scanning Probe Microscopy instrument (Solver Pro 7 from MNT-MDT, Russia). The STM experimental setup is shown in Figure 3.5. To apply voltage between STM tip and sample surface, a special sample holder with contact electrodes was used. Figure 3.5 shows the special sample holder design. This sample holder was used during all the

STM characterizations. 0.3V was applied to the sample with a set point of 0,121nA. After the STM surface topography was obtained for each of the samples, I-V curves were measured in every point of selected area by applying a voltage between -0.5V to 0.5V and then average I-V curves were calculated for each sample.

3.2.4. Cylic Voltammetry Characterization

Cylic voltammogram of MePIFA and DPIFA molecules (in solution) and MePIFA and DPIFA coated on ITO were obtained. As a working electrode, Pt ring; a counter electrode Pt wires and reference electrode Ag/AgCl were used. The scanning rate was 200mV/s. The Ferrocene (Fc) was internal standard. CV measurements were performed by CH660B model potentiostat from CH Platinum wire (Pt), glassy carbon (GCE) and Ag/AgCl electrode were used as counter (CE), working (WE) and reference (RE) electrodes, respectively. 0.1 M $TBAPF_6$ in acetonitrile solution was used as supporting electrolyte. Sweep rate kept constant at 0.2 V/s. Ferrocen/Ferrocenium couple was used as internal reference.

3.2.5. Electrical Characterization of OLEDs Devices

In order to obtain I-V characteristic of OLEDs devices, Keithley 236 source-meter with a connector was used to apply a voltage to anode and cathode electrodes of OLEDs device. I-V characteristic of OLEDs device was monitored on computer screen via electrical characterization program created with LabView^{TM} software (see Figure 3.6).

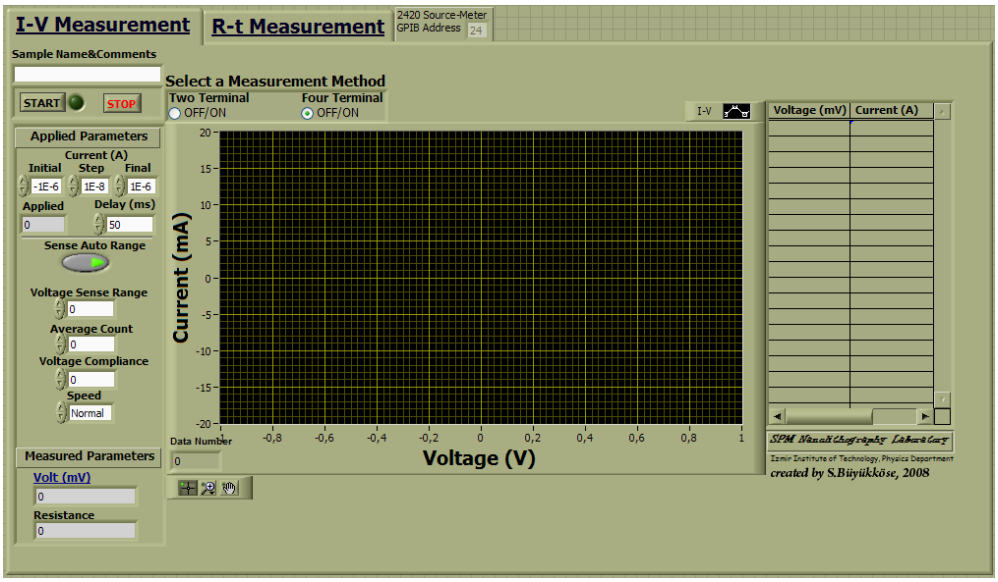

Figure 3.6. I-V program created with LabView™.

CHAPTER 4

RESULTS AND DISCUSSION

This chapter contains three parts including surface, electrical and optical characterization. The first part is the analyses of Atomic Force, Kelvin Probe Force and Scanning Tunneling Microscopy on modified ITO and unmodified ITO. Next, we have characterized electrical properties of modified and unmodified ITO using Spreading Resistance Microscopy and Scanning Tunneling Spectroscopy (STS). Electrical characterization of OLEDs devices were presented in chapter 4.5. Finally, optical properties of OLEDs devices were characterized using Ocean Optics which presented in chapter 4.6.

4.1. Surface Characterization Results

Here, we present the results of surface characterization measured with Atomic Force, Kelvin Probe Force and Scanning Tunneling Microscopy of unmodified ITO, modified ITO and organic thin films.

4.1.1. Atomic Force Microscopy Results

The surface morphology of unmodified and modified ITO was characterized by AFM images as shown in Figure 4.1. From the images, the unmodified ITO has a regular granular morphology but the modified ITO with SAM (MePIFA and DPIFA) has disrupted morphology or more dense structure. Since both modified and unmodified ITO films show rough surfaces, SAM molecules on ITO surface cannot be clearly observed. However, surface roughness (RMS) measurements differences may give some indication about the modification of ITO surface with MePIFA and DPIFA SAM. The results of surface roughness are given below in Table 4.1.

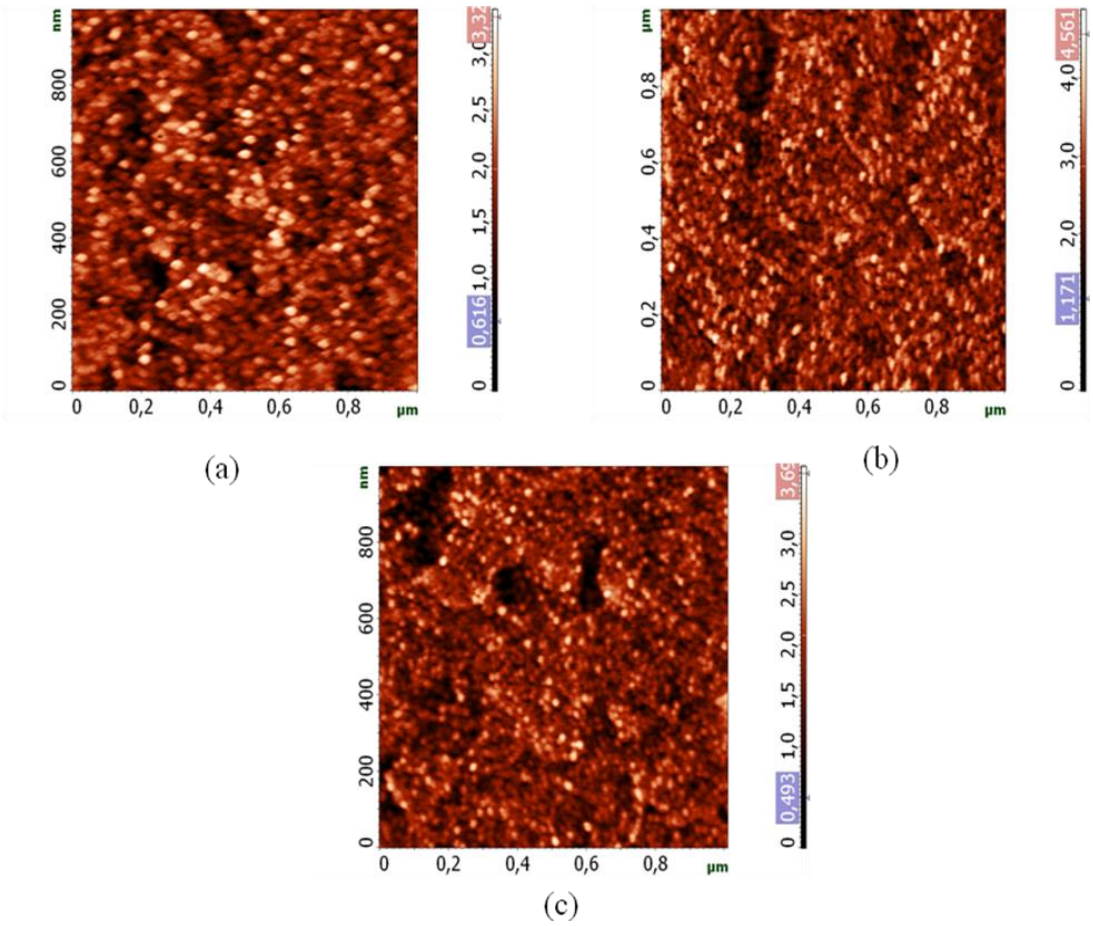

Figure 4.1. AFM images of bare ITO (a), modified ITO with MePIFA (b) and DPIFA (c) SAM molecules.

Table 4.1. Roughness values of bare ITO and modified ITO with MePIFA and DPIFA.

	Bare ITO	**ITO-MePIFA**	**ITO-DPIFA**
Roughness (RMS)	~0,468nm	~0,567nm	~0,490nm

Modified ITO with MePIFA and DPIFA SAM has a higher surface roughness than unmodified ITO. Since extra formation or aggregation may be occurred on ITO surface due to physical or chemical interactions with SAM molecules.

Si wafers with native oxide were used to compare with ITO substrate for the monolayer characterization (Lee et al., 2002). Since ITO has a rough surface and its surface morphology is not appropriate for surface roughness characterization of SAM

monolayers on ITO. On the other hand, It has been reported that both Si wafer and ITO have a similar surface density of reactive sites (about 10^{-6} mol m^{-2}) (Lee et al., 2002).

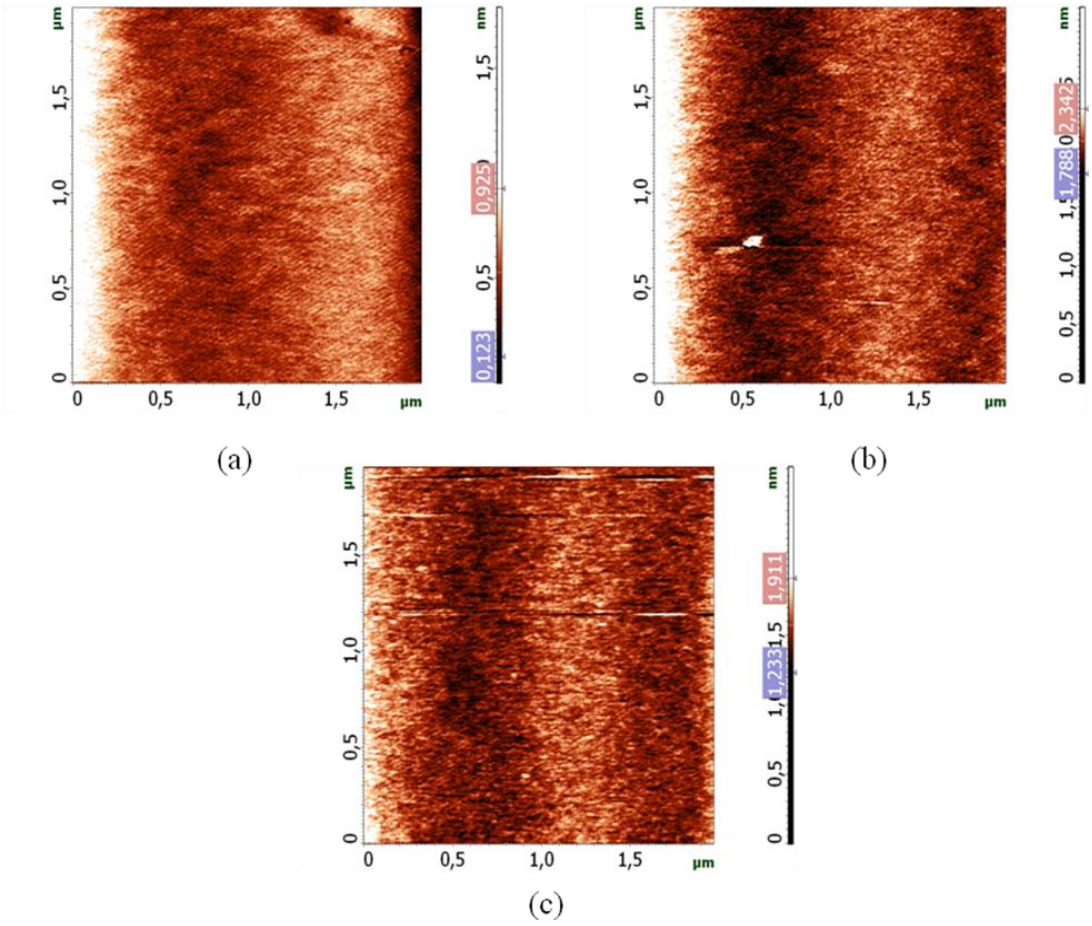

Figure 4.2. AFM images of bare Si (a), modified Si with MePIFA (b) and DPIFA (c) SAM.

The topography of bare Si, Si/MePIFA and Si/DPIFA were evaluated by the AFM images as shown Figure 4.2.a-c. There is no significant difference in morphology between AFM images of modified and unmodified Si surface. However, the measured RMS roughness with two times differences indicates the modification of Si surface with MePIFA and DPIFA SAM molecules.

Table 4.2. Roughness values of bare Si and modified Si with MePIFA and DPIFA.

	Bare Si	**Si-MePIFA**	**Si-DPIFA**
Roughness (rms)	0,132nm	0,190nm	0,266nm

The effect of the SAM molecules between ITO and TPD was characterized by recording AFM images as shown in Figure 4.3.a-c, respectively. TPD deposited on bare ITO shows discontinuous surface morphology due to incompatible structural difference between hydrophilic ITO and hydrophobic TPD. However, modified ITO with MePIFA and DPIFA SAM molecules exhibits a well-dispersed TPD film compared with bare ITO. This result might contribute to turn on voltage and electroluminance intensity improvement.

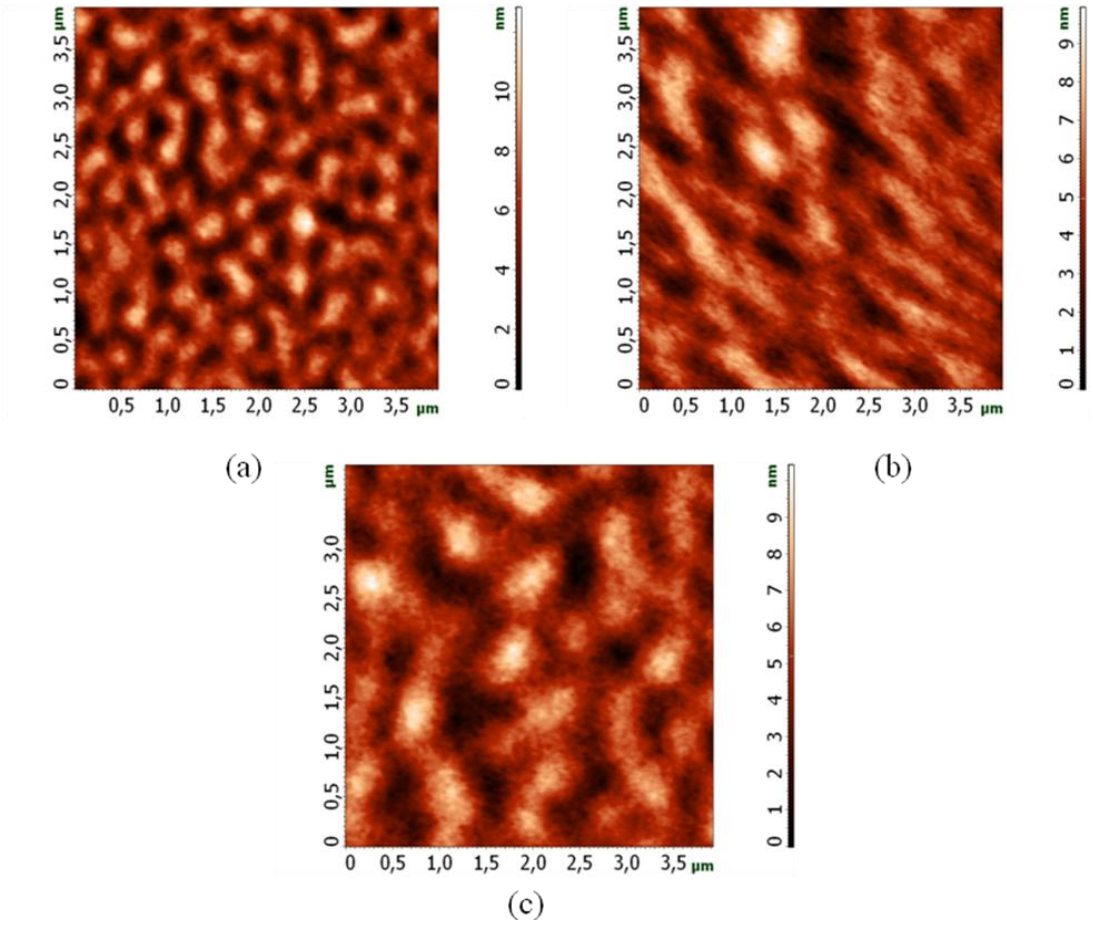

Figure 4.3. AFM images of ITO/TPD (50nm) (a), ITO/MePIFA/TPD (50nm) (b) and ITO/DPIFA/TPD (50nm) (c).

The AFM images of the NPB deposited films on bare ITO and SAM-modified ITO with MePIFA and DPIFA are shown in Figure 4.4.a-c, respectively. Bare ITO and SAM modified ITO with MePIFA shows similar NPB layer compared to DPIFA SAM. DPIFA SAM molecule exhibited a well-dispersed NPB layer.

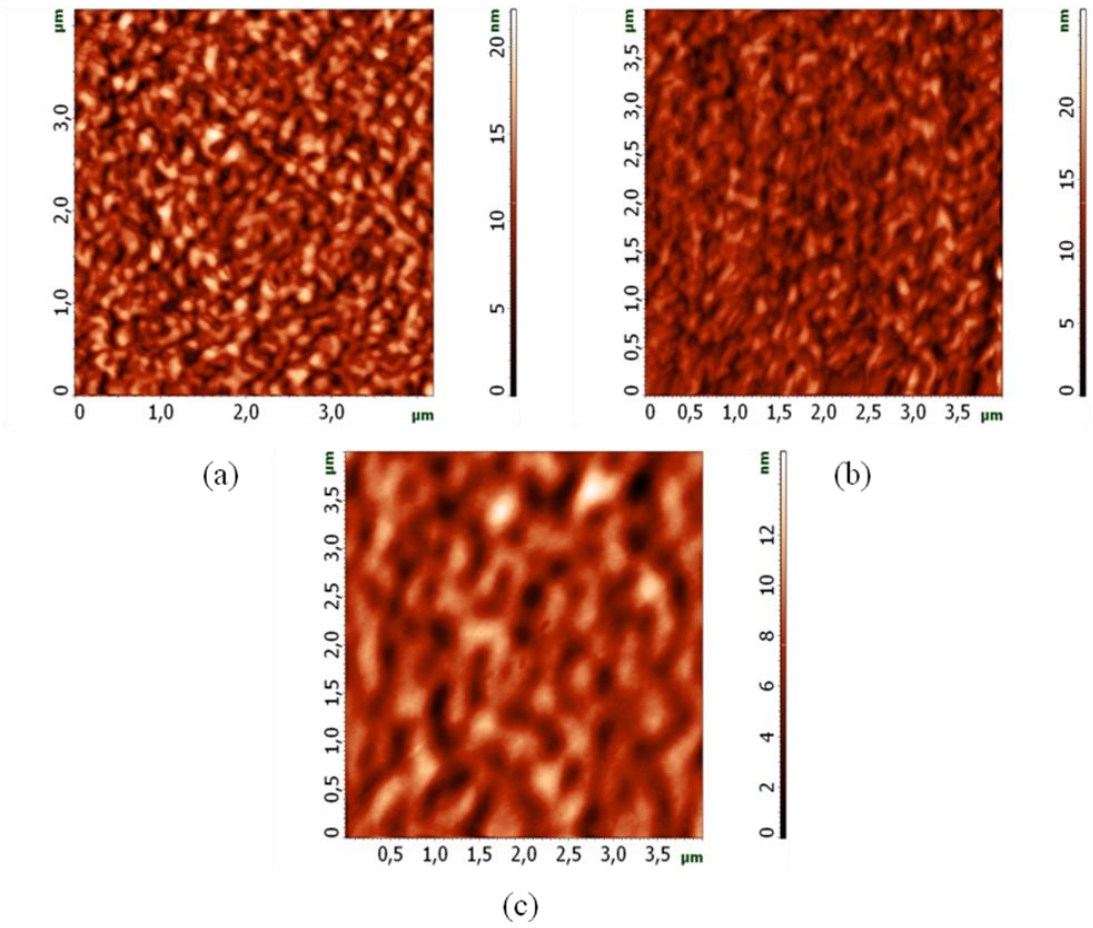

Figure 4.4. AFM images of ITO/NPB (50nm) (a), ITO/MePIFA/NPB (50nm) (b) and ITO/DPIFA/NPB (50nm) (c).

4.1.2. Spreading Resistance Microscopy Results

To investigate local conductivity of bare ITO and modified ITO with MePIFA and DPIFA SAM molecules, Spreading Resistance Microscopy were performed by applying voltage to the conductive tip (0.5V). Figure 4.2 shows SRM images of bare ITO and modified ITO with MePIFA and DPIFA, respectively. The lighter areas in the images correspond to higher conductivity while darker areas are corresponding to higher resistivity. Modified ITO with MePIFA and DPIFA SAM molecules show lower conductivity with respect to bare ITO as seen in Figure 4.5.a-c. It means that SAM molecules act as a dielectric layer between ITO and conductive AFM tip.

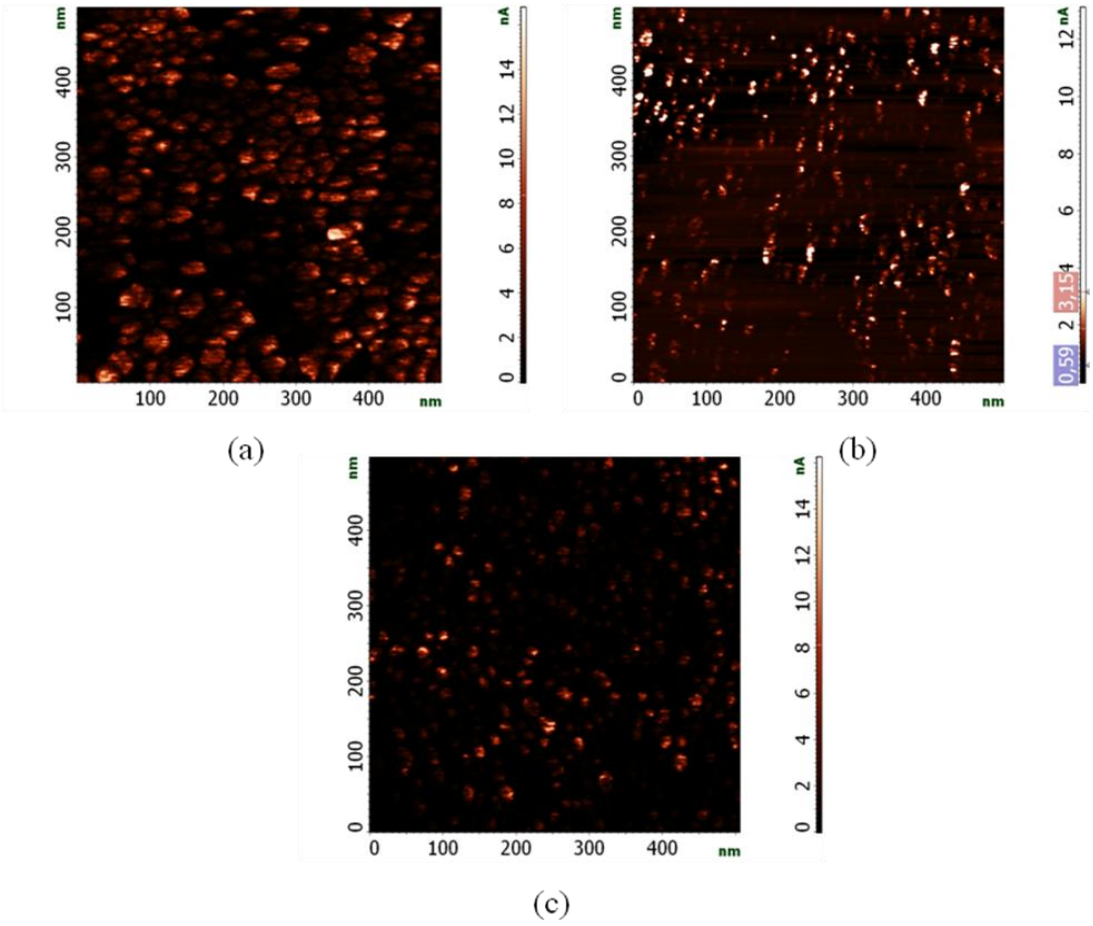

Figure 4.5. SSRM images of bare ITO (a), modified ITO with MePIFA (b) and DPIFA (c) SAM molecules.

To measure and compare the resistance of bare ITO and SAM modified ITO with MePIFA and DPIFA, the I-V curves are shown in Figure 4.6. The obtained resistance from the linear region of the I-V curves were $6{,}1x10^{6}\Omega$, $1{,}9x10^{7}\Omega$ and $1{,}8x10^{7}\Omega$ for bare ITO, ITO/MePIFA, and ITO/DIFA, respectively. Unmodified ITO had a lower resistance surface than SAM modified ITO with MePIFA and DPIFA which acted as a dielectric layer. The values of resistance are in good agreement with SRM images.

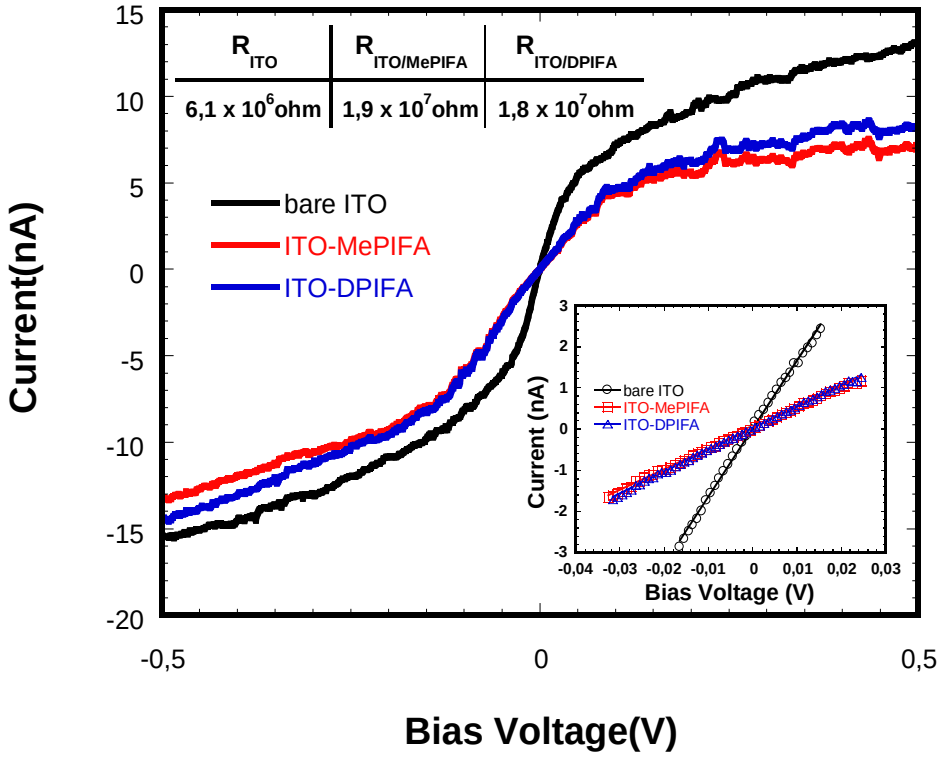

Figure 4.6. AFM I-V curves of bare ITO and SAM modified ITO with MePIFA and DPIFA.

4.1.3. Scanning Tunneling Microscopy Results

The surface morphology of bare ITO, modified ITO and unmodified were characterized with STM as shown in Figure 4.7, 4.8 and 4.9. Bare ITO has homogenous surface morphology, which is important for achievement of well-organized SAMs, with a regular granular structure as seen in Figure 4.7.b. The grain dimension is around 10-15 nm.

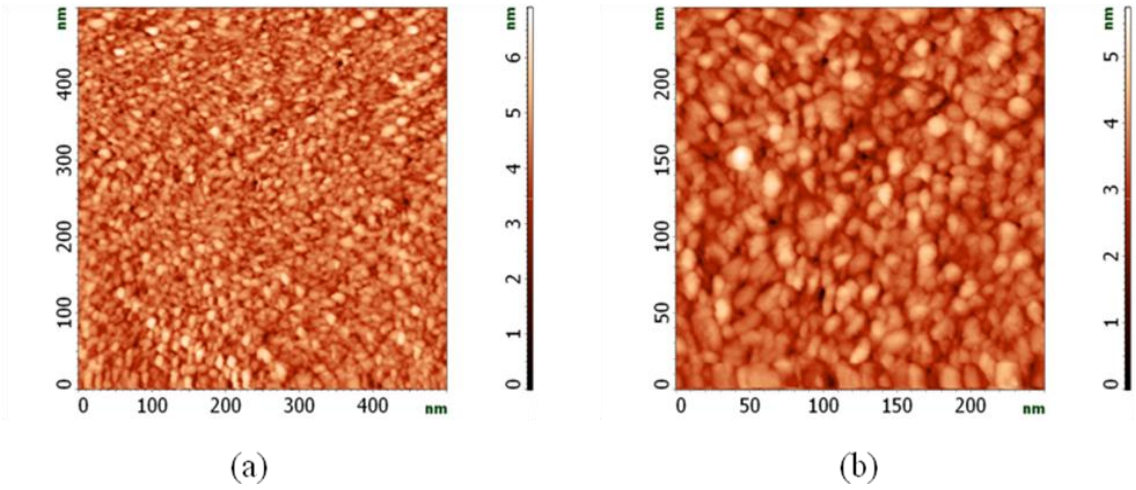

Figure 4.7. STM images of bare ITO with 500nm scan area (a) and with 250nm scan area (b).

However, modified ITO with MePIFA and DPIFA exhibit disrupted surface morphology with respect to the bare ITO.

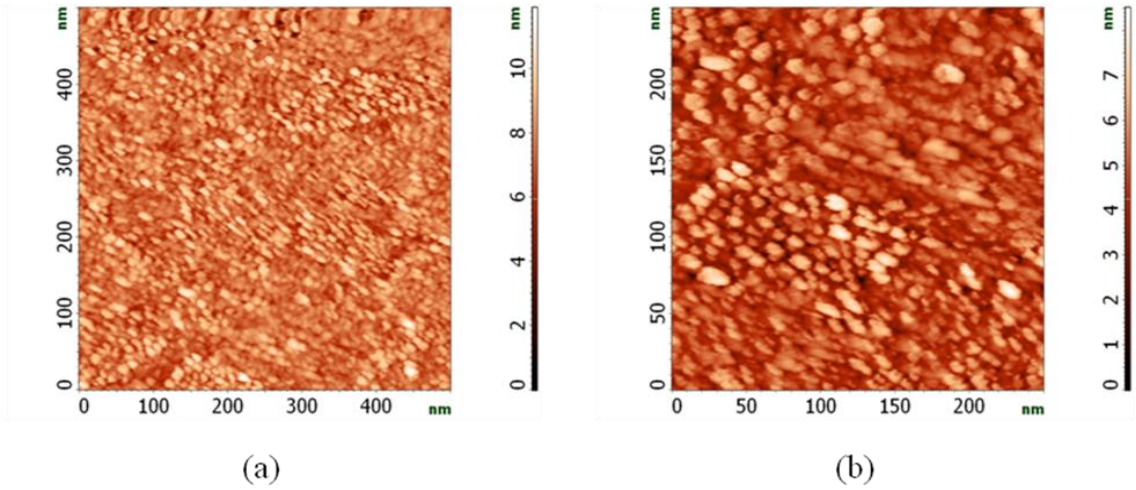

Figure 4.8. STM images of Modified ITO with MePIFA SAM molecule with 500nm scan area (a) and with 250nm scan area (b).

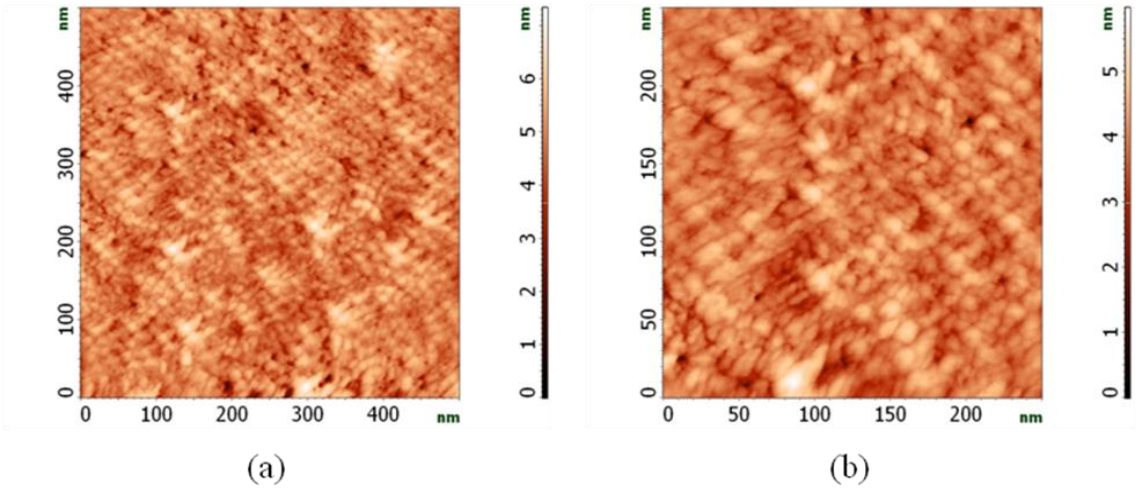

Figure 4.9. STM images of Modified ITO with DPIFA SAM molecule with 500nm scan area (a) and with 250nm scan area (b).

As a result, surface morphology changes show the modification of ITO surface with MePIFA and DPIFA molecular film.

Scanning tunneling spectroscopy (I-V) were obtained to measure and compare the resistance of bare ITO and SAM modified ITO with MePIFA and DPIFA. These result are shown in Figure 4.10. The resistance from the linear region of the I-V curves were $7.4x10^5\Omega$, $1.1x10^7\Omega$ and $9.3x10^6\Omega$ for bare ITO, ITO/MePIFA and ITO/DIFA, respectively. These resistance values are in good agreement with I-V from AFM analyses.

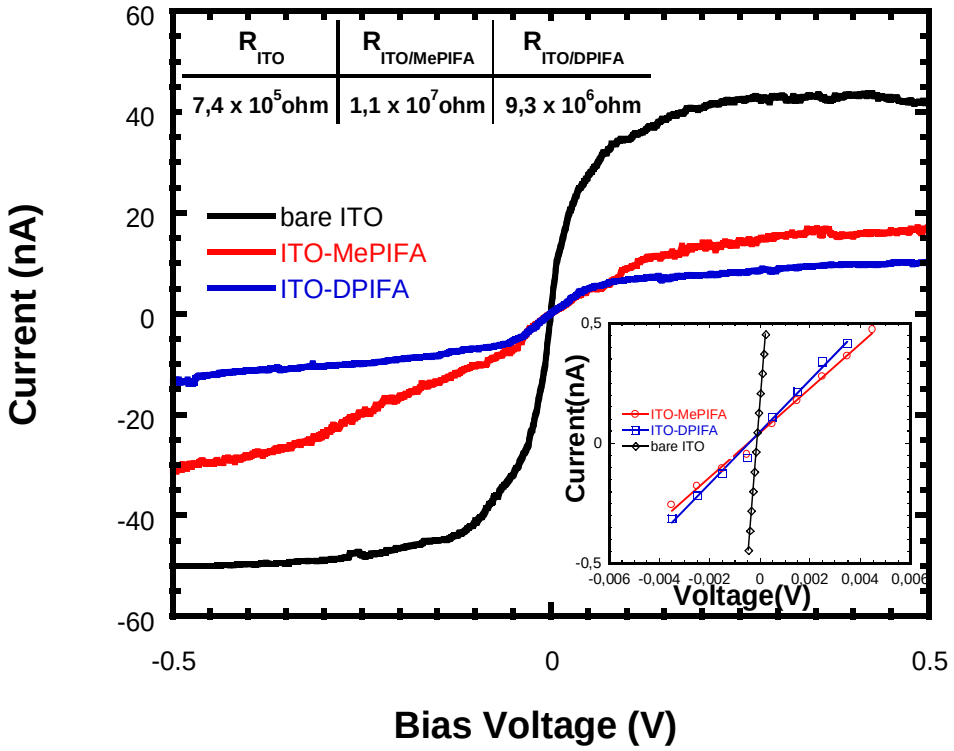

Figure 4.10. STM I-V curves of bare ITO and SAM modified ITO with MePIFA and DPIFA.

Fowler-Nordheim (FN) tunneling describes electrical transport mechanism in a SAM (Wang et al., 2003). In this study, The J-V data can be analyzed using F-N theoretical model as following (Aswal et al., 2006).

$$J = BE^2 \exp(-\frac{C}{E}) \tag{4.1}$$

where E=V/d is the electrical field across the monolayer and d is the thickness of SAM,

$$B = \frac{e^3}{16\pi^2 \hbar m^* \phi} \quad \text{and} \quad C = \frac{4\sqrt{2m^*}}{3e\hbar}\phi^{3/2} \tag{4.2}$$

where e is the electron charge, m^* is the effective mass of electron, ħ is the Planck's constant and ϕ is the average barrier height.

In the F-N region, as shown in figure 4.11, the data is plotted as ln (J/E^2) - 1/E known as F-N plot should have a linear behavior. From the slopes (C) and using d=1 nm and $m^*=0.16m_e$ (Aswal et al., 2005). The calculated barrier heights of ϕ_{ITO}, $\phi_{ITO/MePIFA}$, and $\phi_{ITO/DPIFA}$ have been obtained as 0.209eV, 0.111 eV and 0.135 eV, respectively. The results show that the average barrier height on ITO surface was decreased after modification with SAM molecules.

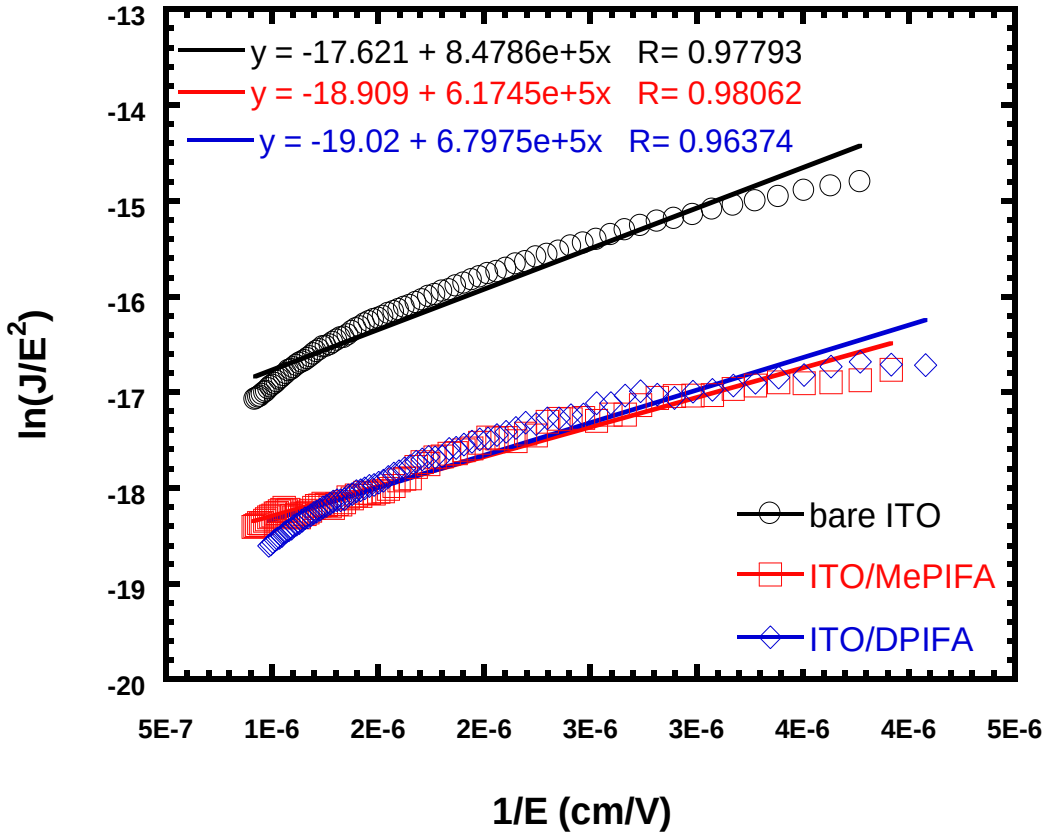

Figure 4.11. The plot of ln (J/E^2) as a function of 1/E for bare and modified ITO with MePIFA and DPIFA.

4.1.4. Kelvin Probe Force Microscopy Results

In order to find surface potential of modified and unmodified ITO surfaces Kelvin Probe Force Microscopy was performed for constant and variable applied voltages between sample and tip with two pass techniques. In the first pass, surface

topography images were obtained in semicontact mode as shown in Figure 4.12.a, 4.13.a and 4.14.a for bare ITO and modified ITO with MePIFA and DPIFA SAM. In the second pass, the probe was retracted above the surface at the height dZ and surface potential topographies were obtained as shown in Figure 4.12.b, 4.13.b and 4.14.b.

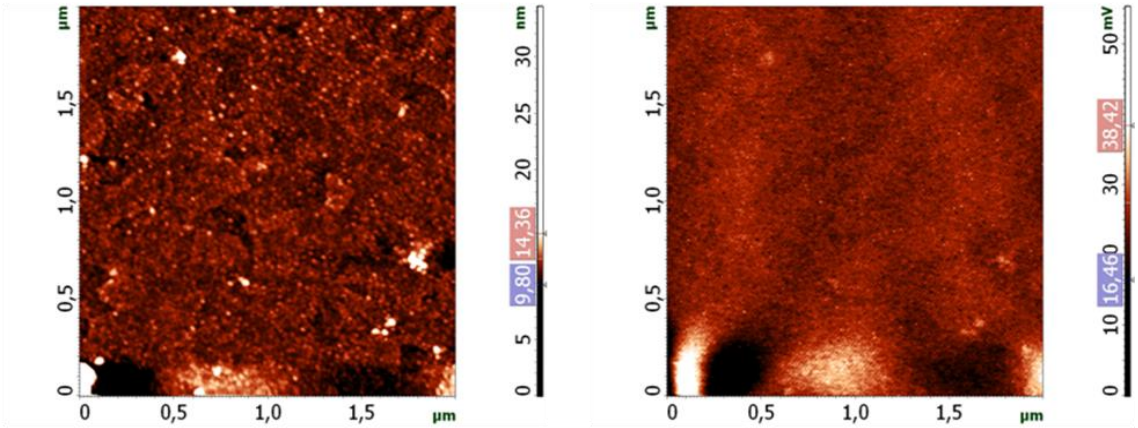

(a) (b)

Figure 4.12. AFM topography (a) and Surface Potential (b) measured on bare ITO with KPFM technique.

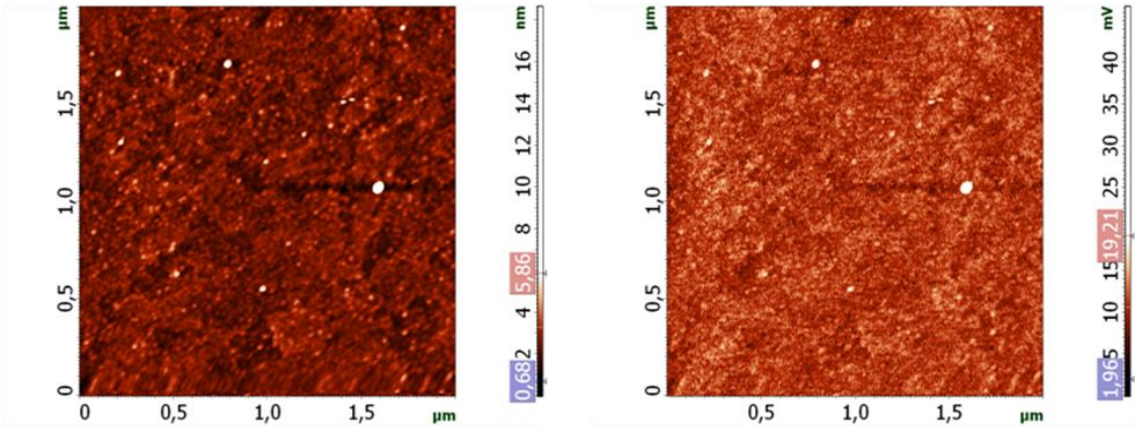

(a) (b)

Figure 4.13. AFM topography (a) and Surface Potential (b) measured on ITO-MePIFA with KPFM technique.

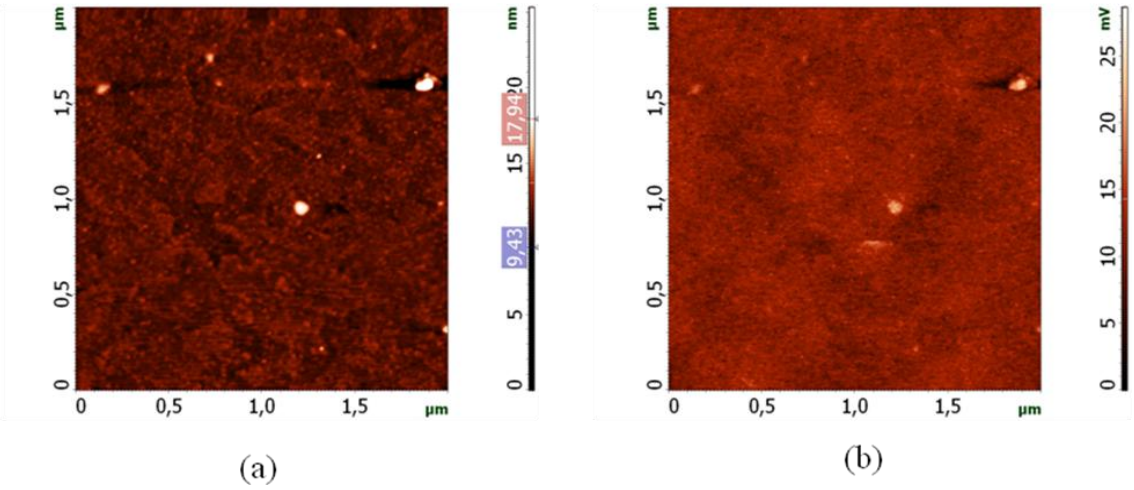

Figure 4.14. AFM topography (a) and Surface Potential (b) measured on ITO-DPIFA with KPFM technique.

Figure 4.15 shows Kelvin Probe Force Microscopy to obtain surface potential on bare ITO and modified ITO with MePIFA and DPIFA SAM molecules.

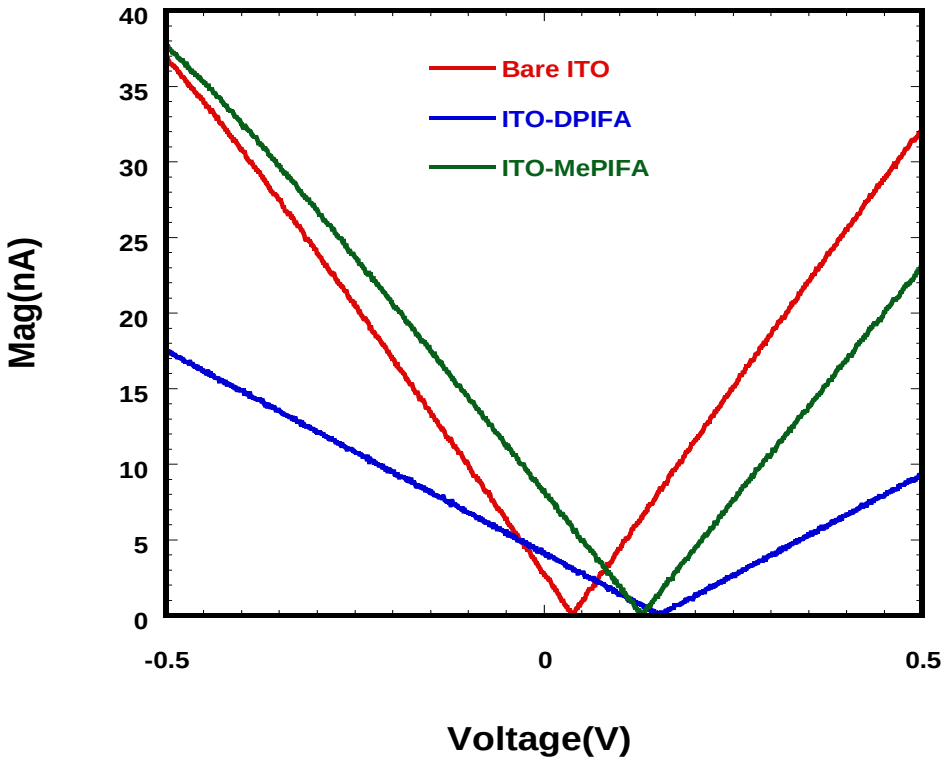

Figure 4.15. Cantilever oscillating amplitude at ω frequency versus applied voltage.

The surface potentials were measured as 36mV, 127 mV and 151 mV for the bare ITO, modified ITO with MePIFA SAM and modified ITO with DPIFA SAM. Table 4.3 summarizes the surface potentials for the bare ITO and modified ITO with MePIFA and DPIFA obtained using KPFM.

Table 4.3. Surface Potential values of bare ITO and modified ITO with MePIFA and DPIFA.

	Bare ITO	**ITO-MePIFA**	**ITO-DPIFA**
Surface Potential	0,036V	0,127V	0,151V

The KPFM results show the surface potential of modified ITO with MePIFA and DPIFA were increased more than 100 mV with respect to the bare ITO surface. It means that the work functions of MePIFA and DPIFA modified ITO surface were enhanced toward HOMO level of TPD and NPB to increase hole injection.

Figure 4.16.a, 4.17.a and 4.18.a show AFM height images of the TPD films deposited on the bare ITO and SAM modified ITO with MePIFA and DPIFA. Figure 4.16.b, 4.17.b, and 4.18.b show surface potential images of the TPD films deposited on bare ITO and modified ITO with MePIFA and DPIFA.

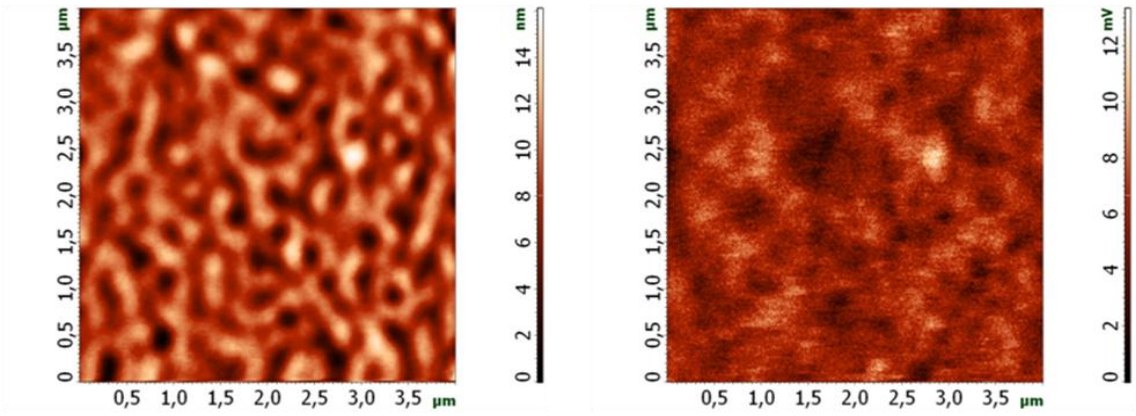

(a) (b)

Figure 4.16. AFM topography (a) and Surface Potential (b) measured on ITO/TPD with KPFM technique.

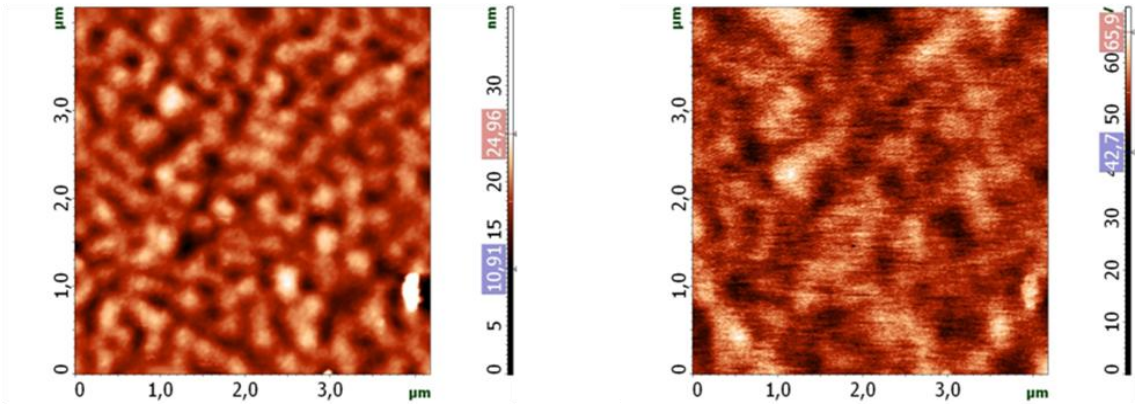

(a) (b)

Figure 4.17. AFM topography (a) and Surface Potential (b) measured on ITO/MePIFA/ TPD with KPFM technique.

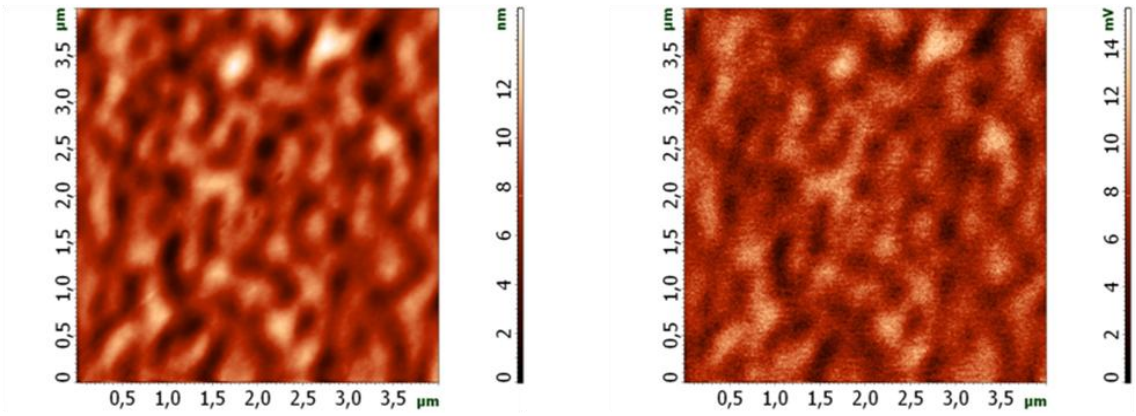

(a) (b)

Figure 4.18. AFM topography (a) and Surface Potential (b) measured on ITO/DPIFA/ TPD with KPFM technique.

Figure 4.19 shows Kelvin Probe Force Microscopy to obtain surface potential TPD films deposited on bare ITO and modified ITO with MePIFA and DPIFA SAM molecules.

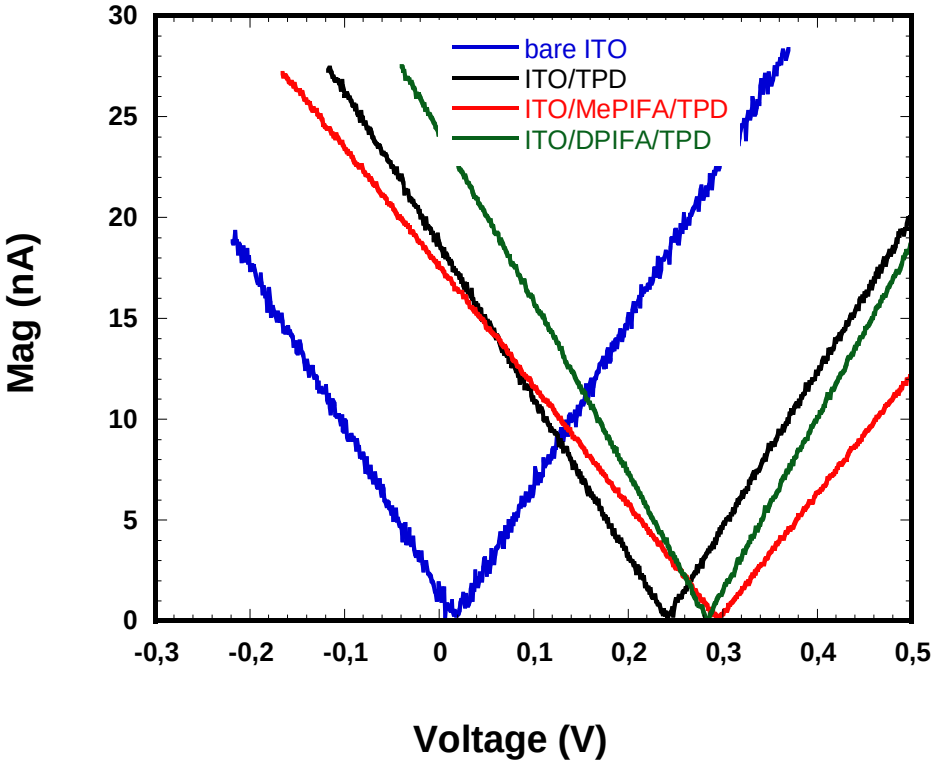

Figure 4.19. Cantilever oscillating amplitude at ω frequency versus voltage.

The surface potential values obtained from the (Mag-V) curves were found as 0.036V, 0.241V, 0.300V and 0.282V for bare ITO, ITO/TPD, ITO/MePIFA/TPD and ITO/DPIFA/TPD respectively (Table 4.4).

Table 4.4. Surface Potential values of bare ITO, ITO/TPD, ITO/MePIFA/TPD and ITO/DPIFA/TPD.

	Bare ITO	**ITO/TPD**	**ITO/MePIFA/TPD**	**ITO/DPIFA/TPD**
Surface Potential	0,036V	0,241V	0,300V	0,282V

Figure 4.20.a, 4.21.a and 4.22.a show AFM height images of the NPB films deposited on the bare ITO and SAM modified ITO with MePIFA and DPIFA. Figure

4.20.b, 4.21.b, and 4.22.b show surface potential images of the NPB films deposited on bare ITO and SAM modified ITO with MePIFA and DPIFA.

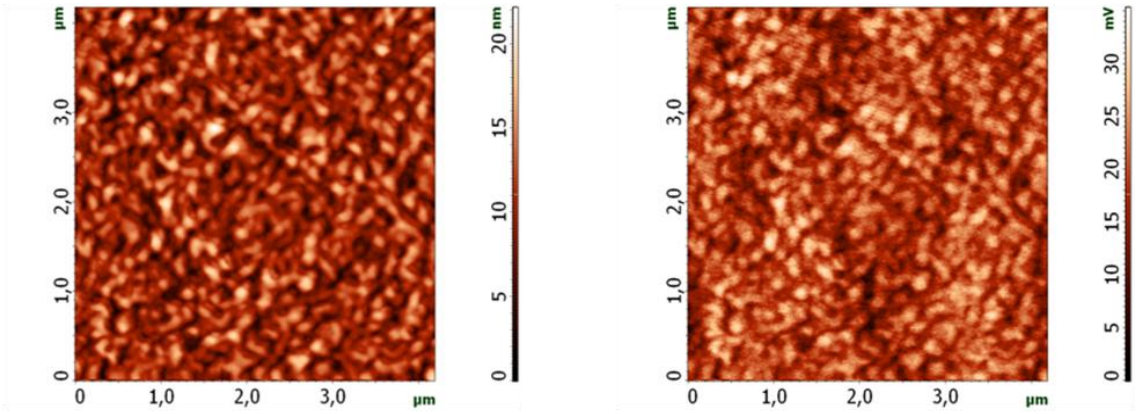

(a) (b)

Figure 4.20. AFM topography (a) and Surface Potential (b) measured on ITO/NPB with KPFM technique.

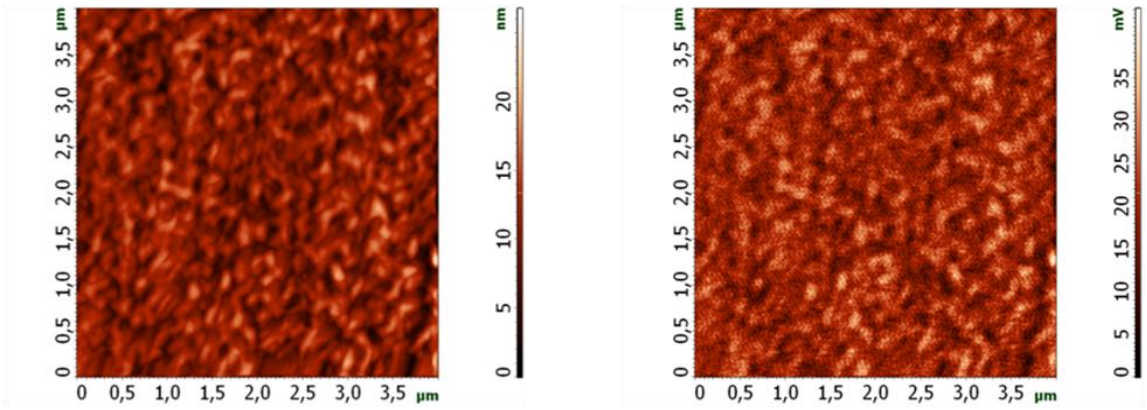

(a) (b)

Figure 4.21. AFM topography (a) and Surface Potential (b) measured on ITO/MePIFA/ NPB with KPFM technique.

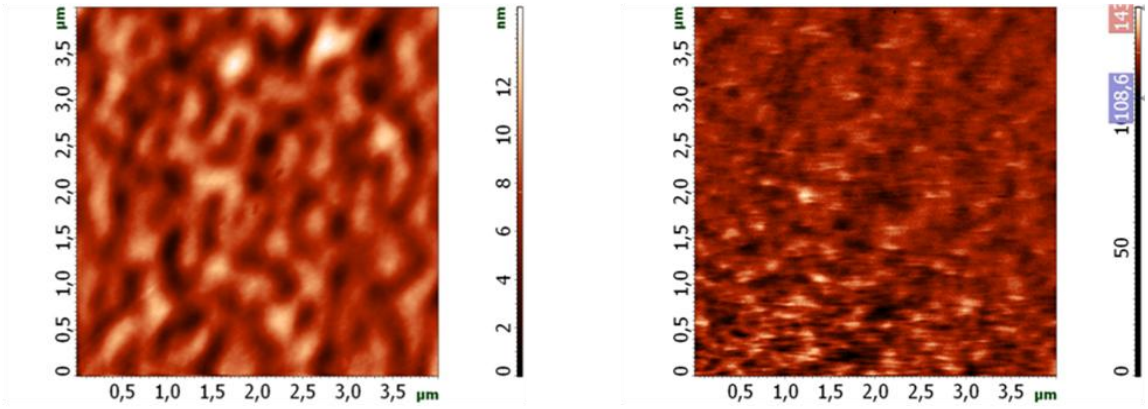

Figure 4.22. AFM topography (a) and Surface Potential (b) measured on ITO/DPIFA/ NPB with KPFM technique.

Figure 4.23 shows surface potential of NPB films deposited on bare ITO and modified ITO with MePIFA and DPIFA SAM molecules.

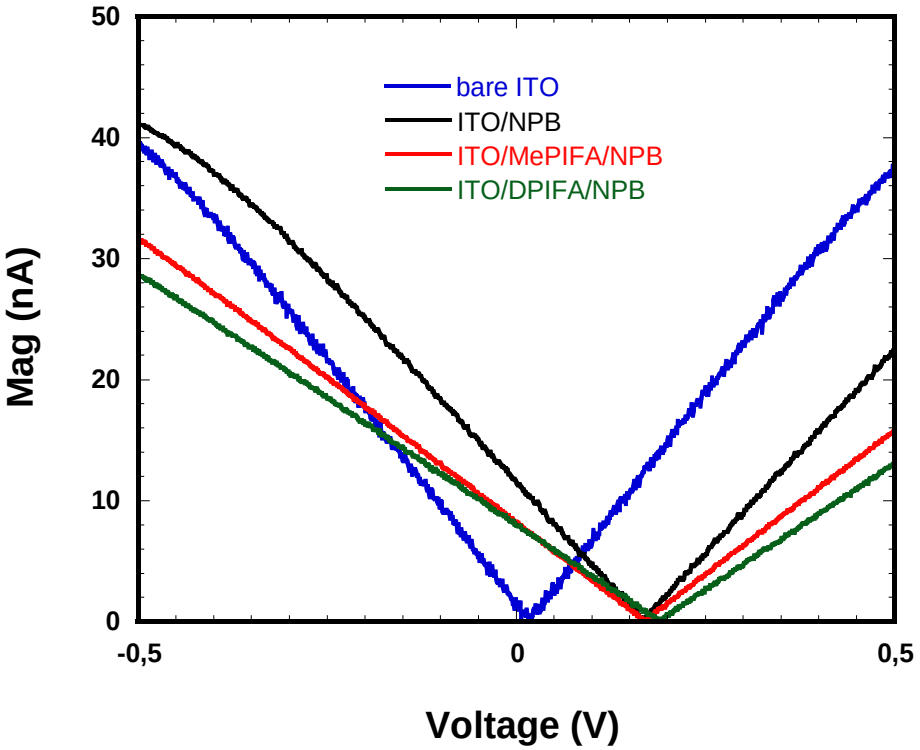

Figure 4.23. Cantilever oscillating amplitude at ω frequency versus applied voltage.

The surface potential values obtained from the (Mag-V) curves were 0.036V, 0.172V, 0.174V and 0.192V for bare ITO, ITO/NPB, ITO/MePIFA/NPB and ITO/DPIFA/NPB respectively (Table 4.5).

Table 4.5. Surface Potential values of bare ITO, ITO/NPB, ITO/MePIFA/NPB and ITO/DPIFA/NPB

	Bare ITO	**ITO/NPB**	**ITO/MePIFA/NPB**	**ITO/DPIFA/NPB**
Surface Potential	0,036V	0,172V	0,174V	0,192V

4.2. Space Charge Analysis Results

The schematic structure of hole only devices is shown in the inset of Figure 4.24. The hole only devices with a structure of ITO/MePIFA or DPIFA SAM/TPD (50 nm)/Al (120 nm) were fabricated. Figure 4.23 shows current density versus voltage characteristic (J-V) of modified and unmodified ITO devices. It can be seen that current density of unmodified ITO were increased with respect to the modified ITO. Moreover, J-V characteristics indicate two distinct regions at low and high biases relatively. As the voltage increases J-V characteristics turn to space charge limited current (SCLC) (Khan et al., 2008) and SCLC can be expressed as

$$J_{SCLC} = \frac{9}{8} \varepsilon_0 \mu \frac{V^2}{L^3} \tag{4.3}$$

where E is the electric field, ε and ε_0 are the relative dielectric constant and permittivity of the free space, respectively, and L is thickness of the organic layer.

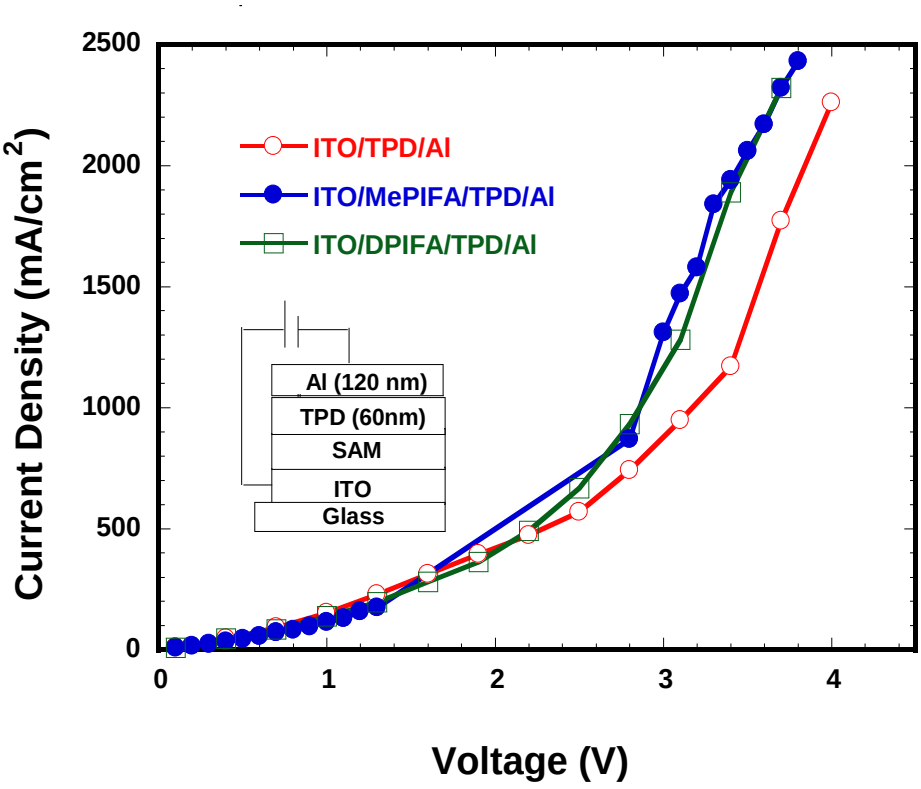

Figure 4.24. Current density versus voltage characteristic for modified and unmodified devices.

‘‘The carrier mobility is affected by energetic disorder due to the interaction of each hopping charge with randomly oriented and randomly located dipoles in the organic thin film’’(Xueyin et al., 2009). Therefore, the mobility is dependent on the electric field can be expressed by a Poole-Frenkel equation

$$\mu(E) = \mu_0 \exp(\beta\sqrt{E}) \qquad (4.4)$$

where μ_0 is the zero field mobility and β is the Poole-Frenkel factor. From a combination of Equation (4.3) and (4.4), the field dependent SCLC can be expressed by

$$J_{SCLC} = \frac{9}{8}\varepsilon\varepsilon_0\mu\frac{V^2}{L^3}\mu_0\exp(\beta\sqrt{E}) \qquad (4.5)$$

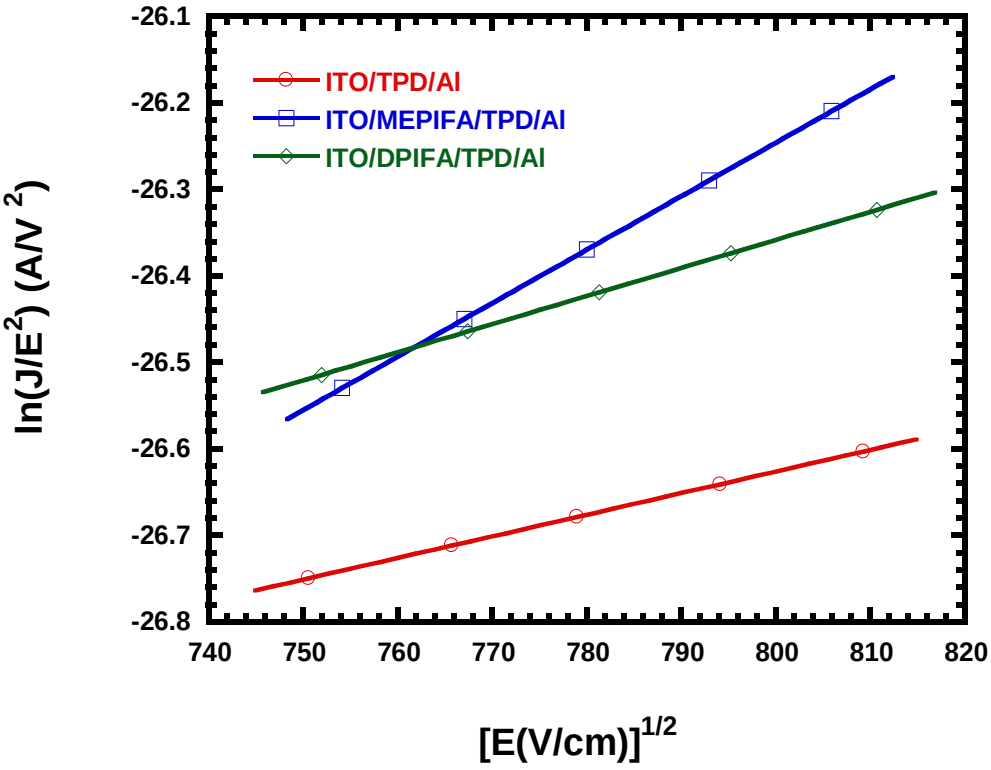

Figure 4.25. Space charge limited currents for modified and unmodified devices.

Figure 4.25 shows the logarithm of J/E^2 versus the square root mean electric field. It is clear that the $\ln(J/E^2)$ increased with increasing applied electric field. β (Pool-Frenkel) and μ_0 (zero-field mobility) can be obtained from the slope and intercept of a line fit to the linear part of J/E^2 versus $E^{1/2}$ plots. The values of μ_0 were found as 6.66 $x10^{-6}$, 4.74 $x10^{-7}$ and $4.4x10^{-6}$ $cm^2/V.s$ for bare ITO, ITO/MePIFA and ITO/DPIFA, respectively. The values of β were found as $2.3x10^{-3}$, $6.1x10^{-3}$ and $3.2x10^{-3}$ for bare ITO, ITO/MePIFA and ITO/DPIFA, respectively.

Figure 4.26 the field dependence of hole mobility for modified and unmodified devices. The mobilities for MePIFA and DPIFA modified devices were increased compared with unmodified device. For the electric field at 0.8 MV/s, the estimated hole mobility of bare and SAM modified ITO with MePIFA and DPIFA were found as 5.60 $x10^{-5}$, $1.04x10^{-4}$ and $7.27x10^{-5}$ $cm^2/V.s$, respectively. There is important enhancement in hole mobility due to modification of SAM molecules. Both MePIFA and DPIFA SAM

molecules form extra energy levels between HOMO and LUMO of TPD. That's why; these energy levels help to increase of tunneling in aromatic groups and contribute increments of hole mobility.

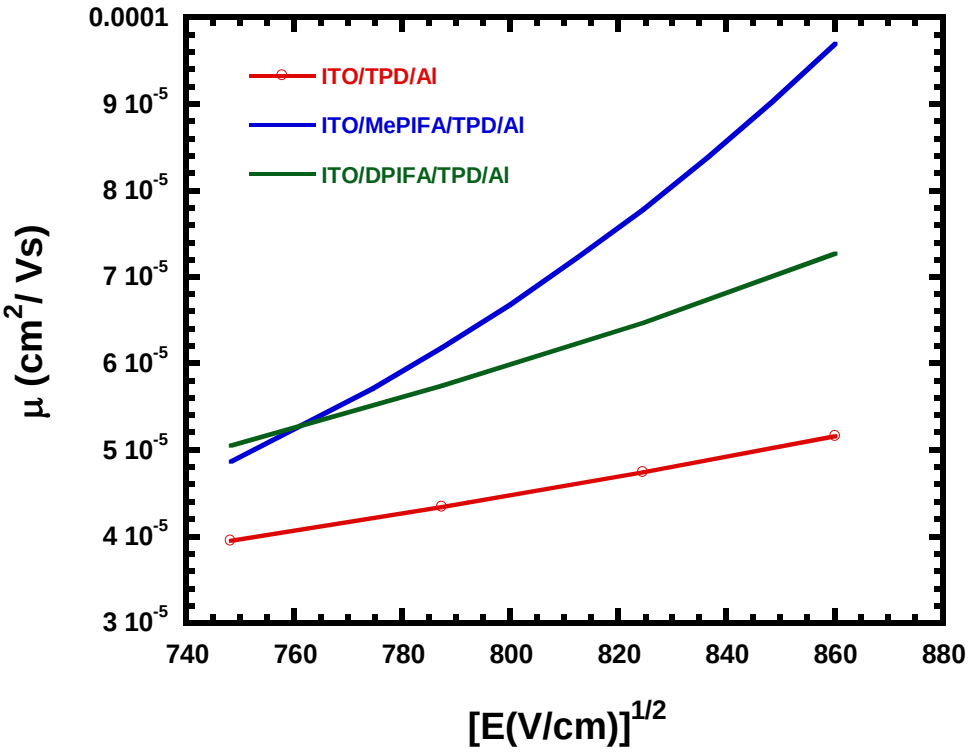

Figure 4.26. Mobility-square root of electric field for modified and unmodified devices.

The schematic structure of hole only devices is shown as an inset in Figure 4.27. We fabricated hole only devices with a structure of ITO/MePIFA or DPIFA SAM/NPB (50 nm)/Al (120 nm). Also, Figure 4.27 shows current density versus voltage characteristic (J-V) of modified and unmodified ITO devices. It can be seen that current density of unmodified ITO were increased with respect to the modified ITO.

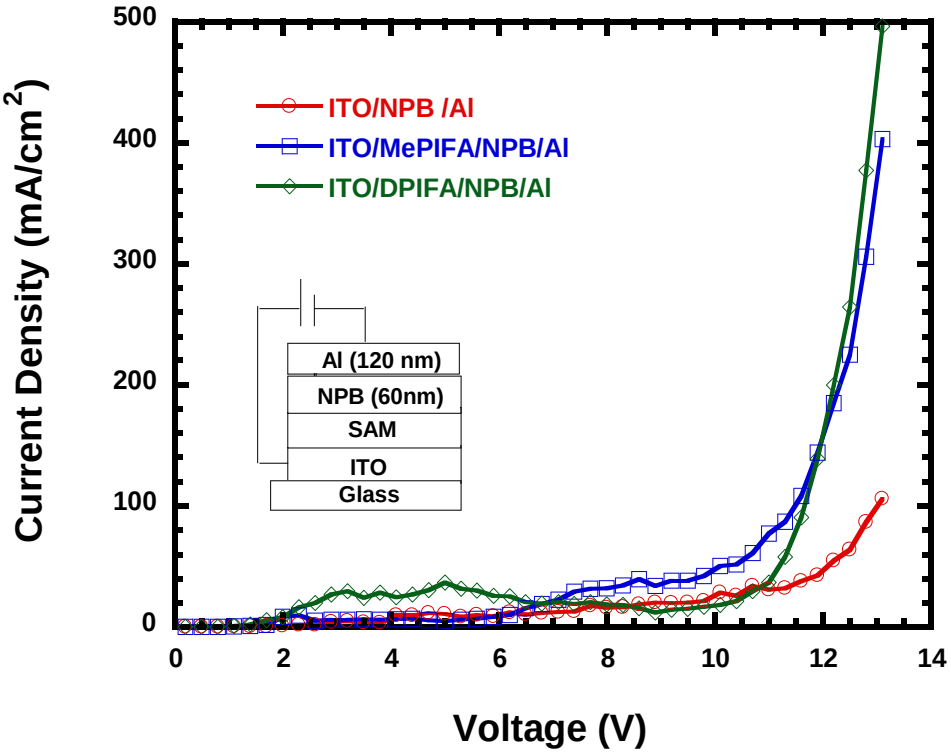

Figure 4.27. Current density versus voltage characteristic for modified and unmodified devices.

Figure 4.28 shows the logarithm of J/E^2 versus the square root mean electric field. The $\ln(J/E^2)$ increased with increasing applied electric field. β (Pool-Frenkel) and μ_0 (zero-field mobility) can be obtained from the slope and intercept of a line fit to the linear part of J/E^2 versus $E^{1/2}$ plots. The values of μ_0 were found as 6.66×10^{-6}, 4.74×10^{-7} and 4.4×10^{-6} $cm^2/V.s$ for bare ITO, ITO/MePIFA and ITO/DPIFA, respectively. The values of β were found as 6.1×10^{-3}, 3.2×10^{-3} and 2.8×10^{-3} for bare ITO, ITO/MePIFA and ITO/DPIFA, respectively.

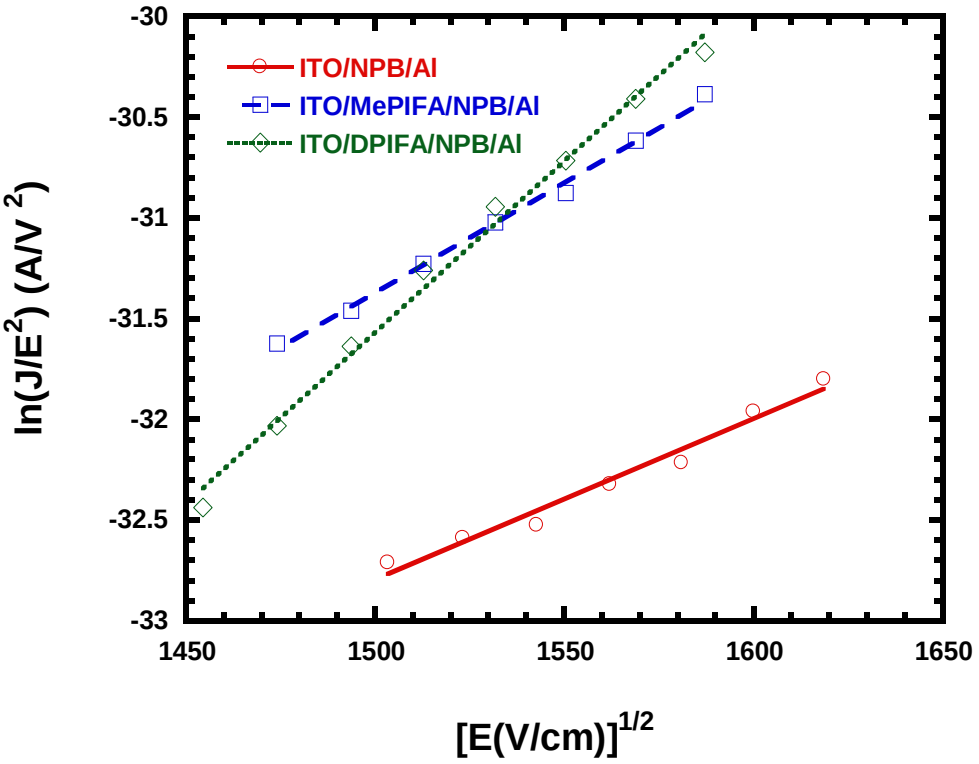

Figure 4.28. Space charge limited currents for modified and unmodified devices.

Figure 4.29 the field dependence of hole mobility for modified and unmodified devices. It can be seen that the mobilities for MePIFA and DPIFA modified devices were increased compared with unmodified device. For the electric field at 0.8 MV/s, the estimated hole mobility of bare and SAM modified ITO with MePIFA and DPIFA were found as 2.47 $x10^{-7}$, $1.07x10^{-6}$ and $1.44x10^{-6}$ $cm^2/V.s$, respectively. MePIFA and DPIFA SAM molecules contribute to increments of the hole mobility due to the lower resistance interface between ITO and SAM molecules.

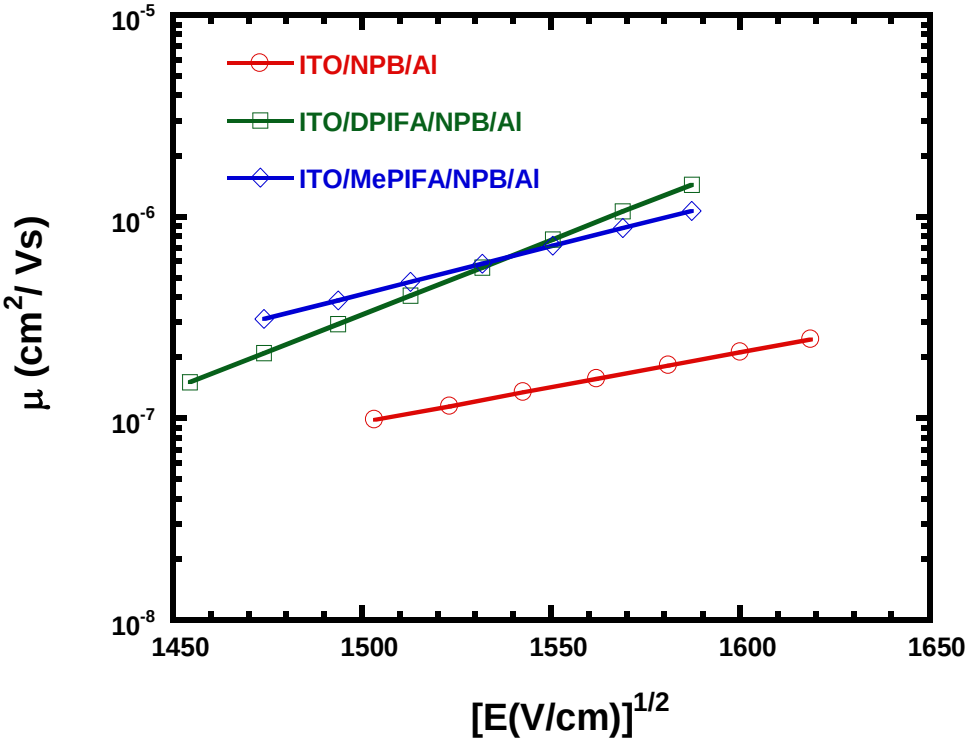

Figure 4.29. Mobility-square root of electric field for modified and unmodified devices.

4.3. Cylic Voltammetry Results

Electrochemistry of MePIFA and DPIFA SAM coated on ITO were investigated by Cylic Voltammetry. MePIFA molecule showed one reversible oxidation peak at 1,202 V on ITO surface. This slight shift to more negative potential can be attributed to carbonyl group that anchored to ITO surface. It must noticed that HOMO level of MePIFA was calculated from the onset of the oxidation potential. The oxidation onset potential was determinate from the intersection of two tangents drawn at the rising oxidation current and background current in the cyclic voltammogram. The onset of oxidation was calculated to be 1.202 V on ITO surface. The HOMO level of MePIFA was calculated as -5.42 eV on ITO surface.

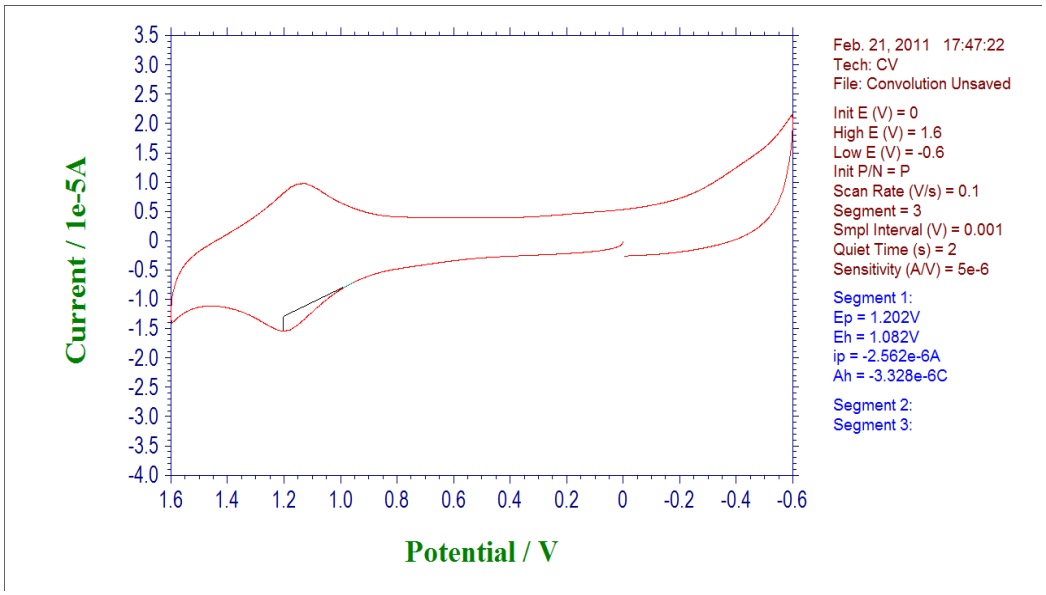

Figure 4.30. Cylic Voltammogram of the MePIFA coated on ITO surface.

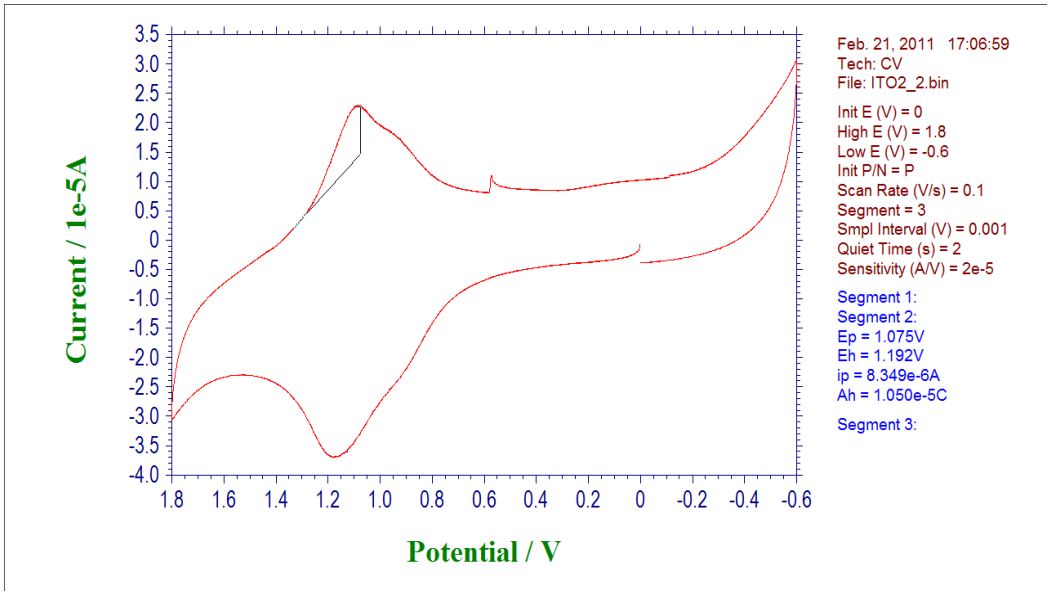

Figure 4.31. Cylic Voltammogram of the DPIFA coated on ITO surface.

DPIFA molecule showed one reversible oxidation peak at 1,075 V on ITO surface. This slight shift to more negative potential can be attributed to carbonyl group that anchored to ITO surface. It must noticed that HOMO level of DPIFA was calculated from the onset of the oxidation potential. The oxidation onset potential was determinate from the intersection of two tangents drawn at the rising oxidation current

and background current in the cyclic voltammogram. The onset of oxidation was calculated to be 1.075 V on ITO surface. The HOMO level of DPIFA was calculated as -5.21 eV on ITO surface.

4.4. Electrical Characterization Results for OLEDs devices

The current-voltage (I-V) characteristic of the first set of OLED device can be seen from Figure 4.32. The turn on voltages of OLED devices made with MePIFA and DPIFA modified ITO and bare ITO was measured as 7V, 11V and 16V respectively. Turn on voltages for MePIFA and DPIFA modified devices were improved compared with unmodified device. Since MePIFA and DPIFA SAM molecules have similar structure to on TPD. This singularity of molecular structure helps to increase of charge transfer in aromatic groups.

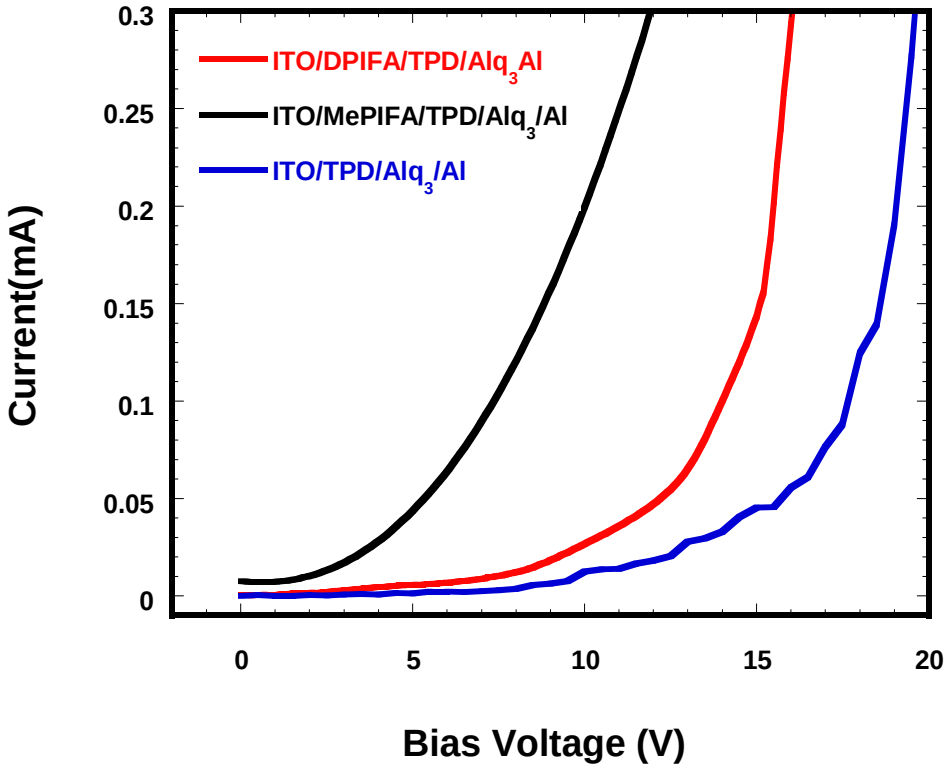

Figure 4.32. Current versus voltage characteristic for OLED devices.

However the effect of MePIFA SAM on the turn on voltage is better than DPIFA SAM due to methyl groups in the structure which leads to matching with TPD structure at the interface.

Figure 4.33 shows the electroluminance (EL) spectrum of modified and unmodified OLEDs devices. EL spectrum of OLED devices made with MePIFA and DPIFA modified ITO were improved compared with unmodified device. It means that more emission can be obtained in MePIFA and DPIFA modified OLED devices with respect to the bare ITO. Moreover, as shown from Figure 4.30, the peaks were observed around 525 nm correspond to green light emission originating from Alq_3 for the three OLED devices.

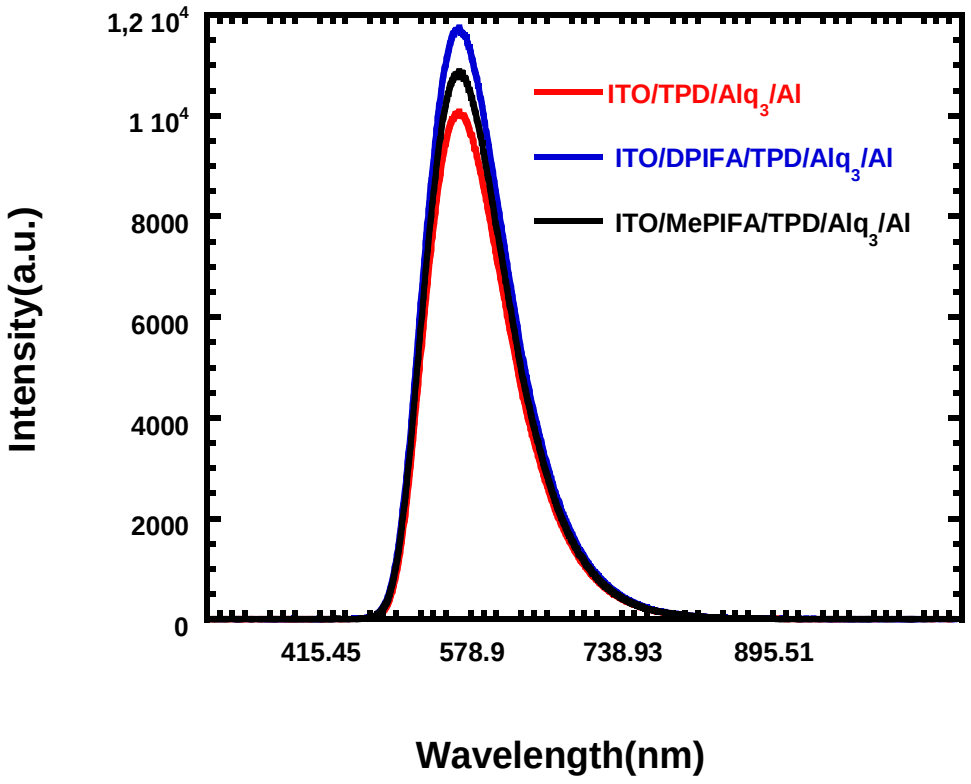

Figure 4.33. EL spectrum of modified ITO with MePIFA and DPIFA SAMs and bare ITO devices.

The current-voltage (I-V) characteristic for the second set of OLEDs device without (bare curve) and with SAM surface modification by MePIFA and DPIFA are given Figure 4.34. The turn on voltages of OLED devices made with MePIFA and DPIFA modified ITO and bare ITO was measured as 4V, 11V and 16V respectively. Both MePIFA and DPIFA have double carboxylic acid groups which formed strong chemical bond on ITO surface. Hence MePIFA and DPIFA SAM molecules have enhanced hole injection compared to bare ITO.

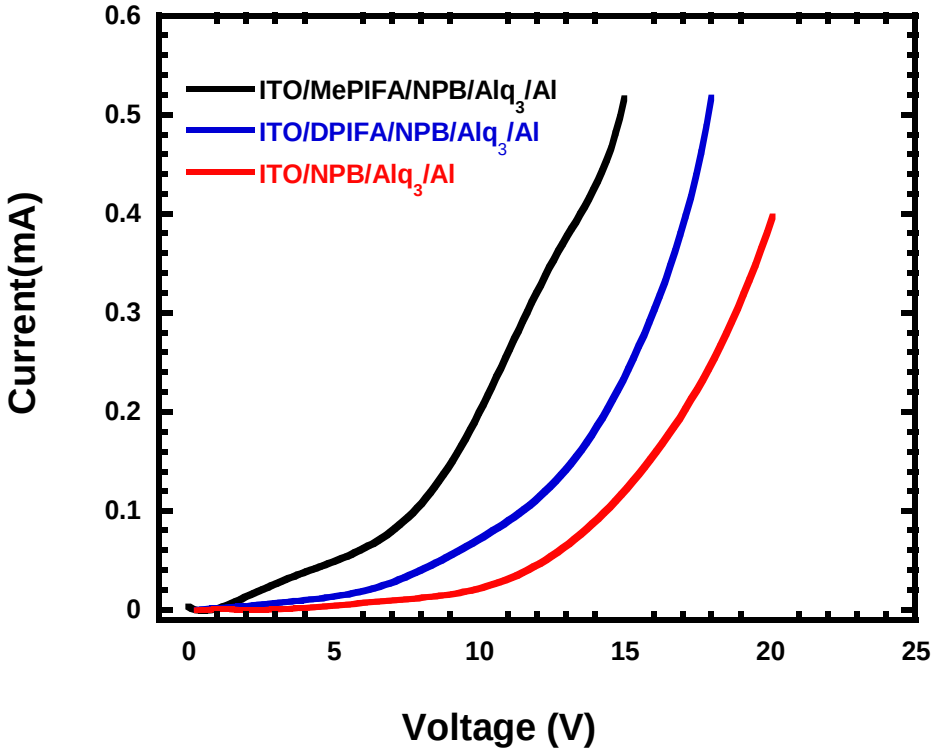

Figure 4.34. Current versus voltage characteristic for OLED devices.

The electroluminance (EL) spectrum of modified and unmodified OLEDs devices can be seen from the Figure 4.35. The emission intensity for the SAM modified OLED devices increased compare to bare ITO. This result indicates that electron-hole pairs for SAM modified OLED devices were increased in the emitting zone, resulting higher electroluminance intensity compared to bare device. Furthermore, the emission peaks were observed around 525 nm correspond to green light for the three OLED devices.

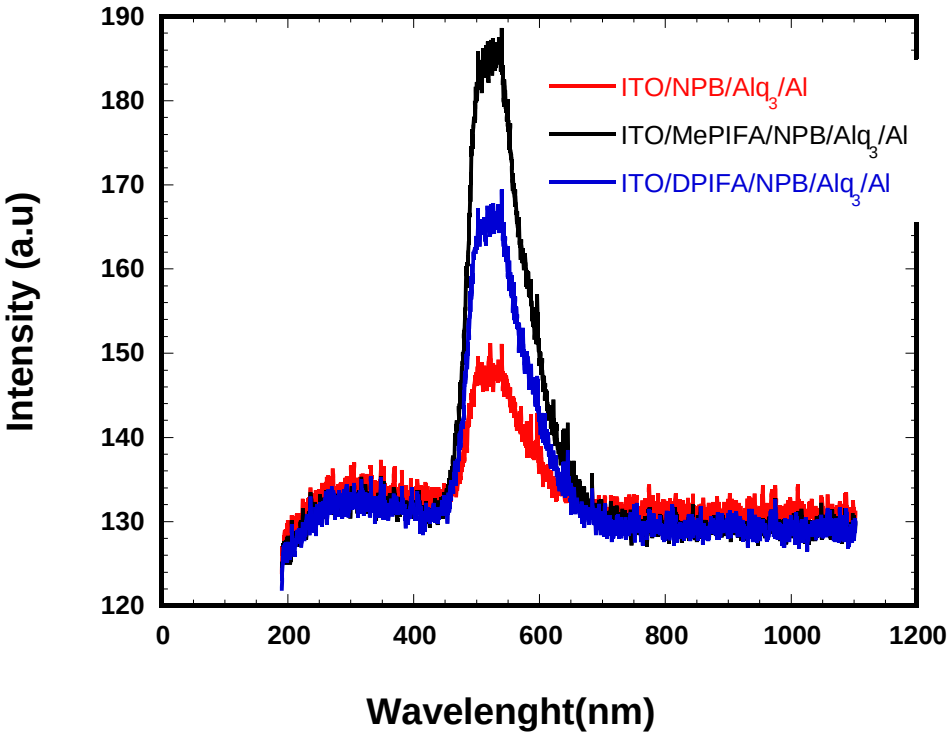

Figure 4.35. EL spectrum of modified ITO with MePIFA and DPIFA SAMs and bare ITO devices.

CHAPTER 5

CONCLUSION

This thesis focused on modification and characterization of ITO substrates with carboxylic acid based self-assembled monolayers to improve OLED device performance, such as turn-on voltage and optical efficiency. The self-assembled monolayer is one of the most promising techniques to modify anode surface. SAM is used to establish a compatible interface between hydrophilic ITO surface and hydrophobic hole transport layer (HTL). SAM also prevents from humidity and hinders passing opposed charges.

In Chapter 1, OLED literature with modification techniques has been briefly given.

Chapter 2 begins with the introduction of organic semiconductors. The devices structure of OLEDs was given in this chapter and then the principle of OLEDs operation was explained with charge injection, charge transport and charge recombination models. And then OLEDs efficiency was explained. Moreover, anode and cathode materials, hole transport materials, electron transport and emissive materials were introduced. In addition, SAM technique was given. Finally, the basic principle of Atomic Force Microscopy, Scanning Tunneling Microscopy, Kelvin Probe force Microscopy and Cylic Voltammogram were explained.

Chapter 3 consists of two subtitles; sample preparation, characterization of modified ITO and unmodified ITO. In the sample preparation part, the synthesis and preparation of SAM molecules were given and then etching and cleaning procedure of ITO substrates were explained. Afterwards, modification of ITO substrates with SAM molecules was given. Finally, possible OLED device configurations were introduced. In characterization part, the surface and electrical characterization of Atomic Force Microscopy, Scanning Tunneling Microscopy and Kelvin Probe force Microscopy were given.

In chapter 4, the experimental results were given in the details. The surface characterizations results for thin films obtained with AFM and STM were presented. The results showed the bare ITO has a granular surface morphology with the roughness

of 0.468nm. SAM modified ITO with MePIFA and DPIFA exhibit island structure morphology with the roughness of 0.567nm (for ITO-MePIFA) and 0.490nm (for ITO-DPIFA). Moreover, Si wafers were used for the monolayer characterization to compare with ITO due to the similar surface density of reactive sides. The result showed a little difference between RMS roughnesses revealed modification of Si surface with MePIFA and DPIFA SAM molecules. The effect of the SAM molecules on TPD and NPB films were also characterized. Compatible interface between ITO and TPD or NPB were observed as a result of SAM modification using MePIFA and DPIFA molecules.

I-V measurements, Scanning Spreading Resistance Microscopy (SSRM) and STM were performed. For SSRM, I-V curves were obtained by using Pt coated conductive AFM tip. The obtained resistance from the linear region of the I-V curves were $6{,}1x10^6$ Ω, $1{,}9x10^7$Ω and $1{,}8x10^7$Ω for bare ITO, ITO/MePIFA, and ITO/DIFA, respectively. For STM, I-V curves were measured by applying voltage between -0.5V to 0.5V. The obtained resistance from the linear region of the I-V curves were $7.4x10^5$ Ω, $1.1x10^7$Ω and $9.3x10^6$Ω for bare ITO, ITO/MePIFA, and ITO/DIFA, respectively. These results showed the resistance of bare ITO is smaller than SAM modified ITO/DPIFA and ITO/MePIFA surfaces.

The effect of carboxylic acid based SAMs on OLED charge transport has been analyzed using fowler-nordheim tunneling mechanism. The data is plotted as ln (J/E^2)-(1/E) known as F-N plot. The calculated barrier heights of ϕ_{ITO}, $\phi_{ITO/MePIFA}$, and $\phi_{ITO/DPIFA}$ have been obtained as 0.209eV, 0.111 eV and 0.135 eV, respectively. The results show that the average barrier height on ITO surface was decreased after modification with SAM molecules.

In order to measure the change in the surface potential after the modification of ITO surface with MePIFA and DPIFA SAM molecules, Kelvin Probe Force Microscopy were performed with TiN coated conductive AFM tip for constant and variable applied voltages between tip and sample. The surface potential values obtained from the (Mag-V) curves were found as 0.036V, 0.127V and 0.151V for bare ITO and SAM modified ITO with MePIFA and DPIFA respectively. Surface potential result showed modified ITO with MePIFA and DPIFA were increased around 0.1V with respect to the bare ITO surface. Moreover, the effect of the SAM molecules on TPD and NPB films were characterized via KPFM technique. For TPD films, the surface potential values obtained from the (Mag-V) curves were found as 0.036V, 0.241V,

0.300V and 0.282V for bare ITO, ITO/TPD, ITO/MePIFA/TPD and ITO/DPIFA/TPD respectively. For NPB films, the surface potential values obtained from the (Mag-V) curves were found as 0.036V, 0.172V, 0.174V and 0.192V for bare ITO, ITO/NPB, ITO/MePIFA/NPB and ITO/DPIFA/NPB respectively.

The effect of carboxylic acid based SAMs on OLED charge transport has been analyzed using space charge limited current. Hole only devices with a structure of ITO/MePIFA or DPIFA SAM/TPD (50 nm)/Al (120 nm) were fabricated. The mobilities of MePIFA and DPIFA modified diodes were increased compared with unmodified diodes. For the electric field at 0.8 MV/s, the estimated hole mobility of bare and SAM modified ITO with MePIFA and DPIFA were found as 5.60 $x10^{-5}$, $1.04x10^{-4}$ and $7.27x10^{-5}$ $cm^2/V.s$, respectively. There are important increments in hole mobility due to the modification of SAM molecules. Another hole only devices with a structure of ITO/MePIFA or DPIFA SAM and M/NPB (50 nm)/Al (120 nm) were fabricated. The mobilities of MePIFA and DPIFA modified diodes were increased compared with unmodified diodes. For the electric field at 0.8 MV/s, the estimated hole mobility of bare and SAM modified ITO with MePIFA and DPIFA were found as 2.47 $x10^{-7}$, $1.07x10^{-6}$ and $1.44x10^{-6}$ $cm^2/V.s$, respectively. MePIFA and DPIFA SAM molecules contribute to increments of the hole mobility due to the lower resistance at interface between ITO and SAM.

Electrochemistry of MePIFA and DPIFA SAM coated on ITO were investigated by Cylic Voltammetry. The onset of oxidation was calculated to be 1.202 V on ITO surface. The HOMO level of MePIFA was calculated as -5.42 eV on ITO surface. Similarly, the HOMO level of DPIFA was calculated as -5.21 eV on ITO surface. Hence, the work functions of MePIFA and DPIFA modified ITO surface were enhanced toward HOMO level of TPD and NPB to increase hole injection.

In the parts of the electrical and optical characterizations of OLED devices, two different sets of OLEDs devices were fabricated in order to the explore effects of SAM modification of ITO surface on electrical and optical characterization of devices. For the first set of OLED device configuration, the turn on voltages of OLED devices made with MePIFA and DPIFA modified ITO and bare ITO was measured as 7V, 11V and 16V respectively. Furthermore, EL spectrum of OLED devices made with MePIFA and DPIFA modified ITO were improved compared with base one device. For the second set of OLED device configuration, the turn on voltages of OLED devices with SAM

surface modification by MePIFA and DPIFA were improved compare with bare ITO device and also turn on voltages were measured 4V, 11V, 17V for modified ITO with MePIFA and DPIFA based devices and bare ITO devices, respectively. Moreover, EL spectrum of OLED devices made with MePIFA and DPIFA modified ITO were improved compared with bare ITO device.

To summarize, we investigated modification of ITO substrates with carboxylic acid based self-assembled monolayers to improve OLED device performance. Also, the effect of MePIFA and DPIFA SAM molecules on I-V characteristic of modified OLED was clearly observed. Since both MePIFA and DPIFA SAM molecules have double carboxylic acid head group providing strong chemical bonding on ITO surface. Furthermore, both MePIFA and DPIFA SAM molecules have similar structure to overlaying TPD or NPB. This singularity helps to increase charge transfer in aromatic structure. However, the effect of MePIFA SAM on the turn on voltage and EL intensity is better than DPIFA SAM due to methyl groups in the structure which leads to matching with TPD and NPB structure at the interface. Moreover, we believed that SAM molecules with double bond carboxylic acid form extra energy levels between HOMO and LUMO of TPD and NPB. That's why; these energy levels help to increase of tunneling in aromatic groups and contribute enhancement in the hole injection. Hence the device performance, and turn on voltage is improved compared to OLED devices with unmodified ITO substrates.

REFERENCES

Adamovich, V.I., S.R. Cordero, P.I. Djurovich, A. Tamayo, M.E. Thompson, B.W. D'Andrade, and S.R. Forrest. 2003. New charge-carrier blocking materials for high efficiency OLEDs. *Organic electronics*. 4:77-87.

Aswal, D., S. Lenfant, D. Guerin, J. Yakhmi, and D. Vuillaume. 2006. Self assembled monolayers on silicon for molecular electronics. *Analytica chimica acta*. 568:84-108.

Aswal, D.K., S. Lenfant, D. Guerin, J.V. Yakhmi, and D. Vuillaume. 2005. A Tunnel Current in Self Assembled Monolayers of 3 Mercaptopropyltrimethoxysilane. *Small*. 1:725-729.

Bansal, A.K., W. Holzer, A. Penzkofer, and T. Tsuboi. 2006. Absorption and emission spectroscopic characterization of platinum-octaethyl-porphyrin (PtOEP). *Chemical physics*. 330:118-129.

Batsanov, S. 2001. Van der Waals radii of elements. *Inorganic materials*. 37:871-885.

Bhandari, N.K., N. Bhandari, M. Cahay, P. Boolchand, and A. Ferendeci. 2009. U UNIVERSITY OF CINCINNATI.

Binnig, G., C.F. Quate, and C. Gerber. 1986. Atomic force microscope. *Physical review letters*. 56:930-933.

Binnig, G., and H. Rohrer. 1983. Scanning tunneling microscopy. *Surface Science*. 126:236-244.

Brütting, W. Organic Semiconductors.

Burroughes, J., D.D.C. Bradley, A. Brown, R. Marks, K. Mackay, R. Friend, P. Burns, and A. Holmes. 1990. Light-emitting diodes based on conjugated polymers. *nature*. 347:539-541.

Cui, J., Q. Huang, J.C.G. Veinot, H. Yan, Q. Wang, G.R. Hutchison, A.G. Richter, G. Evmenenko, P. Dutta, and T.J. Marks. 2002a. Anode interfacial engineering approaches to enhancing anode/hole transport layer interfacial stability and charge injection efficiency in organic light-emitting diodes. *Langmuir*. 18:9958-9970.

Cui, J., Q. Huang, J.G.C. Veinot, H. Yan, and T.J. Marks. 2002b. Interfacial Microstructure Function in Organic Light Emitting Diodes: Assembled Tetraaryldiamine and Copper Phthalocyanine Interlayers. *Advanced Materials*. 14:565-569.

Donkor, E., A.K. Viswanath, S. Pearton, J. Lee, W.P. Gomes, X. Xiang, K. Leo, D. Lie, K. Wang, and E. Zanoni. 2001. Handbook of Advanced Electronic and Photonic Materials and Devices. *Handbook of Advanced Electronic and Photonic Materials and Devices: Conducting polymers*.

Doudevski, I., W.A. Hayes, and D.K. Schwartz. 1998. Submonolayer island nucleation and growth kinetics during self-assembled monolayer formation. *Physical review letters*. 81:4927-4930.

Glang, R., and L.I. Maissel. 1970. Handbook of thin film technology. McGraw-Hill New York.

Gustafsson, G., Y. Cao, G. Treacy, F. Klavetter, N. Colaneri, and A. Heeger. 1992. Flexible light-emitting diodes made from soluble conducting polymers. *nature*. 357:477-479.

Haldi, A. 2008. Patternable electrophosphorescent organic light-emitting diodes with solution-processed organic layers. Georgia Institute of Technology.

Huang, Q., G.A. Evmenenko, P. Dutta, P. Lee, N.R. Armstrong, and T.J. Marks. 2005. Covalently bound hole-injecting nanostructures. Systematics of molecular architecture, thickness, saturation, and electron-blocking characteristics on organic light-emitting diode luminance, turn-on voltage, and quantum efficiency. *Journal of the American Chemical Society*. 127:10227-10242.

Khan, M., W. Xu, Y. Bai, X. Jiang, Z. Zhang, and W. Zhu. 2008. Electron mobility of 4, 7-diphyenyl-1, 10-phenanthroline estimated by using space-charge-limited currents. *Journal of Applied Physics*. 103:014509.

Kijima, Y., N. Asai, and S. Tamura. 1999. A blue organic light emitting diode. *Jpn. J. Appl. Phys*. 38:5274-5277.

Kim, J.S., P.K.H. Ho, N.C. Greenham, and R.H. Friend. 2000. Electroluminescence emission pattern of organic light-emitting diodes: Implications for device efficiency calculations. *Journal of Applied Physics*. 88:1073.

Kim, Y., and C.S. Ha. 2008. Advances in organic light-emitting device. *Trans Tech Publications, Switzerland*.

Kittel, C., and P. McEuen. 1996. Introduction to solid state physics. Wiley New York.

Kulkarni, A.P., C.J. Tonzola, A. Babel, and S.A. Jenekhe. 2004. Electron transport materials for organic light-emitting diodes. *Chemistry of materials*. 16:4556-4573.

Langevin, P. 1903. The ionisation of gases. Vol. 28. 289-384.

Lee, C.T., Q.X. Yu, B.T. Tang, and H.Y. Lee. 2001. Effects of plasma treatment on the electrical and optical properties of indium tin oxide films fabricated by rf reactive sputtering. *Thin solid films*. 386:105-110.

Lee, J., B.J. Jung, J.I. Lee, H.Y. Chu, L.M. Do, and H.K. Shim. 2002. Modification of an ITO anode with a hole-transporting SAM for improved OLED device characteristics. *Journal of Materials Chemistry*. 12:3494-3498.

Li, Z.R., and H. Meng. 2007. Organic light-emitting materials and devices. CRC/Taylor & Francis.

Maldonado, S., T.J. Smith, R.D. Williams, S. Morin, E. Barton, and K.J. Stevenson. 2006. Surface modification of indium tin oxide via electrochemical reduction of aryldiazonium cations. *Langmuir*. 22:2884-2891.

Malinsky, J.E., G.E. Jabbour, S.E. Shaheen, J.D. Anderson, A.G. Richter, T.J. Marks, N.R. Armstrong, B. Kippelen, P. Dutta, and N. Peyghambarian. 1999. Self Assembly Processes for Organic LED Electrode Passivation and Charge Injection Balance. *Advanced Materials*. 11:227-231.

Marrón, Y., and J. Luis. 2010. Development of a new chemical sensor based on plasma polymerized polypyrrole films.

Mironov, V. 2004. Fundamentals of the scanning probe microscopy. *Journal of Nanoscience and Nanotechnology*. 4.

Nüesch, F., E. Forsythe, Q. Le, Y. Gao, and L. Rothberg. 2000. Importance of indium tin oxide surface acido basicity for charge injection into organic materials based light emitting diodes. *Journal of Applied Physics*. 87:7973.

Nuesch, F., F. Rotzinger, L. Si-Ahmed, and L. Zuppiroli. 1998. Chemical potential shifts at organic device electrodes induced by grafted monolayers. *Chemical physics letters*. 288:861-867.

Nuzzo, R.G., and D.L. Allara. 1983. Adsorption of bifunctional organic disulfides on gold surfaces. *Journal of the American Chemical Society*. 105:4481-4483.

Pei, Q., and S. Oh. 2003. Cavity-emission electroluminescent device and method for forming the device. Google Patents.

Pope, M., H. Kallmann, and P. Magnante. 1963. Electroluminescence in organic crystals. *Journal of Chemical Physics*. 38:2042-2043.

Pope, M., and C.E. Swenberg. 1999. Electronic processes in organic crystals and polymers. Oxford University Press.

Rakurthi, A. 2010. Improvement of Efficiencies and Lifetimes of White Light-Emitting Organic Diodes Using a Novel Co-evaporated 'Hole-Confining'Structure. *Structure*. 2010:08-06.

Rhoderick, E.H., and R. Williams. 1978. Metal-semiconductor contacts. Clarendon Press Oxford.

Rockett, A. 2007. Materials science of semiconductors. Springer Verlag.

Rosenwaks, Y., R. Shikler, T. Glatzel, and S. Sadewasser. 2004. Kelvin probe force microscopy of semiconductor surface defects. *Physical Review B*. 70:085320.

Selzer, Y., A. Salomon, and D. Cahen. 2002. The importance of chemical bonding to the contact for tunneling through alkyl chains. *The Journal of Physical Chemistry B*. 106:10432-10439.

Shen, Y., A.R. Hosseini, M.H. Wong, and G.G. Malliaras. 2004. How to make ohmic contacts to organic semiconductors. *ChemPhysChem*. 5:16-25.

Shen, Y., D. Jacobs, G. Malliaras, G. Koley, M. Spencer, and A. Ioannidis. 2001. Modification of indium tin oxide for improved hole injection in organic light emitting diodes. *Advanced Materials*. 13:1234-1238.

Shinar, J. 2004. Organic light-emitting devices: a survey. Springer Verlag.

Tang, C., and S. VanSlyke. 1987. Organic electroluminescent diodes. *Applied Physics Letters*. 51:913-915.

Vincett, P., W. Barlow, R. Hann, and G. Roberts. 1982. Electrical conduction and low voltage blue electroluminescence in vacuum-deposited organic films. *Thin solid films*. 94:171-183.

Vuillaume, D., S. Lenfant, D. Guerin, C. Delerue, C. Petit, and G. Salace. 2006. Electronic properties of organic monolayers and molecular devices. *Pramana*. 67:17-32.

Wang, W., T. Lee, and M.A. Reed. 2003. Mechanism of electron conduction in self-assembled alkanethiol monolayer devices. *Physical Review B*. 68:035416.

Wu, C., P.I. Djurovich, and M.E. Thompson. 2009. Study of Energy Transfer and Triplet Exciton Diffusion in Hole Transporting Host Materials. *Advanced Functional Materials*. 19:3157-3164.

Xueyin, J., Z. Zhilin, Z. Xiaowen, Z. Liang, and L. Jun. 2009. Estimation of electron mobility of n-doped 4, 7-diphenyl-1, 10-phenanthroline using space-charge-limited currents. *Journal of Semiconductors*. 30:114009.

Yang, X., Y. Mo, W. Yang, G. Yu, and Y. Cao. 2001. Efficient polymer light emitting diodes with metal fluoride/Al cathodes. *Applied Physics Letters*. 79:563.

Zurowski, A. 2009. Cesium and rubidium salts of Keggin-type heteropolyacids as stable meso-microporous matrix for anode catalyst for H2/O2 Proton Exchange Membrane Fuel Cell, Direct Methanol Fuel Cell and Direct Ethanol Fuel Cell.